Chapter 5

Characterisation of $Ba_2LnSn_xB'_{1-x}O_{6-\delta}$ (Ln = Pr or Tb and B' = Nb^{5+} or Sb^{5+})

5.1 Introduction

The presence of cations capable of exhibiting multiple valencies and oxygen vacancies in perovskites is of significant interest to researchers because of the potential for high electronic and ionic conductivity associated with these respective features[1-4]. As highlighted in Chapter 1 in perovskites with cations capable of adopting mixed valencies there is competition between the oxidation of such a cation to a higher oxidation state and the formation of oxygen vacancies in the perovskite structure. This competition will have a strong effect on the ionic conducting properties of these materials, as those oxides with higher levels of anion vacancies are likely to have higher proton and oxygen anion conductivity. On the other hand the electronic conductivity of such materials is also likely to be affected by the precise oxidation states of the cations present since this will affect the occupancies of the valence and conduction bands in these compounds.

In this chapter the structures of perovskite compounds belonging to the series $Ba_2LnSn_xB'_{1-x}O_{6-\delta}$ (Ln = Pr or Tb and B' = Nb^{5+} or Sb^{5+}) are explored with an emphasis on determining the valencies of the cations, and particularly the lanthanides, contained therein. This series of compounds was chosen because of their similarity to $Ba_2YSnO_{5.5}$, which is known to have good ionic, and particularly proton, conductivity[5]. Pr and Tb, however, are different to Y^{3+} in that they can adopt either a trivalent or tetravalent oxidation state. This presents the possibility that rather than having a large number of oxygen vacancies as $Ba_2YSnO_{5.5}$ does, Pr^{4+} and/or Tb^{4+} may be present in the compounds $Ba_2PrSnO_{6-\delta}$ and $Ba_2TbSnO_{6-\delta}$. This presents the potential for an insight into the relative stability of oxygen vacancies in the perovskite structure compared to the oxidation of a cation capable of adopting a higher valency. The doping of the Sn^{4+} site with either Sb^{5+} or Nb^{5+} allows for a fine-tuning of the valence state of the lanthanide cations and/or the amount of oxygen vacancies present

in the structure. Sb^{5+} and Nb^{5+} cations were selected because of their similar ionic radius to Sn^{4+} (cf. 0.60 and 0.64 Å for Sb^{5+} and Nb^{5+} and 0.69 Å for Sn^{4+}[6]) and the high chemical stability of the $Ba_2LnB'O_6$ (B' = Nb^{5+} or Sb^{5+}) series[7, 8].

In Chapter 3 of this thesis the structures of compounds in the series $Ba_2LnB'O_6$ were studied thoroughly using synchrotron X-ray and neutron diffraction. Ba_2PrSbO_6 and Ba_2PrNbO_6 were found to adopt $R\bar{3}$, rhombohedral, and *I*2/*m*, monoclinic, structures while Ba_2TbSbO_6 and Ba_2TbNbO_6 were established as belonging to the $Fm\bar{3}m$, cubic, and *I*4/*m*, tetragonal, structures respectively. Therefore as well as providing an excellent opportunity to study the relative stability of oxygen vacancies in these structures, the series $Ba_2LnSn_xB'_{1-x}O_{6-\delta}$ also allows the effects of oxygen vacancies and/or a change in the valence state of the lanthanide on the subtly different structures adopted by the $Ba_2LnB'O_6$ family of compounds to be studied. Where oxidation of the lanthanide cations occurs cation ordering may be lost due to the smaller charge and size difference between the Ln^{4+} cations and Sn^{4+}, Nb^{5+} and Sb^{5+}[6].

To explore the structural and chemical features of the $Ba_2LnSn_xB'_{1-x}O_{6-\delta}$ family of compounds four series have been synthesised; namely $Ba_2PrSn_xSb_{1-x}O_{6-\delta}$, $Ba_2TbSn_xSb_{1-x}O_{6-\delta}$, $Ba_2PrSn_xNb_{1-x}O_{6-\delta}$ and $Ba_2TbSn_xNb_{1-x}O_{6-\delta}$. These series were then structurally characterised using a combination of synchrotron X-ray diffraction and, in selected cases, neutron diffraction both at and, where appropriate, above room temperature. Additionally to more clearly elucidate the oxidation states of the cations present in these compounds they have also been examined using X-ray Absorption Near-Edge Structure (XANES), Ultra-Violet, Visible and Near-Infrared (UV-Vis-NIR) spectroscopies and Thermogravimetric Analysis (TGA).

5.2 Synthesis

5.2.1 Synthesis of $Ba_2LnSn_xSb_{1-x}O_{6-\delta}$

Samples of $Ba_2LnSn_xSb_{1-x}O_{6-\delta}$ (Ln = Pr or Tb and x = 0, 0.1, 0.2,…, 1) were prepared from stoichiometric mixtures of $BaCO_3$, SnO_2, Sb_2O_3 and either Pr_6O_{11} or Tb_4O_7. The samples were finely ground as an acetone slurry and after being allowed

to dry were heated at 800 °C for 24 hrs. After being reground the samples were sequentially heated at 1000, 1100, 1150, 1200 and 1300 °C for periods of 24 hrs with samples being reground between each heating period. Where required samples were then heated at 1350 °C for 48 hrs, 1400 °C for 24 hrs and 1450 °C for 24 hrs.

5.2.2 Synthesis of $Ba_2LnSn_xNb_{1-x}O_{6-\delta}$

Samples of $Ba_2LnSn_xNb_{1-x}O_{6-\delta}$ (Ln = Pr or Tb and x = 0, 0.1, 0.2,…, 1) were prepared from stoichiometric mixtures of $BaCO_3$, SnO_2, Nb_2O_5 and either Pr_6O_{11} or Tb_4O_7. The samples were finely ground as an acetone slurry and after being allowed to dry were heated at 1200 °C for 24 hrs. The samples were then heated again at 1300 °C for 24 hrs, reground, pelleted and then heated at 1350 °C for a total of 48 hrs. Where necessary the samples were then reheated, in pelleted form, at 1400 °C and 1450 °C for periods of 24 hrs. Samples were reground between all heating periods.

5.2.3 Synthesis of Oxidation State Standards

Samples of $Ln_2Sn_2O_7$ and $BaLnO_3$ (Ln = Pr or Tb) were synthesised to use as oxidation state standards for Pr and Tb in the trivalent and tetravalent states respectively. The synthesis of these four compounds was done by methods found in the literature as detailed in the following sections.

5.2.3.1 $Ln_2Sn_2O_7$

Approximately 3 g samples of $Ln_2Sn_2O_7$ (Ln = Pr^{3+} or Tb^{3+}) were synthesised using ceramic methods according to a modification of the heating schedule developed by Kennedy *et al*[9]. This involved preparing finely ground stoichiometric mixtures of SnO_2 and either Pr_6O_{11} or Tb_4O_7 and heating these samples at 1000 °C for 48 hrs followed by the sample being reground and reheated at 1400 °C for 48 hrs.

5.2.3.2 $BaLnO_3$

Samples of $BaLnO_3$ (Ln = Pr^{4+} or Tb^{4+}) were synthesised using ceramic methods according to a modification of the heating schedule developed by Yoshimura *et al*.[10]

and Hinatsu[11]. This involved heating a finely ground stoichiometric mixture of $BaCO_3$ and either Pr_6O_{11} or Tb_4O_7 at 1150 °C for two periods of 24 hrs and then at 1300 °C for 24 hrs with the sample being reground between each heating period. The samples were then heated at 1000 °C for 48 hrs under flowing oxygen and slowly cooled to room temperature in order to form compounds that were stoichiometric with respect to oxygen content.

5.3 Experimental Method

Synchrotron X-ray diffraction patterns were collected using the Debye-Scherrer diffractometer at the ANBF, beamline 20B, at the Photon Factory as described in Section 2.2.2.1. Diffraction patterns of all samples were collected at room temperature using 0.80088(1), 0.80123(1), 0.80286(1) or 0.82606(1) Å X-rays. Following this diffraction patterns of selected samples ($Ba_2PrSnO_{6-\delta}$, $Ba_2PrSn_{0.4}Sb_{0.6}O_{6-\delta}$, $Ba_2PrSn_{0.3}Sb_{0.7}O_{6-\delta}$, $Ba_2PrSn_{0.2}Nb_{0.8}O_{6-\delta}$, Ba_2TbNbO_6 and $BaPrO_3$) were collected above ambient temperature up to a maximum temperature of 800 °C using the custom built furnace employing X-rays with a wavelength of 0.79823(1), 0.80088(1), 0.80155(1), 0.80286(1) or 0.9999(1) Å.

Neutron powder diffraction patterns were collected of selected samples at room temperature using either the HRPD, at the HIFAR facility or BT-1 at the NIST Centre for Neutron Research. The diffraction patterns of $Ba_2PrSn_xSb_{1-x}O_{6-\delta}$ (x = 0, 0.3, 0.4, 0.7, 1.0), $Ba_2TbSn_xSb_{1-x}O_{6-\delta}$ (x = 0, 0.8 and 1.0) and Ba_2TbNbO_6 were collected at HIFAR using a wavelength of either 1.4918(1) or 1.4924(1) Å as described in Section 2.2.3.1. The diffraction patterns of $Ba_2PrSn_xNb_{1-x}O_{6-\delta}$ (x = 0, 0.6 and 0.7) and $Ba_2TbSn_xNb_{1-x}O_{6-\delta}$ (x = 0.3, 0.6 and 0.7) were collected using BT-1 utilising a wavelength of 1.5403(1) Å as described in Section 2.2.3.3.

XANES spectra were collected of the L-edge of various cations in the four $Ba_2LnSn_xB'_{1-x}O_{6-\delta}$ series using either beamline 16A1 at the NSRRC or beamline 20B at the ANBF, Photon Factory (see Section 2.4). Beamline 16A1 was used to collect spectra of all three L-edges of the Sn and Sb cations in selected samples in the series $Ba_2LnSn_xSb_{1-x}O_{6-\delta}$ (Ln = Pr or Tb) and the L_{II}- and L_{III}-edges of Pr cations in

$Ba_2PrSn_xSb_{1-x}O_{6-\delta}$. Due to the Sn and Sb edges occurring in similar energy regions the L-edges of both these cations were typically collected in a single scan over the energy range of 3.779-4.998 keV while the spectra of the Pr L_{II}- and L_{III}-edges were collected using an energy scan over the region 5.764-6.740 keV.

Beamline 20B was used to collect spectra at the L_{III}-edge of Tb cations in the series $Ba_2TbSn_xB'_{1-x}O_{6-\delta}$ (B' = Sb^{5+} or Nb^{5+}) and Pr cations in the series $Ba_2PrSn_xNb_{1-x}O_{6-\delta}$. Data were collected over the range of 7.295-7.809 keV and 5.745-6.110 keV for the Tb and Pr L_{III}-edges respectively.

5.4 Results and Discussion

The discussion of the structures and the oxidation state of the cations in the series $Ba_2LnSn_xB'_{1-x}O_{6-\delta}$ will be presented in two sections. The first of these will consider the praseodymium and terbium antimonate compounds while the second will examine the niobate series. Both of these sections will begin with the discussion of the structures adopted by these compounds, as determined by synchrotron X-ray and neutron diffraction, with the examination of the oxidation states of the various cations in these compounds, particularly the lanthanides, being subsequently discussed.

5.4.1 Characterisation of $Ba_2LnSn_xSb_{1-x}O_{6-\delta}$

The discussion of the characterisation of the $Ba_2LnSn_xSb_{1-x}O_{6-\delta}$ series will consist of three sections. The first two of these will detail the structures adopted by the Pr and Tb series. The final section will examine the oxidation state of the cations present in these two series in more depth, using a combination of XANES, UV-Vis-NIR spectroscopies and TGA. These techniques provide a probe of the relative stability of oxygen vacancies compared to cation oxidation in these series. The oxidation states of Sn and Sb in $Ba_2LnSn_xSb_{1-x}O_{6-\delta}$ are assumed to be tetravalent and pentavalent respectively in Sections 5.4.1.1 and 5.4.1.2, which is subsequently confirmed by XANES spectra in section 5.4.1.4.

5.4.1.1 Structures of $Ba_2PrSn_xSb_{1-x}O_{6-\delta}$

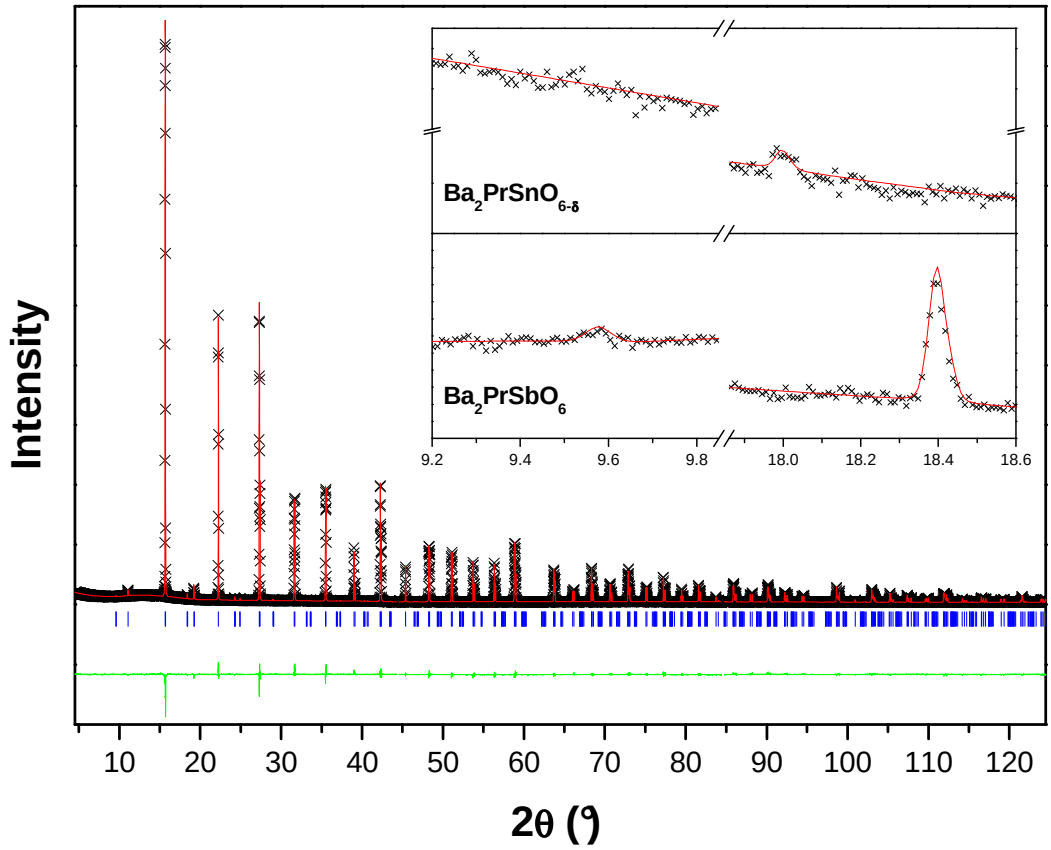

Figure 5.1: Synchrotron X-ray diffraction pattern of Ba_2PrSbO_6. The crosses, upper and lower continuous lines represent the observed and calculated intensities and the difference between these respectively. The vertical markers show the positions of the allowed Bragg reflections. The insert illustrates the low angle *R*-point super-lattice reflections for $Ba_2PrSnO_{6-\delta}$ and Ba_2PrSbO_6. The peak at ~ 18° is present in diffraction patterns of both samples as it is caused by octahedral tilting and/or cation ordering while the lowest angle reflection is not present in the case of $Ba_2PrSnO_{6-\delta}$ as it is caused by cation ordering alone, which is absent in this compound.

As established in Chapter 3 Ba_2PrSbO_6 adopts the rhombohedral $R\bar{3}$ structure (tilt system $a^-a^-a^-$[12, 13]) with refinements of synchrotron X-ray diffraction patterns indicating that the cations are fully ordered in this compound (see Figure 5.1). The sample of $Ba_2PrSnO_{6-\delta}$ used throughout this work was also found to be rhombohedral (see Figure 5.2). X-ray diffraction patterns of this did not, however, exhibit the lowest angle *R*-point (100) and (111) Bragg reflections indicative of cation ordering that were observed at ~ 9.5° (2θ angle) in X-ray diffraction patterns of the Ba_2PrSbO_6

sample (see Figure 5.1). This reveals that the Pr and Sn^{4+} cations in $Ba_2PrSnO_{6-\delta}$ do not order and that it adopts the $R\bar{3}c$ ($a^-a^-a^-$) space group.

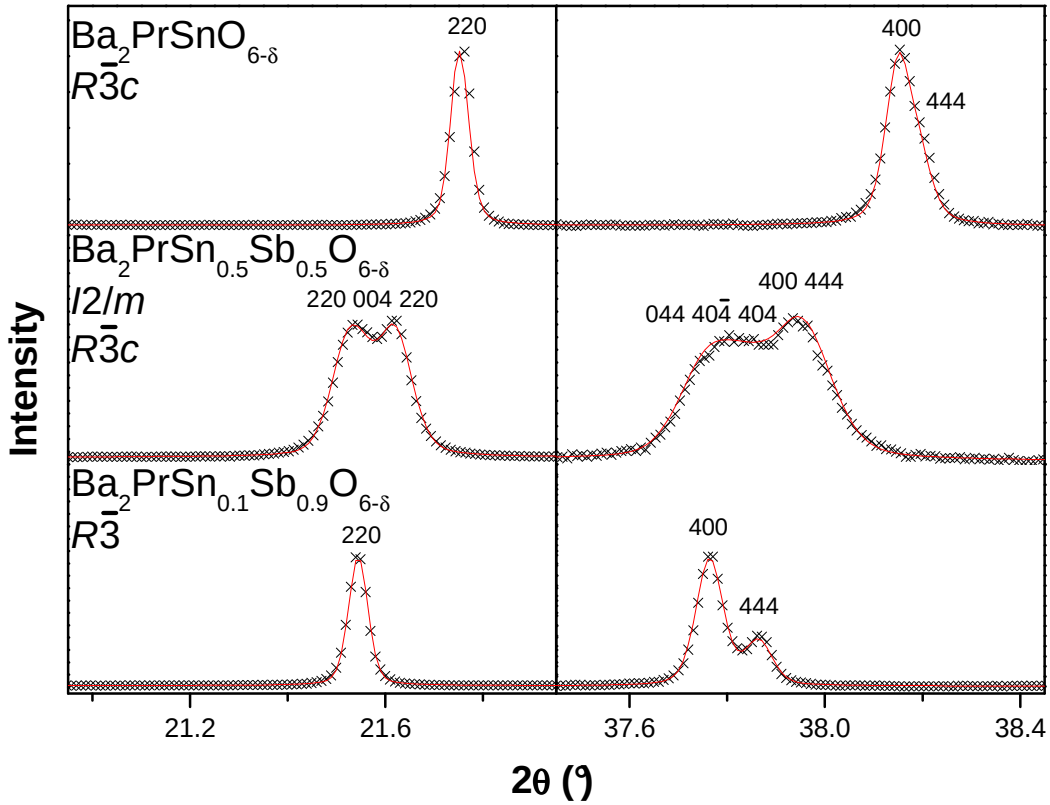

Figure 5.2: Selected portions of synchrotron X-ray diffraction patterns of compounds in the series $Ba_2PrSn_xSb_{1-x}O_{6-\delta}$ indicating the different structures adopted. The black crosses and the red line are the observed and calculated intensities. The patterns have been rescaled to better illustrate the changes, with the parent (444) reflection near 2θ = 38.0° being ~ $1/5^{th}$ as intense as the cubic (400) reflection near 2θ = 21.6°.

The unit cell of $Ba_2PrSnO_{6-\delta}$ is considerably smaller than that of Ba_2PrSbO_6 (cf. a unit cell volume of 153.68(6) to 157.06(1) $Å^3$ for $Ba_2PrSnO_{6-\delta}$ and Ba_2PrSbO_6 respectively). This is an interesting observation as Sn^{4+} has a larger ionic radius than Sb^{5+} (cf. 0.69 and 0.60 Å for Sn^{4+} and Sb^{5+} respectively[6]) and therefore, assuming all other cations remain the same size in both structures, the unit cell of $Ba_2PrSnO_{6-\delta}$ would be expected to be larger than that of Ba_2PrSbO_6. One possible reason for the contraction in unit cell size is that some, or all, of the Pr cations in $Ba_2PrSnO_{6-\delta}$ may be tetravalent. The difference between the ionic radius of Pr^{4+} and Pr^{3+} is larger than

that of Sn^{4+} and Sb^{5+} (the ionic radius of Pr^{4+} and Pr^{3+} are 0.85 and 0.99 Å respectively[6]) and consequently the formation of Pr^{4+} in $BaPrSnO_{6-\delta}$ would explain the smaller unit cell size. The loss of cation ordering is consistent with this hypothesis as the smaller size (cf. a size difference of 0.16 to 0.39 Å for the Pr^{4+}/Sn^{4+} and Pr^{3+}/Sb^{5+} pairings[6]) and charge difference between Pr^{4+} and Sn^{4+} would reduce the tendency of the B-site cations to order. The partial occupancy of the oxygen anion site in $Ba_2PrSnO_{6-\delta}$ refines as being 99.6(6) % occupied indicating that there is not a significant quantity of oxygen vacancies in $Ba_2PrSnO_{6-\delta}$. This indicates that essentially all (95(8) %) of the Pr in $Ba_2PrSnO_{6-\delta}$ is tetravalent. Similarly refinement of a suitable model against a neutron diffraction pattern of Ba_2PrSbO_6 yields an oxygen site occupancy of 101.5(6) % indicating that, assuming all Sb in this compound is pentavalent, the Pr in this antimonate is all trivalent.

Refinements yield a Pr-O bond length of 2.130(2) Å for $Ba_2PrSnO_{6-\delta}$ compared to 2.312(2) Å in Ba_2PrSbO_6, a difference of approximately 0.18 Å (see Tables 5.1 and 5.2 for crystallographic details, and selected bond distances, respectively). This is comparable to the 0.14 Å difference between the ionic radius of Pr^{3+} and Pr^{4+} (cf. an ionic radius of 0.99 Å for Pr^{3+} to 0.85 Å for Pr^{4+}[6]) and is consistent with a valency change from Pr^{3+} to Pr^{4+} when Sn^{4+} is substituted for Sb^{5+}. As noted in Chapter 3 for all $Ba_2LnB'O_6$ compounds (Ln = lanthanide and B'^{5+} = Nb^{5+}, Ta^{5+} or Sb^{5+}) the Pr-O bond lengths are shorter in both these structures than would be expected from the sum of their ionic radii (which is 2.39 and 2.25 Å for Pr^{3+}-O and Pr^{4+}-O respectively[6]). This leads to Pr having a bond valency of 3.72 and 6.08 (based on the bond valence parameter for Pr^{3+}-O) for the Sb^{5+} and Sn^{4+} compounds respectively. This is unusually high, especially for $Ba_2PrSnO_{6-\delta}$, which adopts the B-cation disordered $R\bar{3}c$ structure. In contrast the Sn^{4+} cations in $Ba_2PrSnO_{6-\delta}$, which share the same site as the Pr cations, are significantly underbonded with a bond valence sum of 3.27. The apparent overbonding of the Pr^{4+} cation and the underbonding of the Sn^{4+} cation is, at least in part, a result of their sharing the same crystallographic site and may suggest that the local environment around these cations is distorted from the average environment determined from the refinement. This is a reminder that local distortions can occur that can not be readily revealed by Rietveld refinement and these may be particularly

important when two cations with significantly different size or charge occupy the same crystallographic site.

Table 5.1: Crystallographic details for members of the series $Ba_2PrSn_xSb_{1-x}O_{6-\delta}$ determined using neutron diffraction. The phases in $Ba_2PrSn_{0.4}Sb_{0.6}O_{6-\delta}$ have larger errors due to the refinement requiring more parameters because of the presence of two phases. In the *I*2/*m* structure of $Ba_2PrSn_{0.4}Sb_{0.6}O_{6-\delta}$ the partial occupancy of the 2*a* site is fixed as 0.82 as determined using synchrotron X-ray diffraction with the remainder consisting of, in the appropriate stoichiometric ratio, Sn^{4+} and Sb^{5+}. The B' site is occupied in the opposite manner to maintain nominal stoichiometry.

Compound	Ba_2PrSbO_6	$Ba_2PrSn_{0.4}Sb_{0.6}O_{6-\delta}$		$Ba_2PrSnO_{6-\delta}$
Space Group	$R\bar{3}$	*I*2/*m*	$R\bar{3}c$	$R\bar{3}c$
a (Å)	6.0529(1)	6.0557(8)	6.0158 (22)	6.0099(3)
b (Å)	= *a*	6.0393(6)	= *a*	= *a*
c (Å)	= *a*	8.5393(11)	= *a*	= *a*
α (°)	60.147(2)	90	60.506(45)	60.056(4)
β (°)	= α	89.991(18)	= α	= α
γ(°)	= α	90	= α	= α
Ba	2*c* (x,x,x)	4*i* (x,0,z)	2*a* (¼,¼,¼)	2*a* (¼,¼,¼)
x	0.2505(4)	0.5016(22)	¼	¼
z	= x	0.2492(32)	¼	¼
B (Å^2)	0.66(3)	0.63(5)	2.76(56)	0.91(3)
Pr	1*a* (0,0,0)	2*a* (0,0,0)	2*b* (0,0,0)	2*b* (0,0,0)
B (Å^2)	0.66(7)	0.38(10)	0.68(42)	0.47(3)
B'	1*b* (½,½,½)	2*d* (0,0,½)	2*b* (0,0,0)	2*b* (0,0,0)
B (Å^2)	0.12(5)	0.17(9)	= Pr *B*	= Pr *B*
O1	6*f* (x,y,z)	4*i* (x,0,z)	6*e* (x,½-x,¾)	6*e* (x,½-x,¾)
x	0.7309(4)	-0.0350(20)	0.7839(26)	0.7270(2)
y	0.2390(3)	0	0.7161(26)	0.7730(2)
z	0.2988(2)	0.2591(20)	¼	¼
B (Å^2)	1.15(2)	0.57(12)	2.28(28)	1.60(2)
O2		8*j* (x,y,z)		
x		0.2770(15)		
y		0.2521(20)		
z		0.0110(15)		
B (Å^2)		1.83(11)		
R_p %	6.2	4.4		6.7
R_{wp} %	7.3	5.2		8.1
χ^2	1.5	1.6		1.8

Table 5.2: Bond distances and bond valence sums (BVS) for selected members of the series $Ba_2PrSn_xSb_{1-x}O_{6-\delta}$ as determined by neutron diffraction. The Pr^{3+}-O bond valence parameter was used for the calculation of the Pr-O BVS as the appropriate value for Pr^{4+} is not known. In the mixed Sn^{4+} and Sb^{5+} samples the BVS of Sn^{4+} is listed above that of Sb^{5+}.

x	Space Group	Ba-O			Pr-O		B'-O	
		Bond Length (Å)		BVS	Bond Length (Å)	BVS	Bond Length (Å)	BVS
0	$R\bar{3}$	3 × 2.8565(9) 3 × 3.029(5)	3 × 3.043(5) 3 × 3.2190(8)	1.69	6 × 2.312(2)	3.72	6 × 1.989(2)	5.28
0.4	$I2/m$	1 × 2.808(12) 2 × 2.882(10) 2 × 3.008(12) 2 × 3.0272(9)	2 × 3.047(11) 2 × 3.166(10) 1 × 3.250(12)	1.73	2 × 2.222(17) 4 × 2.268(13)	4.37	2 × 2.068(17) 4 × 2.018(20)	4.23 4.68
	$R\bar{3}c$	3 × 2.825(1) 6 × 3.015(15) 3 × 3.237(1)		1.78	6 × 2.145(22)	5.84	= Pr-O	3.13 3.47
1	$R\bar{3}c$	3 × 2.8691(1) 6 × 3.008(1) 3 × 3.1459(1)		1.79	6 × 2.130(2)	6.08	= Pr-O	3.27

It is worth mentioning at this point that a synchrotron X-ray diffraction pattern of a second sample of $Ba_2PrSnO_{6-\delta}$ (~ 2 g in size cf. to the ~ 15 g sample used for all other analysis) showed that this sample was metrically cubic. Similarly to the case of Ba_2LaTaO_6 (see Chapter 3) this suggests that the thermal history of samples is important in determining the precise nature of the structure adopted. In the case of $Ba_2PrSnO_{6-\delta}$ the larger size of the sample used throughout this work may have either slightly restricted the oxidation of Pr^{3+} to Pr^{4+} during the reaction by limiting the air flow through the sample or, alternatively, reduced the surface area of the sample in contact with the crucible and thereby decreased the reaction of Pr with the vessel resulting in the larger sample having a higher Pr content. The full oxygen stoichiometry determined from the refinement of the neutron diffraction pattern would appear to suggest that the latter of these is more likely. Either of these effects would, however, increase the average B-site cation radius in the larger sample of $Ba_2PrSnO_{6-\delta}$, thereby resulting in the adoption of the lower symmetry rhombohedral structure at room temperature while the smaller sample is cubic. A diffraction pattern of the rhombohedral sample of $Ba_2PrSnO_{6-\delta}$ obtained at 100 °C reveals that this sample adopts $Pm\bar{3}m$ cubic symmetry and that, particularly given the small

rhombohedral distortion of this sample at ambient temperature (α = 60.0551(9)°), the difference between the two samples is most likely very small.

Having established that the two end-member oxides of the series $Ba_2PrSn_xSb_{1-x}O_{6-\delta}$, Ba_2PrSbO_6 and $Ba_2PrSnO_{6-\delta}$, adopt $R\bar{3}$ and $R\bar{3}c$ symmetry and most likely contain Pr in the trivalent and tetravalent state respectively, the structure of the intermediate compounds was then investigated. The x = 0.1 and 0.2 samples had splitting and super-lattice reflections consistent with $R\bar{3}$ symmetry and were well fitted by models in this space group. The splitting of the x = 0.3-0.9 samples were, however, significantly different from that of Ba_2PrSbO_6 (see Figure 5.2). The diffraction pattern of the x = 0.3 sample was, initially, successfully fitted using a model consisting of a single phase $I2/m$ ($a^-a^-c^0$) structure. Variable temperature diffraction patterns, however, appeared to indicate that this structure was adopted up to 760 °C, the maximum temperature investigated. This was unexpected and led to careful re-examination of the variable temperature diffraction patterns. This revealed that the data were slightly better fitted by models consisting of two cubic phases (cf. an R_p and R_{wp} of 3.7 and 5.1 % for the two phase cubic model compared to 4.7 and 6.5 % for the monoclinic model fitted to the 760 °C diffraction pattern). That $Ba_2PrSn_{0.3}Sb_{0.7}O_{6-\delta}$ consists of two phases over the range of 100 to 760 °C suggests that the sample features some sort of cation segregation, similar to that found in the $Ba_2LnNb_{1-x}Sb_xO_6$ series in Chapter 4. Therefore the room temperature pattern should also be two phases. The fit of the two phase model to the diffraction pattern collected at 760 °C suggests that the major phase makes up approximately 90 % of the sample (see Figure 5.3) explaining why the initial investigation of the sample at ambient temperature failed to detect the second minor phase. Subsequent fitting of the room temperature diffraction pattern with a two phase mixture of $I2/m$ monoclinic and $R\bar{3}c$ rhombohedral structures, the later selected because it is the symmetry adopted by $Ba_2PrSnO_{6-\delta}$, provided a better fit than the $I2/m$ monoclinic structure alone (cf. an R_p and R_{wp} of 3.2 and 4.5 % for the two phase model to 4.6 and 6.0 % for the single phase monoclinic model).

Similar two phase models consisting of $I2/m$ monoclinic and $R\bar{3}c$ rhombohedral structures provided the best fit to diffraction patterns of samples with x = 0.4-0.9. It

should be noted that attempts to fit the patterns of x = 0.3-0.9 compounds with two cubic phases, as was suitable for fitting patterns of $Ba_2PrSn_{0.3}Sb_{0.7}O_{6-\delta}$ obtained above ambient temperature, were unsuccessful. Such fits did not model sufficient intensity in the *R*-point super-lattice reflections of neutron diffraction patterns obtained of selected two phase samples (x = 0.3, 0.4 and 0.7) and failed to account for significant peak broadening that was consistent with the splitting of the monoclinic phase (see Figure 5.2). Attempts to fit the two phase region with two rhombohedral phases, as would be the case if these two phase samples consisted of the structures belonging to the x = 0 and 1.0 end-members, were also unsuccessful. Variable temperature X-ray diffraction patterns of $Ba_2PrSn_{0.4}Sb_{0.6}O_{6-\delta}$ indicate that similar to $Ba_2PrSn_{0.3}Sb_{0.7}O_{6-\delta}$ it consists of two phases up to the maximum temperature examined, in this case 800 °C, where it is well fitted by two cubic phases.

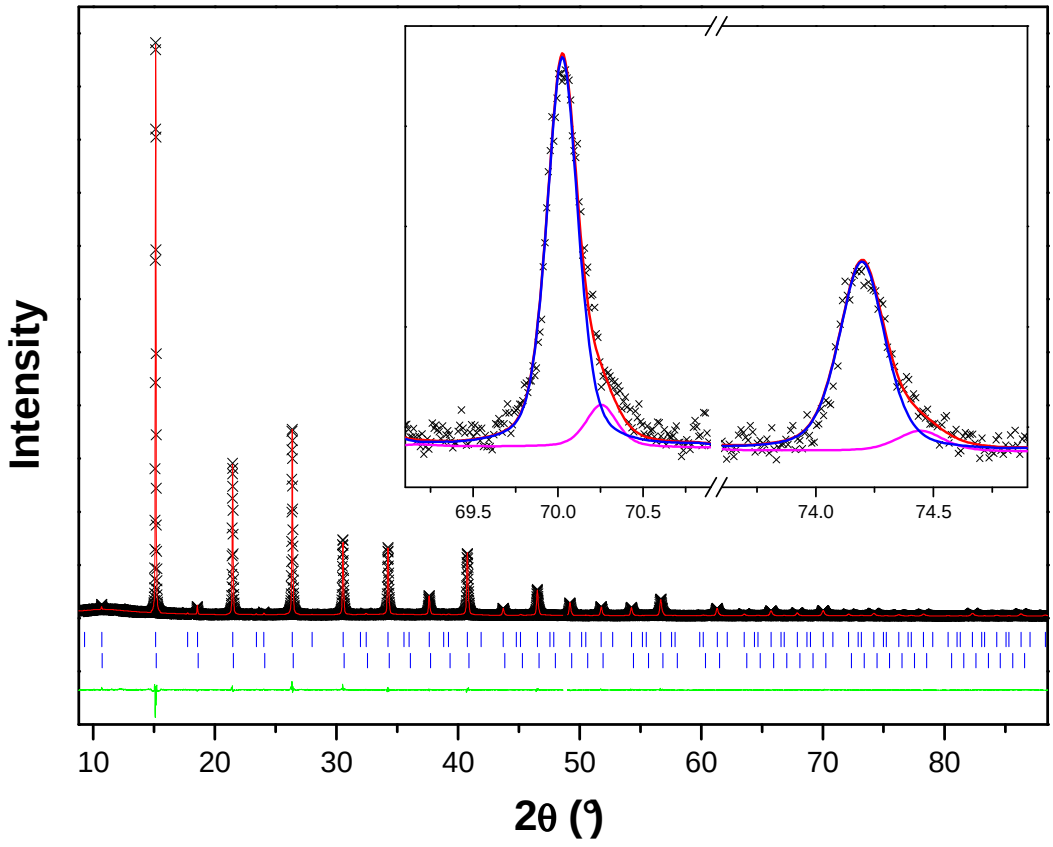

Figure 5.3: Synchrotron X-ray diffraction pattern of $Ba_2PrSn_{0.3}Sb_{0.7}O_{6-\delta}$ at 760 °C. The format is the same as for Figure 5.1. The insert depicts the calculated intensities of the two cubic phases in the sample and the overall calculated intensity.

The large two phase region in this series and its persistence to high temperature, as seen in $Ba_2PrSn_{0.3}Sb_{0.7}O_{6-\delta}$ and $Ba_2PrSn_{0.4}Sb_{0.6}O_{6-\delta}$, suggests that these two structures form as a result of phase segregation into phases with different chemical composition. A combination of Energy Dispersive X-ray (EDX) analysis and backscattered electron images collected using Scanning Electron Microscopy (SEM) was, therefore, used to investigate if any cation segregation was present. There were no significantly contrasting regions in the backscattered images (see Figure 5.4) indicating that the samples are reasonably homogenous and the EDX analysis did not find any significant variation in the cation concentrations in the regions studied across the sample. It should, however, be noted that because Sn^{4+} and Sb^{5+} have similar atomic numbers (50 and 51 respectively) and have X-ray emission spectra that overlap to a significant extent, there is some correlation between the amount of Sn^{4+} and Sb^{5+} estimated by EDX analysis. The variation of Sn^{4+} and Sb^{5+} concentrations between regions, while larger than that found for Ba^{2+} and Pr, is much smaller than that found in the $Ba_2LnNb_xSb_{1-x}O_6$ series. This suggests that while there may be some small amount of Sn^{4+} and Sb^{5+} segregation between the two phases this is not large enough to be detectable due to the overlap of the Sn^{4+} and Sb^{5+} X-ray emission spectra.

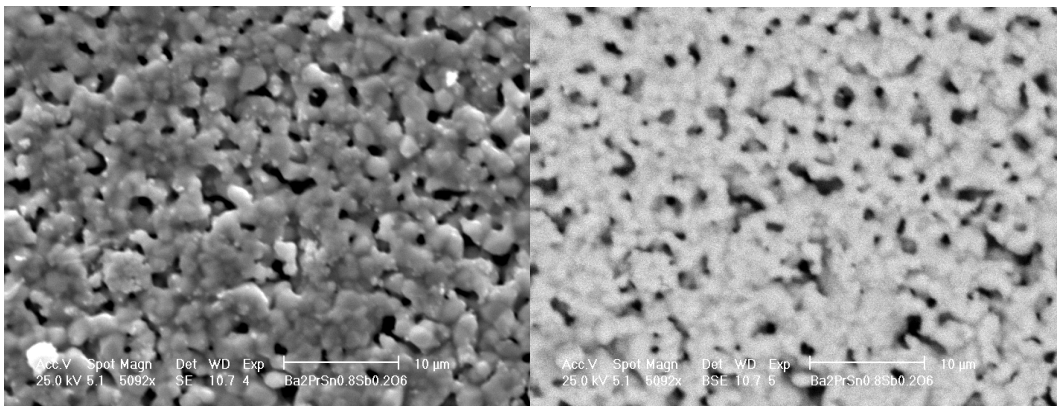

Figure 5.4: Secondary (left) and backscattered (right) electron images of $Ba_2PrSn_{0.8}Sb_{0.2}O_{6-\delta}$. The lack of contrast in the backscattered image suggests the sample is relatively homogeneous.

An explanation of why EDX analysis and SEM did not find any significant cation segregation in the two phase $Ba_2PrSn_xSb_{1-x}O_{6-\delta}$ samples is required to explain the phase segregation in these. It is possible that the failure to detect significant cation segregation is a result of either a small amount occurring or it happening on a length

scale smaller than can be resolved by these techniques. The structural parameters for these compounds may, however, suggest at alternate explanation. Examination of the lattice parameters of the monoclinic and rhombohedral phases shows that the unit cell of the monoclinic phase is significantly larger than that of the rhombohedral phase in each sample (see Table 5.3 and Figure 5.5). Preferential concentration of the Pr^{3+} and Pr^{4+} into the monoclinic and rhombohedral phases respectively, would seem to be a likely cause of the different unit cell sizes of the two structures given the significant size difference between Pr^{3+} and Pr^{4+}. Segregation of different oxidation states of the same element would not be detectable by EDX analysis or backscattered electron images explaining why these techniques suggest the samples to be chemically homogeneous. Refinement of a neutron diffraction pattern of $Ba_2PrSn_{0.4}Sb_{0.6}O_{6-\delta}$ reveals that the bond length of the Pr site in the monoclinic phase is much longer than the mixed Pr/Sn/Sb site in the rhombohedral phase (see Table 5.2). This is consistent with the above hypothesis, which is also supported by the increase in mol % of the rhombohedral phase present in samples with increasing x. Similarly to $Ba_2PrSnO_{6-\delta}$ the lack of B-site cation order in the $R\bar{3}c$ phase of $Ba_2PrSn_{0.4}Sb_{0.6}O_{6-\delta}$ leads to the Pr occupying a site where it is apparently very overbonded while the Sn^{4+} and Sb^{5+} cations are very underbonded suggesting that the local order environment around each of these cations may be different from the average structure.

Refinements using the synchrotron X-ray diffraction patterns reveal that the double perovskite phases, $R\bar{3}$ for x = 0-0.2 and *I*2/*m* monoclinic for x = 0.3-0.6, generally feature increasing B-site cation disorder with increasing x. There is, however, a significant increase in the amount of ordering present between the single phase x = 0.2 sample and the monoclinic phase of the x = 0.3 sample (cf. 77(3) % of Pr on the 1*a* site in x = 0.2 to 92(2) % on the 2*a* site in the x = 0.3 sample). This may reflect the partial segregation of the Pr^{4+} cations into the disordered $R\bar{3}c$ phase in the x = 0.3 sample. This would leave a smaller amount of Pr^{4+} in the monoclinic phase thereby leading to increased ordering compared to the x = 0.2 sample. The degree of B-site cation ordering appears to increase again between the x = 0.6 and 0.7 samples. That the monoclinic phase makes up less than 15 mol % of the two phase mixture in the x = 0.7-0.9 samples, however, suggests that this observation regarding B-site ordering must be treated with caution.

Table 5.3: Phase composition and unit cell parameters for the $Ba_2PrSn_xSb_{1-x}O_{6-\delta}$ series of compounds determined using synchrotron X-ray diffraction. In the case of the *I*2/*m* phases in the x = 0.7-0.9 samples the monoclinic angle was very close to 90° and unstable in the refinement and was therefore set to 90°.

x	Space Group	*a* (Å)	*b* (Å)	*c* (Å)	α (°)	β (°)	Volume (Å^3)	Phase Composition (mol %)
0	$R\bar{3}$	6.04912(1)	= *a*	= *a*	60.1522(2)	= α	157.056(13)	100
0.1	$R\bar{3}$	6.04792(2)	= *a*	= *a*	60.1277(4)	= α	156.878(30)	100
0.2	$R\bar{3}$	6.04328(6)	= *a*	= *a*	60.1081(10)	= α	156.414(70)	100
0.3	*I*2/*m*	6.04268(11)	6.06053(12)	8.54974(19)	90	90.0779(24)	313.105(11)	81.9(4)
	$R\bar{3}c$	6.02493(25)	= *a*	= *a*	60.1319(51)	= α	155.105(344)	18.1(4)
0.4	*I*2/*m*	6.04149(14)	6.05938(15)	8.54959(29)	90	90.0681(43)	312.980(15)	51.0(2)
	$R\bar{3}c$	6.02040(14)	= *a*	= *a*	60.1039(26)	= α	154.601(144)	49.0(3)
0.5	*I*2/*m*	6.04013(11)	6.06012(10)	8.54356(22)	90	90.0571(45)	312.728(11)	34.5(1)
	$R\bar{3}c$	6.02021(12)	= *a*	= *a*	60.0523(22)	= α	154.464(143)	65.5(3)
0.6	*I*2/*m*	6.03978(18)	6.06065(14)	8.54245(36)	90	90.0198(244)	312.696(18)	17.3(1)
	$R\bar{3}c$	6.02324(13)	= *a*	= *a*	60.0423(22)	= α	154.661(144)	82.7(4)
0.7	*I*2/*m*	6.03760(17)	6.05958(13)	8.53771(29)	90	90	312.355(15)	14.5(1)
	$R\bar{3}c$	6.01974(7)	= *a*	= *a*	60.0057(20)	= α	154.282(130)	85.5(3)
0.8	*I*2/*m*	6.03547(21)	6.06002(13)	8.53594(30)	90	90	312.202(17)	7.5(1)
	$R\bar{3}c$	6.01657(7)	= *a*	= *a*	60.0088(19)	= α	154.029(128)	92.5(3)
0.9	*I*2/*m*	6.03066(40)	6.05252(26)	8.52788(63)	90	90	311.273(34)	2.8(1)
	$R\bar{3}c$	6.01320(6)	= *a*	= *a*	60.0104(17)	= α	153.848(110)	97.2(3)
1.0	$R\bar{3}c$	6.00990(6)	= *a*	= *a*	60.0551(9)	= α	153.683(58)	100

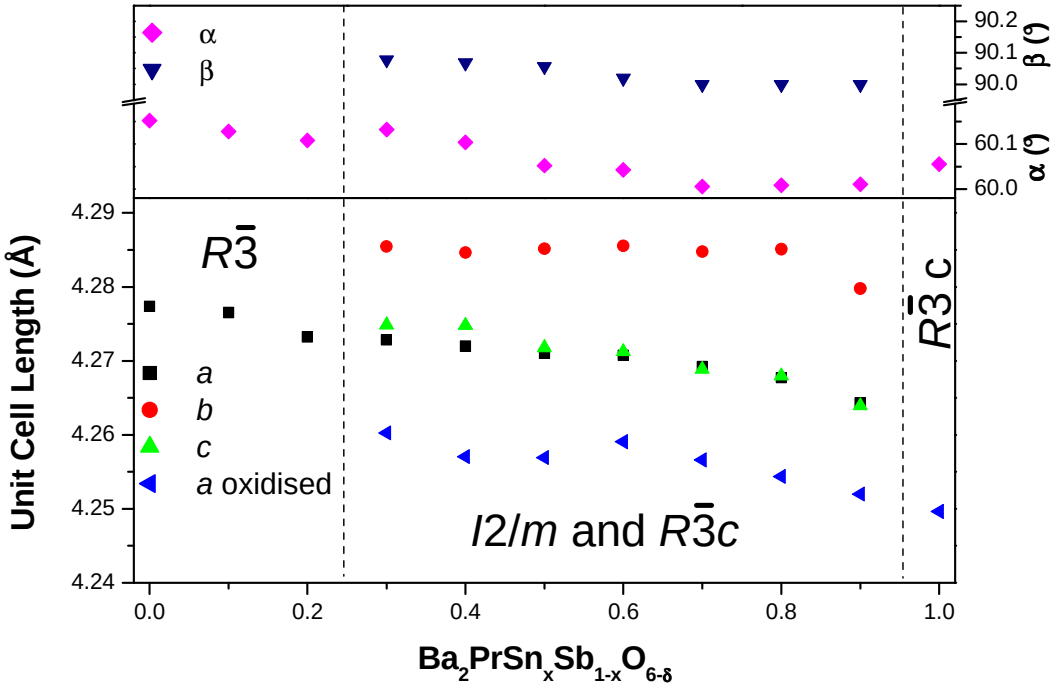

Figure 5.5: Lattice parameters for compounds in the series $Ba_2PrSn_xSb_{1-x}O_{6-\delta}$. "a oxidised" corresponds to the rhombohedral phase hypothesised to contain predominately Pr^{4+}. Unit cell lengths have been reduced to the size of the primitive cubic perovskite for ease of comparison.

5.4.1.2 Structures of $Ba_2TbSn_xSb_{1-x}O_{6-\delta}$

As observed in Chapter 3 synchrotron X-ray diffraction patterns of Ba_2TbSbO_6 reveal that it adopts a fully B-site cation ordered structure belonging to the untilted $Fm\bar{3}m$ space group. $Ba_2TbSnO_{6-\delta}$ is also found to be metrically cubic but lacks the *R*-point super-lattice reflections that, in the untilted cubic structure, indicate the presence of B-site cation ordering (see Figure 5.6 and 5.7). Therefore, similarly to $Ba_2PrSnO_{6-\delta}$, the Tb and Sn^{4+} cations in $Ba_2TbSnO_{6-\delta}$ share the same site in a $Pm\bar{3}m$ cubic perovskite structure.

The peaks in both the synchrotron X-ray and neutron diffraction patterns of $Ba_2TbSnO_{6-\delta}$ are notably asymmetric, especially in the higher resolution X-ray diffraction data, with this asymmetry increasing at higher angles (see Figure 5.7). This asymmetry is not consistent with subtle unresolved splitting of a lower symmetry structure. Rather it is similar to the asymmetry noted in the peak shapes of the related

compound Ba_2InNbO_6 by Ting *et al.*[14], which adopts the $Fm\bar{3}m$ cubic structure with a high degree of B-site cation disorder. These authors concluded that this unusual peak shape was caused by strain induced by twinning and stacking faults arising from the disorder of the B-site cations. Since the B-site cations in $Ba_2TbSnO_{6-\delta}$ are completely disordered it is likely that the peak shape observed in this compound is caused by a similar effect.

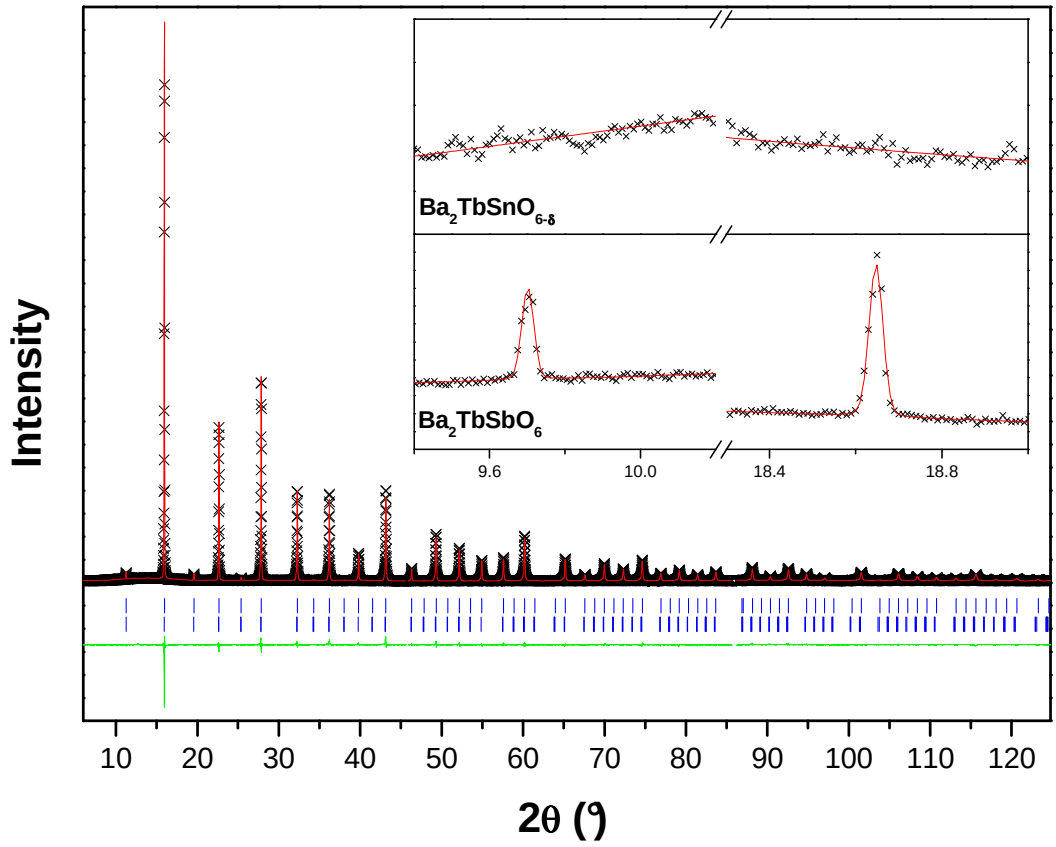

Figure 5.6: Synchrotron X-ray diffraction pattern of $Ba_2TbSnO_{6-\delta}$. The format is the same as for Figure 5.1. The insert displays the two lowest angle *R*-point super-lattice reflections of Ba_2TbSbO_6 and the same region of the diffraction pattern of $Ba_2TbSnO_{6-\delta}$ indicating that the former features B-site cation ordering while the B-site cations in the later are completely disordered.

Ting *et al.*[14] utilised a second "phase" *P*4/*mmm* model to account for the observed peak asymmetry and application of a similar model to the synchrotron X-ray and neutron diffraction patterns of $Ba_2TbSnO_{6-\delta}$ results in a significant improvement in the quality of the fits. This can be clearly seen by the vast improvement of R_p and R_{wp}

factors from 9.3 and 13.4 % to 4.9 and 6.2 % for a fit to the synchrotron X-ray diffraction data upon application of the second *P*4/*mmm* "phase" while a significant improvement in the quality of the fit to the neutron diffraction pattern is also obtained (R_p and R_{wp} of 6.2 and 7.7 % cf. to 5.6 and 6.8 % upon the application of the second "phase"). It is possible that the asymmetric peak shape of the diffraction pattern of $Ba_2TbSnO_{6-\delta}$ may be caused by the sample containing a small amount of another perovskite impurity. This seems unlikely since the asymmetry does not resolve into split peaks even at high angles in the synchrotron X-ray diffraction pattern. Additionally refinement of the peak shape parameters of the second phase against the synchrotron X-ray diffraction pattern yields a very broad peak shape rather than the sharp features that would be expected for a genuine perovskite impurity "phase" indicating it is more likely that this peak asymmetry is a result of strain in the sample.

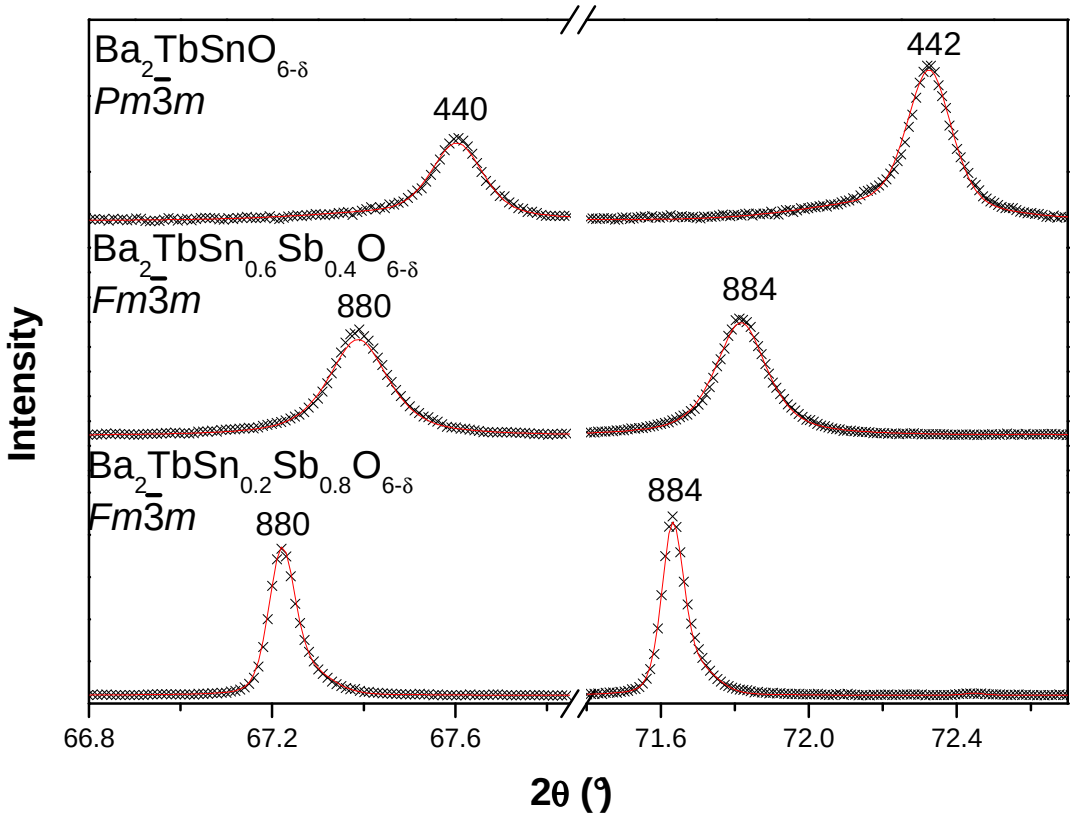

Figure 5.7: Selected regions of diffraction patterns of members in the series $Ba_2TbSn_xSb_{1-x}O_{6-\delta}$ indicating the lack of peak splitting revealing that these compounds are all cubic. The format is the same as Figure 5.2.

The smaller unit cell volume of $Ba_2TbSnO_{6-\delta}$ compared to Ba_2TbSbO_6 (cf. 73.8778(7) to 75.3947(8) $Å^3$ for $Ba_2TbSnO_{6-\delta}$ and Ba_2TbSbO_6 respectively) and the lack of cation order in $Ba_2TbSnO_{6-\delta}$ suggest that, similarly to $Ba_2PrSnO_{6-\delta}$, while Tb^{3+} is present in Ba_2TbSbO_6 the Tb in $Ba_2TbSnO_{6-\delta}$ is tetravalent. The change in bond lengths between Ba_2TbSbO_6 and $Ba_2TbSnO_{6-\delta}$ is also consistent with an oxidation state change from Tb^{3+} to Tb^{4+}. Refinement of models against neutron diffraction patterns show that the Tb-O bond length shortens from 2.2449(8) Å in Ba_2TbSbO_6 to 2.09963(4) Å in $Ba_2TbSnO_{6-\delta}$, which is a change of approximately 0.15 Å (see Tables 5.4 and 5.5 for crystallographic information and bond lengths respectively). This is very close to the 0.16 Å difference between the ionic radii of Tb^{3+} and Tb^{4+}, 0.92 and 0.76 Å respectively[6]. Similarly to the analogous Pr compounds Tb is overbonded in both structures with a bond valence sum of 3.53 and 5.23 for Ba_2TbSbO_6 and $Ba_2TbSnO_{6-\delta}$. The bond valence sums were determined using the parameter for a Tb^{3+}-O bond since the appropriate parameter for Tb^{4+} is unknown.

Table 5.4: Lattice parameters, atomic positions and displacement parameters for compounds in the series $Ba_2TbSn_xSb_{1-x}O_{6-\delta}$ as determined using neutron diffraction. In the case of the partially disordered $Ba_2TbSn_{0.8}Sb_{0.2}O_{6-\delta}$ structure the 4*a* site refines as containing 56(4) % Tb cations.

Compound Space Group	Ba_2TbSbO_6 $Fm\bar{3}m$	$Ba_2TbSn_{0.8}Sb_{0.2}O_{6-\delta}$ $Fm\bar{3}m$	$Ba_2TbSnO_{6-\delta}$ $Pm\bar{3}m$
a (Å)	8.4494(2)	8.4097(2)	4.19925(7)
Ba *B* ($Å^2$)	8*c* (¼,¼,¼) 0.49(2)	8*c* (¼,¼,¼) 0.64(3)	1*b* (½,½,½) 0.57(2)
Tb *B* ($Å^2$)	4*a* (0,0,0) 0.32(4)	4*a* (0,0,0) 0.40(3)	1*a* (0,0,0) 0.32(1)
B' *B* ($Å^2$)	4*b* (½,½,½) 0.20(4)	4*b* (½,½,½) 0.40(3)	1*a* (0,0,0) = Tb *B*
O *x* *B* ($Å^2$) Occupancy	24*e* (x,0,0) 0.2657(1) 0.82(2) 0.995(5)	24*e* (x,0,0) 0.2534(5) 1.00(2) 0.976(6)	3*d* (½,0,0) ½ 0.83(2) 0.986(7)
R_p % R_{wp} % χ^2	5.9 7.1 1.8	6.1 7.3 1.4	5.6 6.8 1.6

Refinements from neutron diffraction patterns of Ba_2TbSbO_6 and $Ba_2TbSnO_{6-\delta}$ have oxygen anion sites that are 99.5(5) and 98.6(7) % of full occupancy. While this is consistent with all Tb in Ba_2TbSbO_6 being trivalent it equates to a stoichiometry of $Ba_2TbSnO_{5.92(4)}$ for $Ba_2TbSnO_{6-\delta}$. This is equivalent to 83(8) % of the Tb in this compound being tetravalent with the remainder being trivalent. This is slightly lower than the average valency of Pr in $Ba_2PrSnO_{6-\delta}$, which neutron diffraction suggests is effectively all (95(8) %) tetravalent. Determination of oxygen occupancy by Rietveld refinement against neutron diffraction patterns, however, suffers from the strong cross-correlation between the occupancy and displacement parameters of a site particularly in data that do not cover an extensive range of *d*-spacing. An oxygen occupancy that is lower than the true value can be compensated for in the refinement by a smaller atomic displacement parameter. To determine a more accurate estimate of the oxidation state of cations, and thereby the level of oxygen vacancies, in compounds in the series $Ba_2LnSn_xSb_{1-x}O_{6-\delta}$ (Ln = Pr or Tb), samples were probed by other techniques as discussed in Section 5.4.1.4.

Table 5.5: Bond lengths and bond valence sums (BVS) for selected compounds in the $Ba_2TbSn_xSb_{1-x}O_{6-\delta}$ series determined from refinements using neutron diffraction patterns. The BVS for Tb is based on the Tb^{3+}-O parameter since the appropriate value for Tb^{4+} is not known. In the case of the mixed Sn^{4+} and Sb^{5+} structure the BVS for Sn^{4+} is listed above Sb^{5+}.

x	Ba-O		Tb-O		B'-O	
	Bond Length (Å)	BVS	Bond Length (Å)	BVS	Bond Length (Å)	BVS
0	12 × 2.9903(1)	1.81	6 × 2.2449(8)	3.53	6 × 1.9798(8)	5.42
0.8	12 × 2.9734(1)	1.89	6 × 2.131(4)	4.80	6 × 2.073(4)	3.81 4.21
1.0	12 × 2.9693(1)	1.91	6 × 2.0996(1)	5.23	= Tb-O	3.55

It has been determined that both Ba_2TbSbO_6 and $Ba_2TbSnO_{6-\delta}$ are cubic and that the Tb exists primarily as Tb^{3+} in the former and Tb^{4+} in the latter, causing the loss of B-site cation ordering and a change of symmetry from $Fm\bar{3}m$ to $Pm\bar{3}m$. Having established this, the series $Ba_2TbSn_xSb_{1-x}O_{6-\delta}$ was investigated using synchrotron X-ray and neutron diffraction to determine the point at which the transition occurs. Refinements reveal a gradual increase in B-site disorder with increased Sn^{4+} doping and that the transition occurs between x = 0.8 and 0.9. This is accompanied by a

gradual shortening of the Tb-O bond lengths and a lengthening of the Sn/Sb-O bonds such that the Tb-O and Sn/Sb-O bond lengths in $Ba_2TbSn_{0.8}Sb_{0.2}O_{6-\delta}$, the last ordered structure before the symmetry changes, are very similar (see Table 5.5). It should be mentioned that these refinements are carried out with the constraint that any disordering of the B-site cations involves both Sn^{4+} and Sb^{5+} replacing Tb in a ratio consistent with the composition of the compound (i.e. a partial occupancy of 0.2 of the Sn^{4+} and Sb^{5+} cation on the Tb site in $Ba_2TbSn_{0.6}Sb_{0.4}O_{6-\delta}$ denotes a partial occupancy of 0.12 and 0.08 for Sn^{4+} and Sb^{5+}). This constraint is necessary because Sn^{4+} and Sb^{5+} have similar neutron scattering lengths (cf. a coherent neutron scattering length of 6.225(2) fm for Sn^{4+} to 5.57(3) fm for Sb^{5+}[15]) and the same number of electrons, leading to very weak or no contrast in neutron and X-ray diffraction.

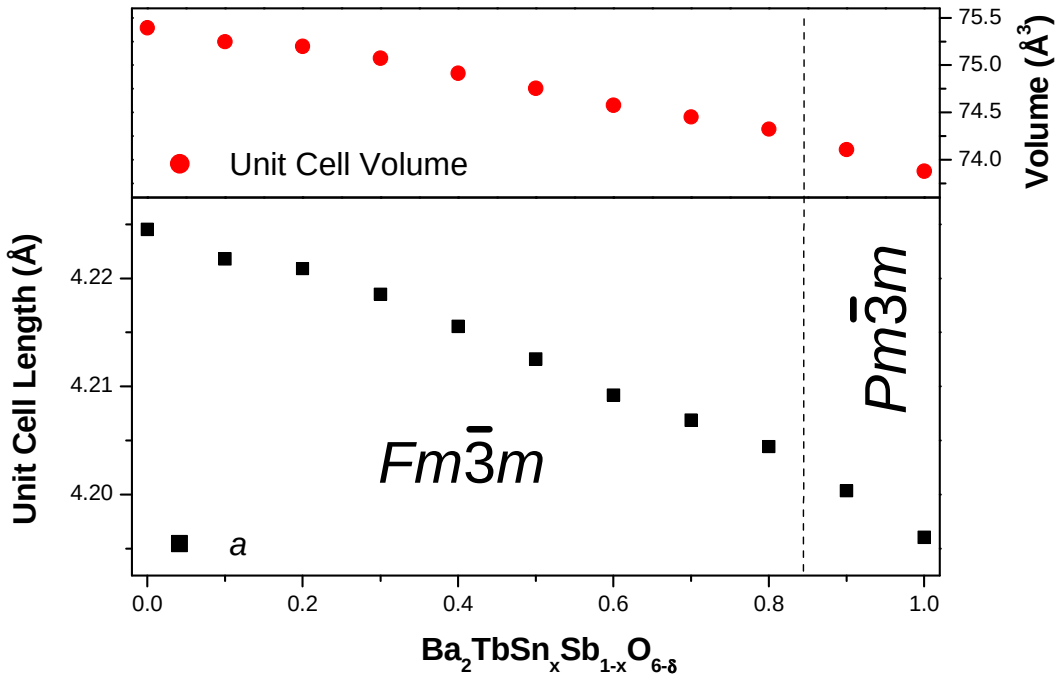

Figure 5.8: Reduced unit cell length and volume of members in the series $Ba_2TbSn_xSb_{1-x}O_{6-\delta}$.

The gradual change in B-site bond distances with increasing x suggests that the oxidation state change from Tb^{3+} to Tb^{4+} occurs gradually across the series rather than suddenly at a specific composition. This is consistent with the gradual decrease in unit cell length and volume observed with increasing x (see Figure 5.8 and Table 5.6). The peak asymmetry observed in $Ba_2TbSnO_{6-\delta}$ is also noticeable in a number of other

compounds in this series. In compositions where x = 0.2 to 0.4 the longer sloping tail of the asymmetric peaks, is on the higher angle (lower *d*-spacing) side of the peak, while in x = 0.8-1.0 the longer tail is on the lower angle (higher *d*-spacing) side of the peak (see Figure 5.7). Consequently in the x = 0.2 to 0.4 range of compositions the lattice parameters of the secondary "phase" are smaller than that of the main phase while in the 0.8-1.0 range they are larger. In the x = 0.5 to 0.7 range the peaks do not have a significantly asymmetric shape. The asymmetric peak shape found in these samples may provide an insight into the stresses present in these materials. The observation that the lattice parameters of the secondary "phase" are smaller than that of the main phase for the x = 0.2 to 0.4 samples suggests that the stress is most likely compressive. On the other hand the nature of the asymmetry in the x = 0.8-1.0 compounds suggests that tensile stress is dominant, while in the x = 0.5 to 0.7 samples, where there is no obvious peak asymmetry, a comparable mix of the two appears to be present. Why this should be the case is not obvious, although it may be related to the changing quantities of the four different sized B-site cations, Tb^{3+}, Tb^{4+}, Sn^{4+} and Sb^{5+}, throughout the series. The existence of stress in these complex oxides is not surprising either for the same reason.

Table 5.6: Unit cell parameters of compounds in the series $Ba_2TbSn_xSb_{1-x}O_{6-\delta}$ determined using synchrotron X-ray diffraction.

x	Space Group	*a* (Å)	Volume (Å^3)
0	$Fm\bar{3}m$	8.44909(5)	603.157(7)
0.1	$Fm\bar{3}m$	8.44361(6)	601.983(7)
0.2	$Fm\bar{3}m$	8.44181(3)	601.599(4)
0.3	$Fm\bar{3}m$	8.43707(4)	600.586(4)
0.4	$Fm\bar{3}m$	8.43112(4)	599.316(6)
0.5	$Fm\bar{3}m$	8.42509(5)	598.031(7)
0.6	$Fm\bar{3}m$	8.41840(8)	596.608(10)
0.7	$Fm\bar{3}m$	8.41375(6)	595.620(7)
0.8	$Fm\bar{3}m$	8.40886(5)	594.582(6)
0.9	$Pm\bar{3}m$	4.20034(7)	74.106(2)
1.0	$Pm\bar{3}m$	4.19602(2)	73.878(1)

5.4.1.3 Structural Analysis of XANES Standards

X-ray Absorption Near-Edge Structure (XANES) spectroscopy is an excellent probe for examining the oxidation state of ions in a compound independently of each other. This is done by determining the precise energy of the absorption edge of an element in a compound and then comparing this energy with that of an appropriate oxidation state standard, which ideally should have a similar co-ordination environment. In this work the L-edges of Pr, Tb, Sn and Sb are probed as the principal method for determining the oxidation states of these cations. For Sn SnO and SnO_2 were used as standards for Sn^{2+} and Sn^{4+} and similarly Sb_2O_3 and Sb_2O_5 were employed as standards for Sb^{3+} and Sb^{5+}. These compounds are all commercially available and were bought from Sigma Aldrich.

For Pr and Tb, however, there were no suitable commercially available standards for the trivalent and tetravalent oxidation states so suitable compounds had to be synthesised. In the case of the trivalent oxidation states $Pr_2Sn_2O_7$ and $Tb_2Sn_2O_7$ were selected. These compounds have the cubic pyrochlore structure in space group $Fd\bar{3}m$ where the Pr^{3+} and Tb^{3+} cations occupy an eight-fold co-ordination site in the channels between the SnO_6 octahedral framework[9]. While the eight-fold site is different from the octahedral co-ordination environment the B-site cations occupy in the perovskite structure it was the closest environment for a trivalent lanthanide that could be readily synthesised, which was suitable for use as an oxidation state standard. Refinements using synchrotron X-ray diffraction patterns confirm that $Pr_2Sn_2O_7$ and $Tb_2Sn_2O_7$ were obtained in pure form and have a unit cell length of 10.6072(10) and 10.42684(3) Å respectively. In $Pr_2Sn_2O_7$ Pr^{3+} is bonded to six oxygen anions with a bond length of 2.618(4) Å and two with a bond length of 2.29652(2) Å while in $Tb_2Sn_2O_7$ there are six Tb-O bonds with a length of 2.523(3) Å and two that are 2.25748(1) Å in length. The bond valence sums are 2.92 and 2.81 for Pr^{3+} and Tb^{3+}, respectively, in good agreement with the expected oxidation state.

Table 5.7: Lattice parameters, atomic positions and displacement parameters for $BaTbO_3$ at ambient temperature. The larger standard deviations in the *I*4/*mcm* tetragonal part of the two phase mixture are a result of it being the minor component.

Compound	$BaTbO_3$	
Space Group	*Ibmm*	*I*4/*mcm*
a (Å)	6.07212(4)	6.04512(5)
b (Å)	6.05410(4)	= *a*
c (Å)	8.54580(5)	8.59824(9)
Ba	4*e* (x,0,¼)	4*b* (½,0,¼)
x	0.5002(7)	½
B (Å^2)	0.64(2)	0.73(4)
Tb	4*a* (0,0,0)	4*c* (0,0,0)
B (Å^2)	0.29(1)	0.39(3)
O1	4*e* (x,0,¼)	4*a* (0,0,¼)
x	0.0550(21)	0
B (Å^2)	0.72(18)	0.21(20)
O2	8*g* (¼,¼,z)	8*h* (x,x+½,0)
x	¼	0.2654(60)
y	¼	0.7654(60)
z	0.9736(14)	0
B (Å^2)	0.85(13)	1.99(40)
R_p %	3.9	
R_{wp} %	5.2	
χ^2	355	

The perovskites $BaPrO_3$ and $BaTbO_3$ were selected for use as standards for Pr^{4+} and Tb^{4+} respectively. They were the ideal standards for XANES since the tetravalent lanthanides occupy the same octahedral environments in these standards as they do in the $Ba_2LnSn_xSb_{1-x}O_{6-\delta}$ compounds. A synchrotron X-ray diffraction pattern of $BaTbO_3$ was best fitted by a model using a combination of *Ibmm* orthorhombic (tilt system $a^-a^-c^0$) and *I*4/*mcm* tetragonal (tilt system $a^0a^0c^-$) structures where the orthorhombic phase was the most abundant. This result is consistent with the recent study carried out by Fu *et al.*[16], which reported the presence of a two phase mixture in $BaTbO_3$ just below ambient temperature as a result of the phase transition between orthorhombic and tetragonal symmetries. The refinement revealed an average bond distance of 2.16(2) and 2.144(1) Å for the orthorhombic and tetragonal structures respectively (see Tables 5.7 and 5.8 for crystallographic information and selected bond distances respectively) very close to the value of 2.16 Å expected from the sum of the ionic radii for a Tb^{4+}-O bond[6]. The co-existence of these two phases is not believed to impact upon the use of this as an oxidation state standard since in both

phases the Tb^{4+} environment is essentially identical. The structural parameters determined in this work are very similar to that of Fu *et al.*[16] although they found that $BaTbO_3$ had completed its phase transition to the tetragonal structure at ambient temperature. This minor discrepancy is most likely due to the sample used in the work of Fu *et al.*[16] being synthesised in air while the sample used in the work presented in this thesis was annealed in flowing oxygen during the last stage of the heating process to ensure that it was stoichiometric with respect to oxygen content[10, 11].

Table 5.8: Selected bond distances and bond valence sums (BVS) for $BaTbO_3$ at ambient temperature.

Phase	Ba-O			Tb-O	
	Bond Length (Å)		BVS	Bond Length (Å)	BVS
Ibmm	1 × 2.7032(1) 4 × 2.871(27) 2 × 3.0456(1)	4 × 3.190(24) 1 × 3.3689(2)	1.82	2 × 2.1624(1) 4 × 2.155(4)	4.47
*I*4/*mcm*	4 × 2.940(35) 4 × 3.0226(1) 4 × 3.126(37)		1.66	2 × 2.1496(2) 4 × 2.141(3)	4.64

A synchrotron X-ray diffraction pattern of $BaPrO_3$ obtained at room temperature was well fitted using a model with orthorhombic *Pbnm* symmetry (tilt system $a^-a^-c^+$). There was clear evidence for *M*-, *R*- and *X*-point super-lattice reflections confirming that it adopts *Pbnm* symmetry consistent with earlier reports[17, 18] (see Figure 5.9). The structure of $BaPrO_3$ above room temperature, however, was unknown. Most other $A^{2+}B^{4+}O_3$ perovskites[19], including $BaTbO_3$[16] adopt the series of phase transitions from *Pbnm* orthorhombic to *Ibmm* orthorhombic to *I*4/*mcm* tetragonal to the untilted $Pm\bar{3}m$ cubic structure although not all are known to adopt the *Ibmm* intermediate phase. The only $A^{2+}B^{4+}O_3$ perovskite known to adopt a different series of phase transitions is $BaCeO_3$ which adopts the $R\bar{3}c$ rhombohedral space group (tilt system $a^-a^-a^-$) between *Ibmm* and $Pm\bar{3}m$ symmetry instead of the tetragonal structure[20]. Since Pr^{4+} has a very similar size, electronegativity and electronic configuration to Ce^{4+} it is worth investigating the phase transitions undertaken by $BaPrO_3$ with increasing temperature to determine if it adopts the tetragonal or rhombohedral intermediate.

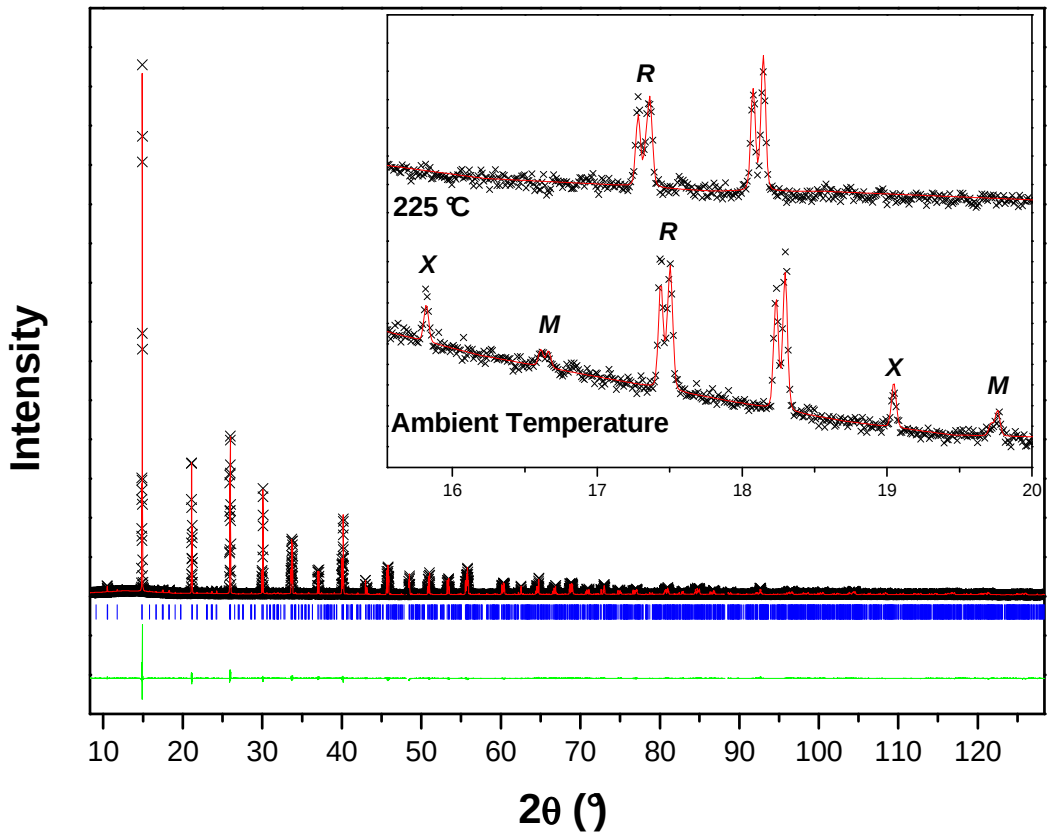

Figure 5.9: Synchrotron X-ray diffraction pattern of $BaPrO_3$ at ambient temperature. The insert displays a region of two diffraction patterns of $BaPrO_3$, one collected at ambient temperature and the other at 225 °C, revealing the different super-lattice reflections present at these temperatures. The format is the same as in Figure 5.1.

Above 200 °C the diffraction patterns of $BaPrO_3$ no longer contained any *M*- or *X*-point super-lattice reflections (see Figure 5.9). This denotes a phase transition occurs near 200 °C from *Pbnm* to *Ibmm* symmetry. There is a change in slope of the lattice parameters with increasing temperature in this region consistent with a continuous phase transition. As can be seen in Figure 5.10 the rate of increase in the length of the *a*-axis decreases significantly in this region while that of the *c*-axis increases confirming the temperature range of this phase transition has been assigned correctly. At 400 °C there is evidence for the coexistence of a second phase with the *Ibmm* orthorhombic phase. This two phase region exists in the range of 400-475 °C with a gradual decrease in the amount of orthorhombic phase present with increasing temperature until at 500 °C only the second phase remains. Peak splitting in this second phase is consistent with a rhombohedral structure indicating that this phase

adopts $R\bar{3}c$ symmetry. Excellent fits are achieved using this structure, both as a single phase model above 500 °C and as part of a two phase fit with an *Ibmm* orthorhombic structure in the two phase region (see Figure 5.11). $R\bar{3}c$ rhombohedral symmetry is maintained up to 800 °C, which is the maximum temperature available for this work.

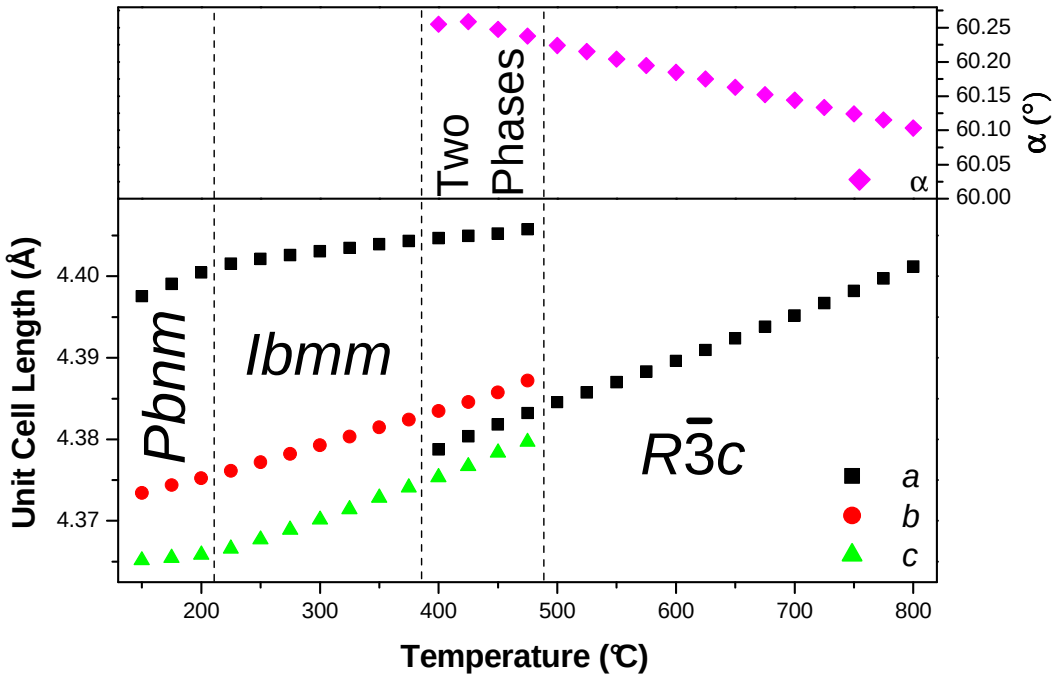

Figure 5.10: Reduced unit cell parameters for $BaPrO_3$ over a temperature range of 150-800 °C.

$BaPrO_3$ undergoes the same series of phase transitions as $BaCeO_3$ changing from *Pnma* to *Ibmm* to $R\bar{3}c$ and, presumably, to $Pm\bar{3}m$ with increasing temperature. $BaPrO_3$ is only the second example of an $A^{2+}B^{4+}O_3$ perovskite found to adopt rhombohedral symmetry as an intermediate between orthorhombic symmetries and the ideal cubic perovskite structure. The ionic radius of Pr^{4+}, while slightly smaller than Ce^{4+} (cf. an ionic radii of 0.85 Å for Pr^{4+} to 0.87 Å for Ce^{4+}[6]) is significantly larger than any of the B-site cations in $A^{2+}B^{4+}O_3$ perovskites that adopt the tetragonal intermediate. The electronegativity of Pr^{4+}, on the other hand is larger than both Ce^{4+} and Zr^{4+}, which adopt the two alternate intermediates but is smaller than that of other B^{4+} cations found in tetragonal perovskites[21]. This suggests that it is the larger size of Ce^{4+} and Pr^{4+} that causes perovskites with these cations to adopt the rhombohedral, rather than the alternate tetragonal, structure. This is a similar result to that presented

in Chapter 3 for the double perovskites $Ba_2LnB'O_6$ (Ln = lanthanide and B' = Nb^{5+} or Ta^{5+}), which found that compounds in the series $Ba_2LnB'O_6$ that contain the larger lanthanides, La^{3+} and Pr^{3+}, adopt a $R\bar{3}$ rhombohedral intermediate between monoclinic and cubic symmetries while the rest of the series adopt an *I*4/*m* tetragonal phase. The rhombohedral and tetragonal space groups in both the ternary and double perovskites correspond to the same two tilt systems, $a^-a^-a^-$ and $a^0a^0c^-$ respectively, and the results from both these two studies provide a strong indication that the ionic radius of the B-site cation plays a role in determining which of these two tilt systems is adopted.

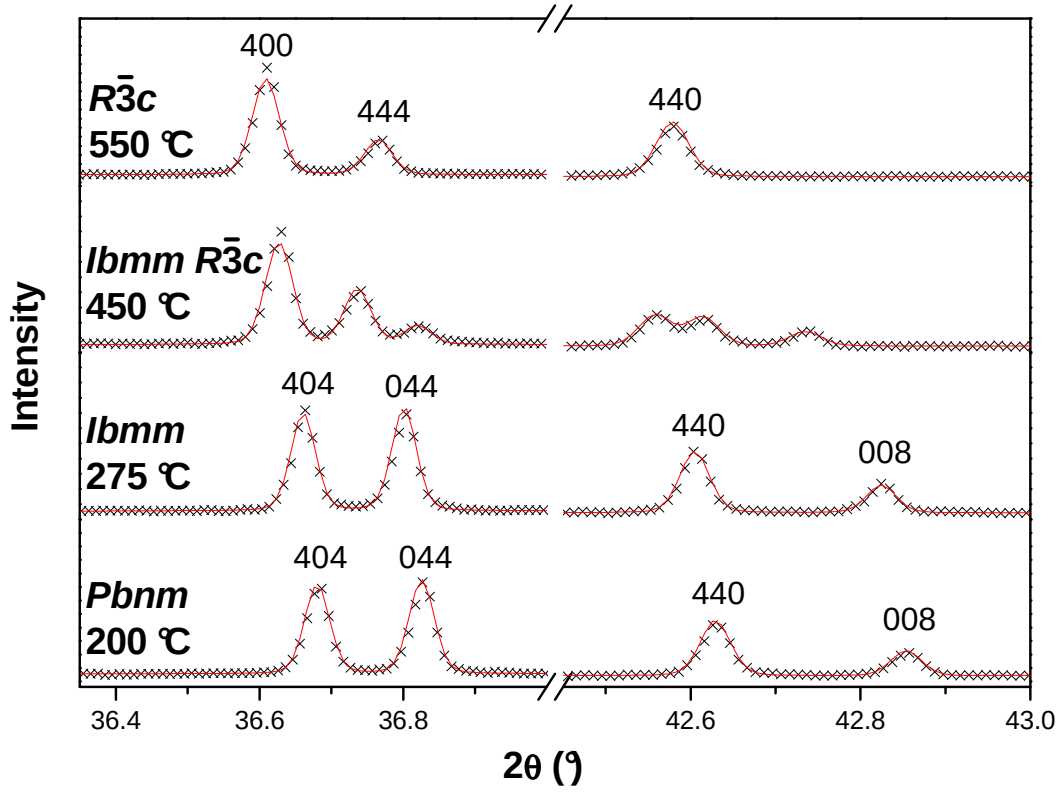

Figure 5.11: Selected regions of diffraction patterns of $BaPrO_3$ collected at different temperatures indicating the various phases it adopts.

Refinements show that the average Pr-O bond length does not change significantly over the large temperature range examined and is very close to the value of 2.25 Å expected for a Pr^{4+}-O bond (see Tables 5.9 and 5.10 for crystallographic details and selected bond lengths respectively). The Pr-O octahedra does not distort significantly in either *Pbnm* or *Ibmm* symmetry, although these space groups do not require it to have O_h symmetry. On the other hand while the average Ba-O bond length also

remains approximately the same with temperature as the octahedral tilting decreases the Ba^{2+} bond valence sum appears to decrease significantly from 1.76 at room temperature to 1.45 at 800 °C. This apparent decrease in Ba-O bonding strength occurs because of the exponential relationship of bonding strength with distance. It should, however, be noted these bond valencies are determined based on the bond valence parameters determined for a cation and anion combination at ambient temperature, as is routinely done in the literature, and are likely to not be applicable at higher temperatures. Indeed using the method developed by Brown *et al.*[22] to calculate bond valence parameters above ambient temperature it was found that the bond valence sum of the Ba-O bond is approximately 1.8 at all temperatures examined. Thus while the bonding environment of the Ba^{2+} cation changes significantly with increasing temperature the overall bonding strength, despite initial appearances, appears to remain the same.

Table 5.9: Crystallographic details for the various structures adopted by $BaPrO_3$ at different temperatures.

Temperature Space Group	Ambient *Pbnm*	375 °C *Ibmm*	500 °C $R\bar{3}c$	800 °C $R\bar{3}c$
a (Å)	6.21318(2)	6.22862(3)	6.20069(2)	6.2245(2)
b (Å)	6.18120(2)	6.19776(3)	= *a*	= *a*
c (Å)	8.72859(3)	8.74819(4)	= *a*	= *a*
α (°)	90	90	60.2241(4)	60.1015(4)
Ba	4*c* (x,y,¼)	4*e* (x,0,¼)	2*a* (¼,¼,¼)	2*a* (¼,¼,¼)
x	0.0040(2)	0.5022(3)	¼	¼
y	0.5133(1)	0	¼	¼
B (Å^2)	0.76(1)	1.23(1)	1.45(2)	2.20(1)
Pr	4*a* (0,0,0)	4*a* (0,0,0)	2*b* (0,0,0)	2*b* (0,0,0)
B (Å^2)	0.36(1)	0.28(1)	0.43(1)	0.73(1)
O1	4*c* (x,y,¼)	4*e* (x,0,¼)	6*e* (x,½-x,¼)	6*e* (x,½-x,¼)
x	-0.0684(9)	0.0590(15)	0.6944(9)	0.7071(8)
y	0.9886(12)	0	0.8056(9)	0.7929(8)
B (Å^2)	0.89(8)	1.48(21)	2.47(14)	3.90(12)
O2	8*d* (x,y,z)	8*g* (¼,¼,z)		
x	0.2271(9)	¼		
y	0.2778(9)	¼		
z	0.0392(5)	-0.0346(8)		
B (Å^2)	0.74(6)	1.86(16)		
R_p %	3.7	6.3	6.4	4.3
R_{wp} %	4.3	8.0	8.9	6.1
χ^2	213	205	329	217

Table 5.10: Bond distances and bond valence sums (BVS) for $BaPrO_3$ at various temperatures. The corrected BVS values are calculated according to the methodology of Brown *et al*.[22].

Temperature (°C)	Ba-O				Pr-O	
	Bond Length (Å)		BVS	Corrected BVS	Bond Length (Å)	BVS
Ambient	1 × 2.711(6) 2 × 2.725(5) 1 × 2.972(7) 2 × 2.975(5)	2 × 3.178(4) 1 × 3.274(7) 1 × 3.510(6) 2 × 3.545(5)	1.77	1.77	2 × 2.209(6) 2 × 2.224(1) 2 × 2.248(6)	4.68
375	1 × 2.760(10) 4 × 2.887(5) 2 × 3.122(1)	4 × 3.326(5) 1 × 3.468(10)	1.57	1.75	2 × 2.231(3) 4 × 2.259(4)	4.80
500	3 × 2.7649 (1) 6 × 3.120(5) 3 × 3.4568(1)		1.59	1.83	6 × 2.223(7)	4.73
800	3 × 2.8492(1) 6 × 3.124(5) 3 × 3.3845(1)		1.45	1.80	6 × 2.218(7)	4.79

It has been shown in this section that suitable standards for trivalent and tetravalent Pr and Tb have been synthesised and then characterised using synchrotron X-ray diffraction. Results from this have shown that they are high quality samples and have structures consistent with the expected oxidation states. These standards were therefore suitable be used for XANES analysis of the oxidation states of the lanthanide cations.

5.4.1.4 Analysis of Oxygen Vacancies and Oxidation States of Cations in $Ba_2LnSn_xSb_{1-x}O_{6-\delta}$

The structural analysis of compounds in the series $Ba_2LnSn_xSb_{1-x}O_{6-\delta}$ (Ln = Pr or Tb) carried out using a combination of synchrotron X-ray and neutron diffraction provided a strong indication that as x increases the lanthanide cations change from the trivalent to tetravalent states reducing or eliminating the need for oxygen vacancies to form. Diffraction techniques, however, are not reliable methods for quantifying the oxidation states of cations in complex materials. Even when an accurate structural model of the compound has been determined estimates of oxidation states rely on calculating bond lengths in a compound and then comparing these to “average” values that are based on a wide range of materials. Since the nature of the bonding between a

specific cation and anion combination can vary significantly between different compounds, due to different co-ordination environments and competing bonding interactions, use of average bond lengths and bond valence sums are not accurate and precise measures of the oxidation state of a cation. Furthermore while, when high quality neutron diffraction patterns are available, it is possible to quantify oxygen occupancy and thereby directly determine the oxygen stoichiometry of a compound, the cross-correlation between occupancy and displacement parameters may result in a measurement with poor accuracy.

In the work presented in this section the oxidation states, and thereby the amount of oxygen vacancies, in the series $Ba_2LnSn_xSb_{1-x}O_{6-\delta}$ have been analysised using three techniques that are applicable for use on a large number of samples and provide an estimate of oxidation states independently of structural modelling. The first of these techniques to be utilised was UV-Vis-NIR spectroscopy. These measurements afforded a rapid qualitative examination of the way the oxidation states of Pr and Tb change with increased Sn^{4+} doping. The 1200-1900 nm region of the Near-Infrared spectra of $Ba_2PrSn_xSb_{1-x}O_{6-\delta}$ reveals that the many sharp peaks present in Ba_2PrSbO_6 are replaced in the spectrum of $Ba_2PrSnO_{6-\delta}$ by fewer, broader and more intense features (see Figure 5.12). These features corresponds to low lying transitions between the 4*f* orbitals, and the sharp features in the Ba_2PrSbO_6 spectrum and the broad features in the $Ba_2PrSnO_{6-\delta}$ were well established as being typical of Pr^{3+} and Pr^{4+} respectively[23-25]. The Near-Infrared spectra of $Pr_2Sn_2O_7$ and $BaPrO_3$ were also found to be similar to those of Ba_2PrSbO_6 and $Ba_2PrSnO_{6-\delta}$ respectively. This confirms the oxidation states of Pr in these compounds although the intensity and precise energy of some features vary significantly between spectra of the Ba_2PrSbO_6 and $Ba_2PrSnO_{6-\delta}$ compounds and the Pr^{3+} and Pr^{4+} standards. The change in the intensity of these features between the two end-members of the $Ba_2PrSn_xSb_{1-x}O_{6-\delta}$ series appears to be gradual, providing a strong indication that the oxidation state changes from Pr^{3+} to Pr^{4+} smoothly across the series. Unfortunately a subtle change in the energy of some of the features associated with Pr^{3+} and particularly Pr^{4+} with increased Sn^{4+} doping prevents a least squared fit of the two end-members being used to obtain a quantitative estimate of the amount of Pr^{3+} and Pr^{4+} in the intermediate compounds.

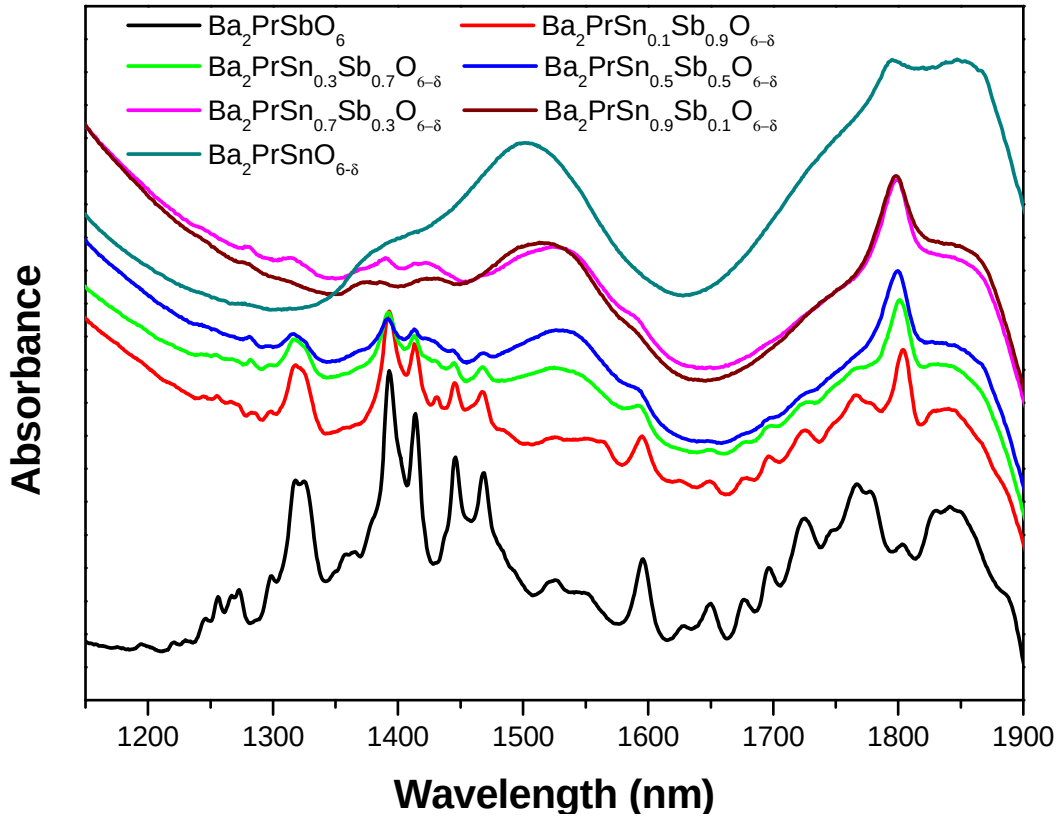

Figure 5.12: Near-Infrared spectra of selected compounds in the series $Ba_2PrSn_xSb_{1-x}O_{6-\delta}$ in the region 1150-1900 nm.

There were also significant changes in the 300-500 nm region of the spectra of compounds in the series $Ba_2PrSn_xSb_{1-x}O_{6-\delta}$ with the absorption feature in this region increasing in intensity as x increases (see Figure 5.13). Absorption in this energy range is likely to be caused by a combination of $4f^2 \rightarrow 4f^15d^1$ and band gap transitions making it difficult to use this region to probe the oxidation state of Pr[23-25]. The $4f^2 \rightarrow 4f^15d^1$ transitions of Pr^{4+} are known to be lower in energy than those of Pr^{3+} so the broadening of the absorption features in this region with increased Sn^{4+} doping is consistent with a change in oxidation state from Pr^{3+} to Pr^{4+}[24]. Weak absorption features are also noticeable at approximately 450 nm and 600 nm in the spectrum of Ba_2PrSbO_6. These are in the appropriate region for transitions between low lying and high energy *f*-orbitals and are not seen in the spectra of other compounds in the $Ba_2PrSn_xSb_{1-x}O_{6-\delta}$ series[23, 25]. This is most likely due to the broadening of the main absorption feature in this region leading to it overlapping with these peaks and, due to its much greater intensity, obscuring these weaker features.

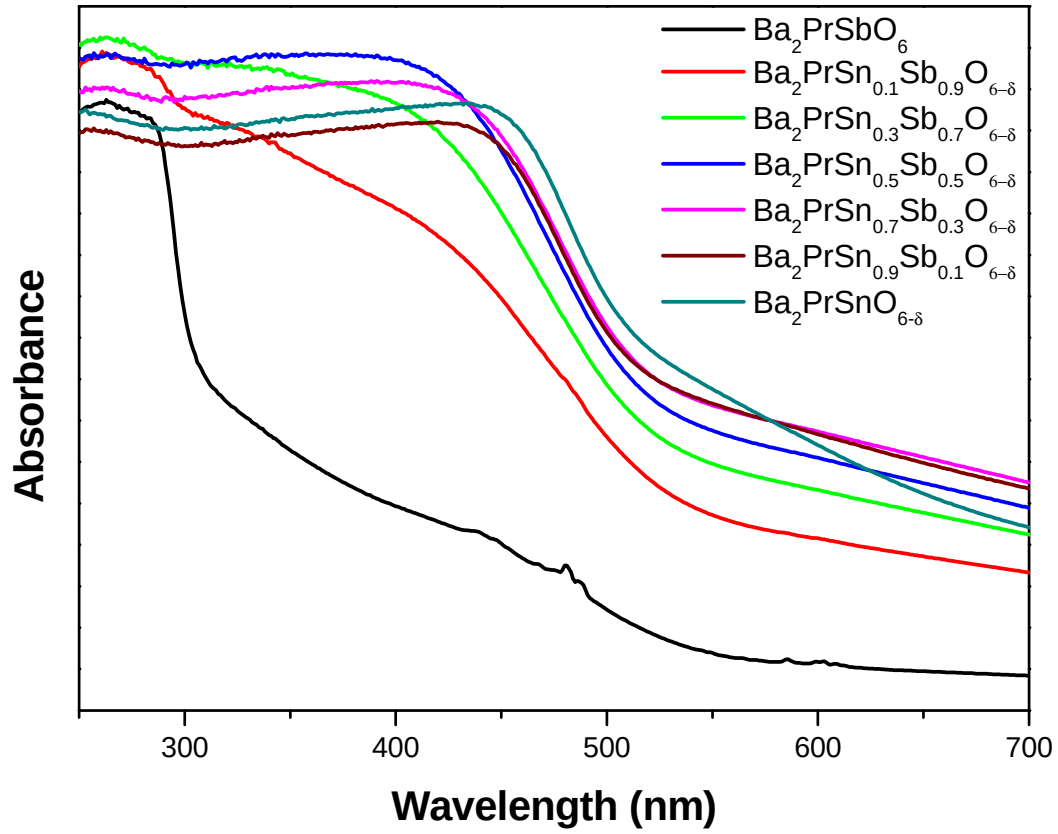

Figure 5.13: UV-Vis spectra of selected compounds in the series $Ba_2PrSn_xSb_{1-x}O_{6-\delta}$ in the region 250-700 nm.

Examination of the 1500-2200 nm region of the spectra of compounds in the series $Ba_2TbSn_xSb_{1-x}O_{6-\delta}$ reveals a significant loss in the intensity of the sharp features in Ba_2TbSbO_6 with Sn^{4+} doping, with these features being almost indistinguishable from the background at intermediate compositions (see Figure 5.14). These sharp features are consistent with those found in the Near-Infrared region of $Tb_2Sn_2O_7$ and are typical of those of Tb^{3+}[26, 27]. The loss of intensity of these features is consistent with the transition from Tb^{3+} to Tb^{4+} across the series, although it is unclear why the loss of these features occurs suddenly with Sn^{4+} doping while the structural data and XANES spectra, which are subsequently presented, suggest a gradual change in the oxidation state. Unlike $Ba_2PrSnO_{6-\delta}$, $Ba_2TbSnO_{6-\delta}$ appears to have no spectral features in this region that are distinguishable from the background. $BaTbO_3$ does not have any significant spectral features in this region either, confirming that Tb^{4+} is virtually featureless in the Near-Infrared.

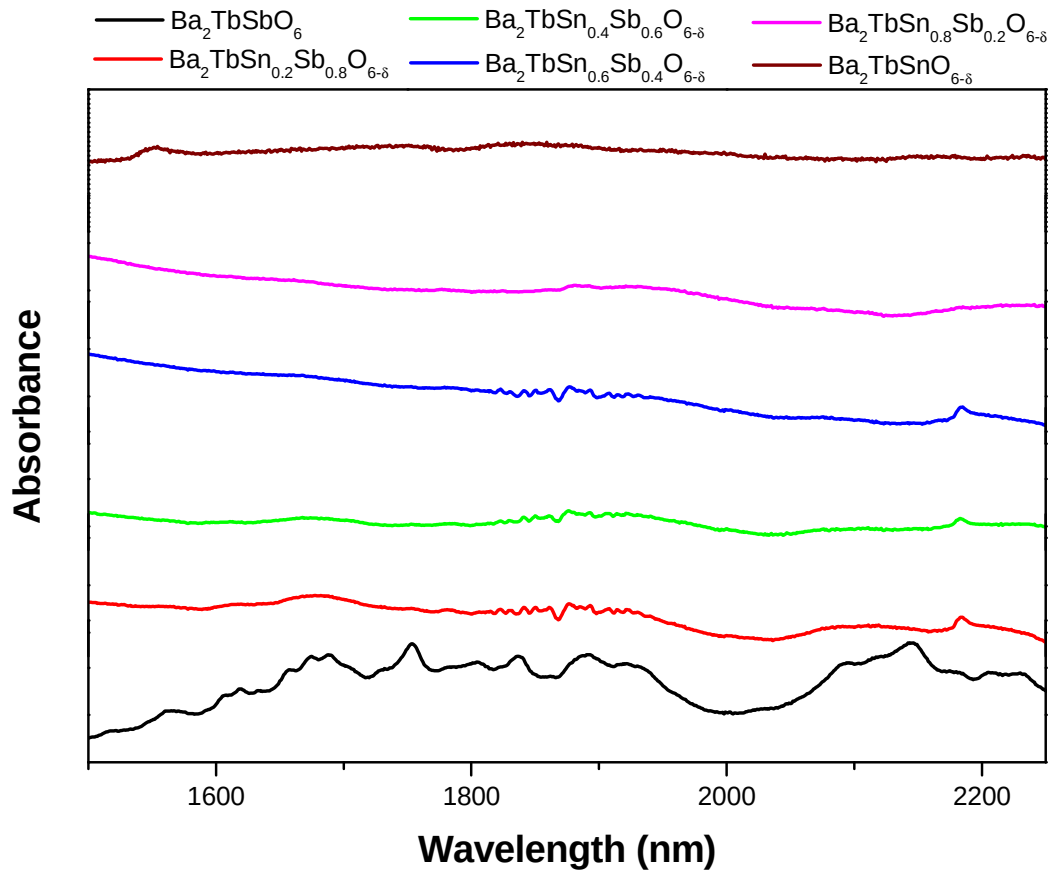

Figure 5.14: Near-Infrared spectra of compounds in the series $Ba_2TbSn_xSb_{1-x}O_{6-\delta}$ in the region of 1500-2250 nm.

As was found for $Ba_2PrSn_xSb_{1-x}O_{6-\delta}$, spectra of compounds in the series $Ba_2TbSn_xSb_{1-x}O_{6-\delta}$ also have a broad peak in the region of 300-500 nm that widens with increased Sn^{4+} doping. It is known that Tb^{3+} $4f^2 \rightarrow 4f^15d^1$ transitions occur in the near UV region[26]. Since it would be expected that, similarly to Pr^{4+}, the Tb^{4+} $4f^2 \rightarrow 4f^15d^1$ transitions would be lower in energy than Tb^{3+} the broadening of the absorption features in this region with increased Sn^{4+} doping is consistent with Tb^{3+} oxidising to Tb^{4+}, thereby reducing the amount of oxygen vacancies present.

Having utilised UV-Vis-NIR spectroscopy to qualitatively confirm the change in oxidation state of Pr^{3+} and Tb^{3+} to Pr^{4+} and Tb^{4+} with increased Sn^{4+} doping, attempts were made to use Thermogravimetric Analysis (TGA) to quantitatively determine the oxygen stoichiometry of compounds in the series $Ba_2LnSn_xSb_{1-x}O_{6-\delta}$. These measurements were conducted by David Cassidy at ANSTO in association with this work. Examining the oxygen stoichiometry of compounds using this approach relies

on being able to fully reduce all the cations present to either a metallic state or, when this is not possible under the conditions available, to a stable lower oxidation state. The success of this technique relies on having a temperature region where there is a significant weight loss followed by a plateau. In both $Ba_2PrSnO_{6-\delta}$ and $Ba_2TbSnO_{6-\delta}$ while there was significant weight loss between 450 and 800 °C the samples never reached a constant weight, thus making it difficult to use this technique to estimate the oxygen stoichiometry of these compounds (see Figure 5.15). If it is assumed that the slope in the weight loss in this post-edge region is entirely caused by buoyancy effects, the validity of which may be questionable, a weight loss can be determined that is approximately consistent with the reduction of all the Pr in $Ba_2PrSnO_{6-\delta}$ from Pr^{4+} to Pr^{3+} consistent with the diffraction and spectroscopic data. A similar analysis of the weight change in $Ba_2TbSnO_{6-\delta}$, however, leads to a loss that is too high to be consistent with the reduction of Tb^{4+} to Tb^{3+} but is too low for the full reduction of any other cation to its next lowest stable oxidation state.

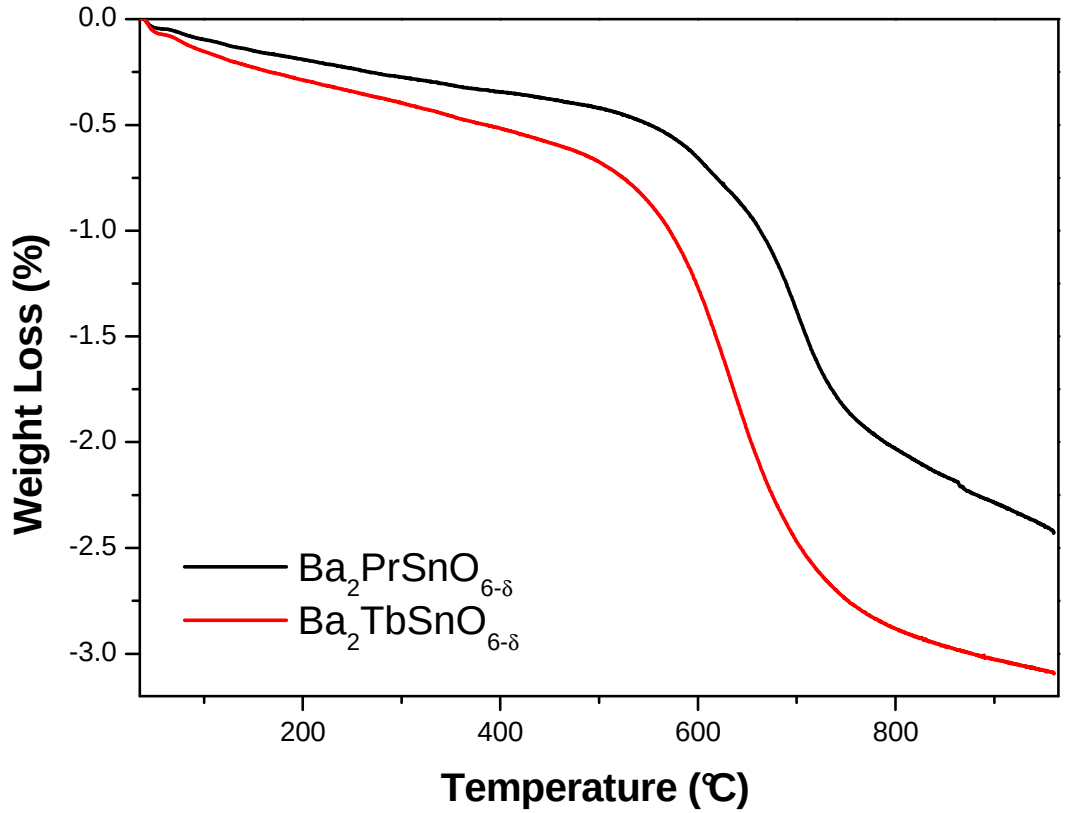

Figure 5.15: Weight loss versus temperature plots for $Ba_2PrSnO_{6-\delta}$ and $Ba_2TbSnO_{6-\delta}$ in an atmosphere of 3.5 % H_2 in N_2. The weight loss between 450 and 800 °C is 1.65 and 2.30 % of initial weight for $Ba_2PrSnO_{6-\delta}$ and $Ba_2TbSnO_{6-\delta}$ respectively.

Given the problems with utilising TGA to examine the compounds of interest it was necessary to use another technique to quantitatively assess the oxygen stoichiometry and the oxidation state of elements in $Ba_2LnSn_xSb_{1-x}O_{6-\delta}$. X-ray Absorption and Near-Edge Structure (XANES) spectroscopy was used to probe the oxidation state of the various cations present. Since in metal oxides Ba cations are almost invariably divalent it was not necessary to investigate Ba using XANES spectroscopy leaving Sn, Sb, Pr and Tb to be examined[28]. The L-edges of these cations were selected for examination because of the high sensitivity of these transitions to the oxidation state of these cations. Additionally the energy of the L-edges is more easily accessible using the available synchrotrons than that of the K-edges, particularly in the case of the lanthanide cations which have K-edges at approximately 42 and 52 keV for Pr and Tb respectively.

The analysis of the L-edges of Sn and Sb is complicated as a result of all six edges of these elements occurring in the narrow energy range of 3.9-4.7 keV[29]. This leads to extensive overlap of the Sn L_{II}- and Sb L_{III}-edges, which occur at 4.156 and 4.132 keV respectively, making analysis of these edges in mixed Sn and Sb compounds very difficult. More importantly the Sn L_I- and Sb L_{II}-edges (present at 4.465 and 4.380 keV) overlap, although not to as severe an extent. This is particularly problematic in the case of the Sn L_I-edge as this is the edge that is ideally suited for analysis of the oxidation state of Sn. This is because, similar to the Sb L_I- edge, it is the simplest and most sensitive L-edge to any change in oxidation state[29-31]. The high sensitivity of the L_I-edge to the oxidation state of Sn and Sb is a result of this transition occurring between the 2*s* and the 5*p* states whose energy depends on the presence or absence of 5*s* electrons.

The problem of using the L_I-edge to determine the oxidation state of Sn, however, was overcome by examining a combination of the Sn L_I- and L_{III}-edges; the later being free from overlap with any Sb L-edge. The Sn L_{III}-edge spectra of compounds in the series $Ba_2PrSn_xSb_{1-x}O_{6-\delta}$ and of the three Sn doped $Ba_2TbSn_xSb_{1-x}O_{6-\delta}$ (x = 0.3, 0.7 and 1.0) samples investigated were very similar suggesting that Sn has the same oxidation state in all of these compounds (see Figure 5.16). These spectra were, however, quite different from those of SnO and SnO_2 (which were selected to be used

as Sn^{2+} and Sn^{4+} oxidation state standards). The main peak in the Sn L_I absorption edge (also known as a white line) occurred at approximately 4.471 keV in all samples (see Figure 5.17). This edge energy is similar to that measured for SnO_2 and no features were observed corresponding to SnO. There was, however, another feature that increased in intensity with Sb doping at approximately 4.46 keV. This feature corresponds to a peak in the Sb L_{II} post-edge spectra. Since all Sn L_{III}-edges appear the same and the energy of the Sn L_I-edge does not change with increased Sn doping it would seem unlikely that there are any significant features in the Sn L_I-edge that are obscured by this interference. It is concluded from the Sn L-edges XANES that Sn adopts a tetravalent oxidation state in these two perovskite series, with no indication of any fraction of Sn^{2+} being present. The disparity between the perovskite spectra and that of SnO_2 reflects the different co-ordination environment for Sn^{4+} in these two structures. This illustrates the high degree of sensitivity of XANES to co-ordination environment since Sn^{4+} is 6-fold co-ordinate in both the perovskite and rutile SnO_2 structure[32]. It is somewhat surprising that subtle differences between the octahedral environment in the perovskite and rutile structures are sufficient to cause such a significant difference in the XANES spectra of the samples and the SnO_2 standard.

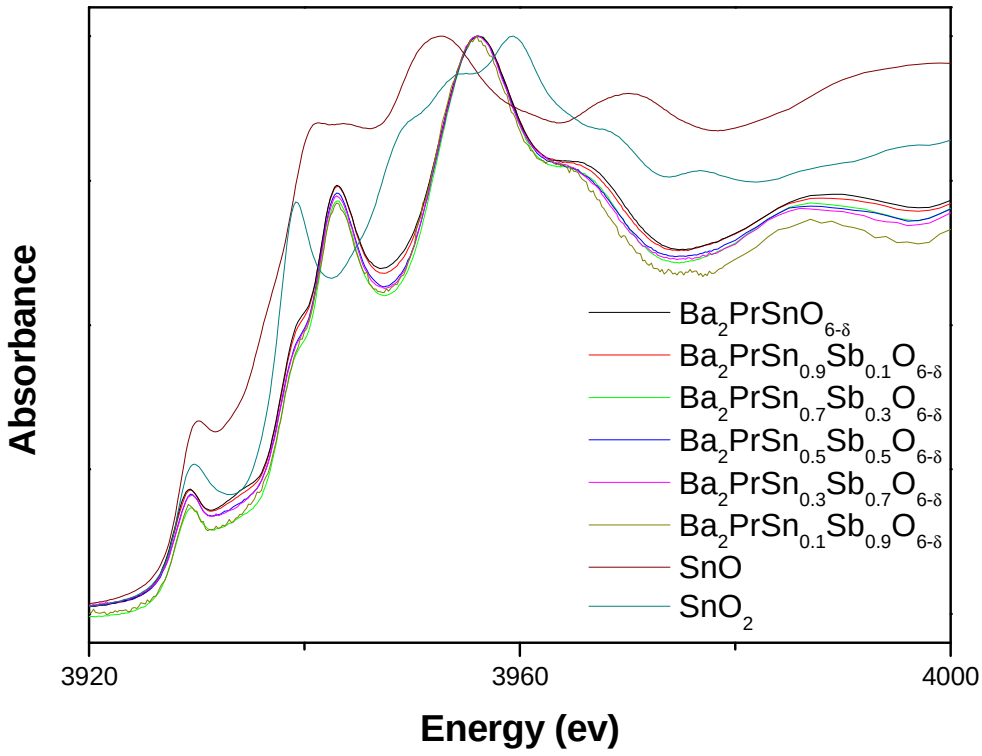

Figure 5.16: Sn L_{III}-edges of selected samples in the series $Ba_2PrSn_xSb_{1-x}O_{6-\delta}$ and, the Sn^{2+} and Sn^{4+} standards, SnO and SnO_2.

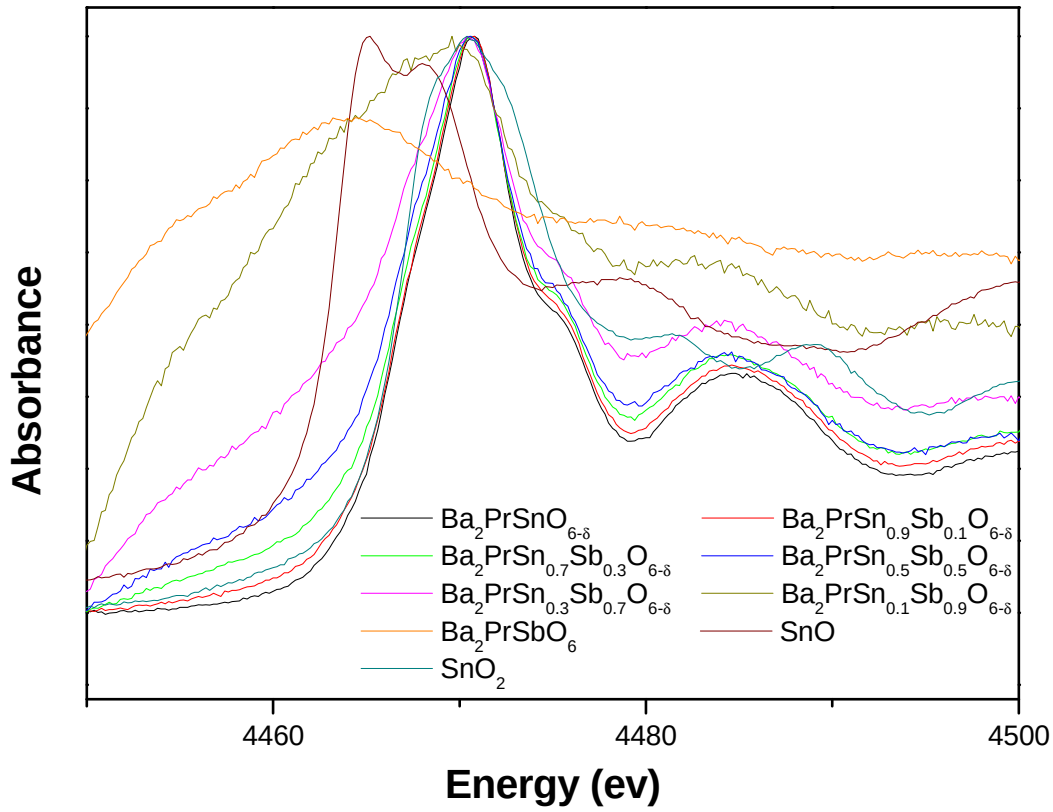

Figure 5.17: Sn L_I-edges of selected samples in the series $Ba_2PrSn_xSb_{1-x}O_{6-\delta}$ and, the Sn^{2+} and Sn^{4+} standards, SnO and SnO_2. A rescaled spectrum of Ba_2PrSbO_6 is also included as a reference for the features of the Sb L_{II} post-edge region.

The Sn L_I-edge of samples of $Ba_2PrSnO_{6-\delta}$ and $Ba_2TbSnO_{6-\delta}$ that were heated in an atmosphere of 5 % H_2 in Ar have an additional shoulder at the low energy side of Sn-edge (see Figure 5.18). This feature occurs at 4.464 keV, which is at approximately the same energy as the SnO edge. This suggests that these reduced compounds contain a significant amount of Sn^{2+}. A least squares fit of the SnO and SnO_2 edges to the edges of these reduced samples over the range of 4.450- 4.480 keV was carried out to determine what fraction of the Sn^{4+} in these samples was reduced to Sn^{2+}. The results from this analysis reveal that samples of $Ba_2PrSnO_{6-\delta}$ and $Ba_2TbSnO_{6-\delta}$ that were heated up to 800 °C under reducing conditions at a rate of 5 °/min, analogous to the conditions used for the TGA, and then immediately cooled contained approximately 15 % Sn^{2+} and 85 % Sn^{4+}. The analysis also showed that continued heating of a sample of $Ba_2TbSnO_{6-\delta}$ at 800 °C for 24 hrs resulted in a Sn^{2+} content of about 20 %. Evidently reduction of Sn^{4+} in these samples initially occurs rapidly but decreases significantly over time. Alternatively more Sn^{2+} may form under

these conditions than suggested by the XANES spectra but then rapidly re-oxidise on exposure to air. The unexplained magnitude of the weight loss indicated by TGA for $Ba_2TbSnO_{6-\delta}$ would appear to consistent with the hypothesis that some, but not all, of the Sn^{4+} is reduced after 24 hrs of reduction and this suggests that TGA is not a valid technique for examining oxygen stoichiometry in these two perovskite series. It should be noted that a similar least squared fit to the XANES region of the as synthesised $Ba_2PrSnO_{6-\delta}$ and $Ba_2TbSnO_{6-\delta}$ compounds does not point to the presence of any Sn^{2+} in these compounds confirming that they only contain Sn^{4+}.

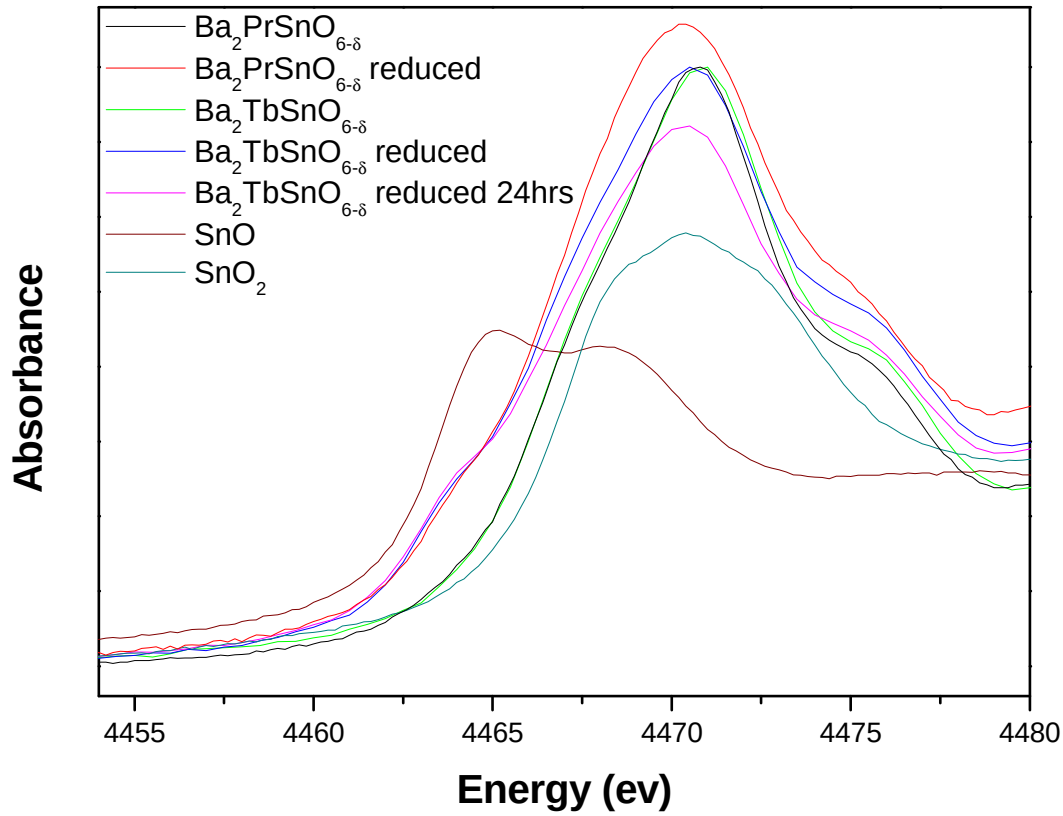

Figure 5.18: Sn L_I-edge of as synthesised and reduced samples of $Ba_2PrSnO_{6-\delta}$ and $Ba_2TbSnO_{6-\delta}$ and the Sn^{2+} and Sn^{4+} standards SnO and SnO_2. Of particular interest is the shoulder in the peak of the samples heated under reducing conditions at about 4464 eV indicating the presence of Sn^{2+}.

Examination of the Sb L_I-edge of compounds in the series $Ba_2PrSn_xSb_{1-x}O_{6-\delta}$ and the Sb containing samples studied in $Ba_2TbSn_xSb_{1-x}O_{6-\delta}$ (x = 0, 0.3 and 0.7) indicates that the shape and position of the edge is constant throughout these two series (see Figure 5.19). The energy of the white line in the samples was found to be at 4.705 keV. This

is slightly higher than the energy of the edge in the Sb^{5+} standard Sb_2O_5 and significantly higher than that of the Sb^{3+} standard Sb_2O_3. This can be interpreted as indicating that the Sb in these two series adopts the pentavalent oxidation state with no Sb^{3+} being present.

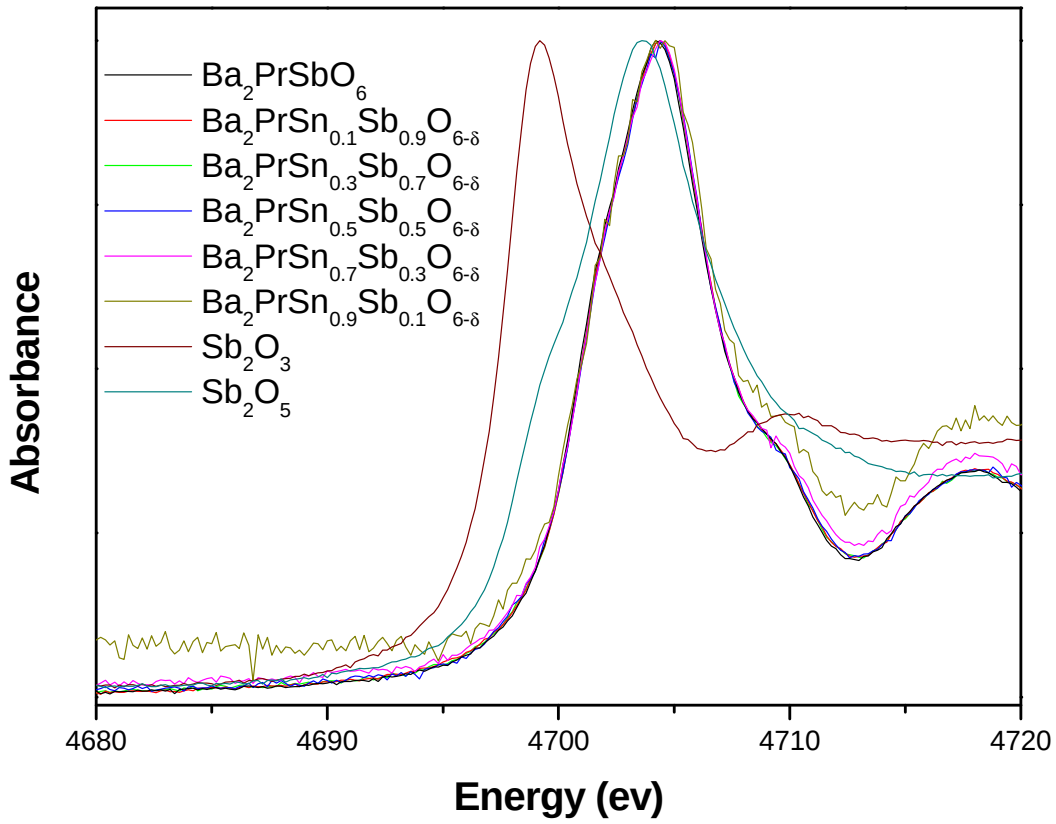

Figure 5.19: Sb L_I-edge for selected compounds in the series $Ba_2PrSn_xSb_{1-x}O_{6-\delta}$ and, the Sb^{3+} and Sb^{5+} standards, Sb_2O_3 and Sb_2O_5.

Having confirmed that Sn and Sb adopt the tetravalent and pentavalent oxidation states in the as synthesised samples of $Ba_2PrSn_xSb_{1-x}O_{6-\delta}$ and $Ba_2TbSn_xSb_{1-x}O_{6-\delta}$ attention was then turned to quantifying the way in which the oxidation state of Pr and Tb changes throughout the series. In order to achieve this the Pr and Tb L_{III}-edges were examined because of their higher sensitivity to the oxidation state of these lanthanides. This transition is between the 2*p* and the 5*d* states, the energy of which is particularly dependant on the 4*f* occupancy because of the decrease in effective nuclear charge that occurs with an increased number of 4*f* electrons[33, 34].

The energy and shape of the near-edge region of the Pr L_{III} spectrum of Ba_2PrSbO_6 is very similar to that of the $Pr_2Sn_2O_7$ edge (see Figure 5.20). There is, however, some difference in the shape of the edge and the post-edge regions of these two spectra. This can most likely be attributed to the difference in the co-ordination environment of Pr in these two samples. As there is no evidence for any features in the edge of Ba_2PrSbO_6 diagnostic of Pr^{4+} it can be concluded that only Pr^{3+} is present in this compound. The Pr L_{III}-edge in $Ba_2PrSnO_{6-\delta}$, on the other hand, is very similar to that measured for $BaPrO_3$, with the white line associated with this edge occurring at 5.972 keV (see Figure 5.20).

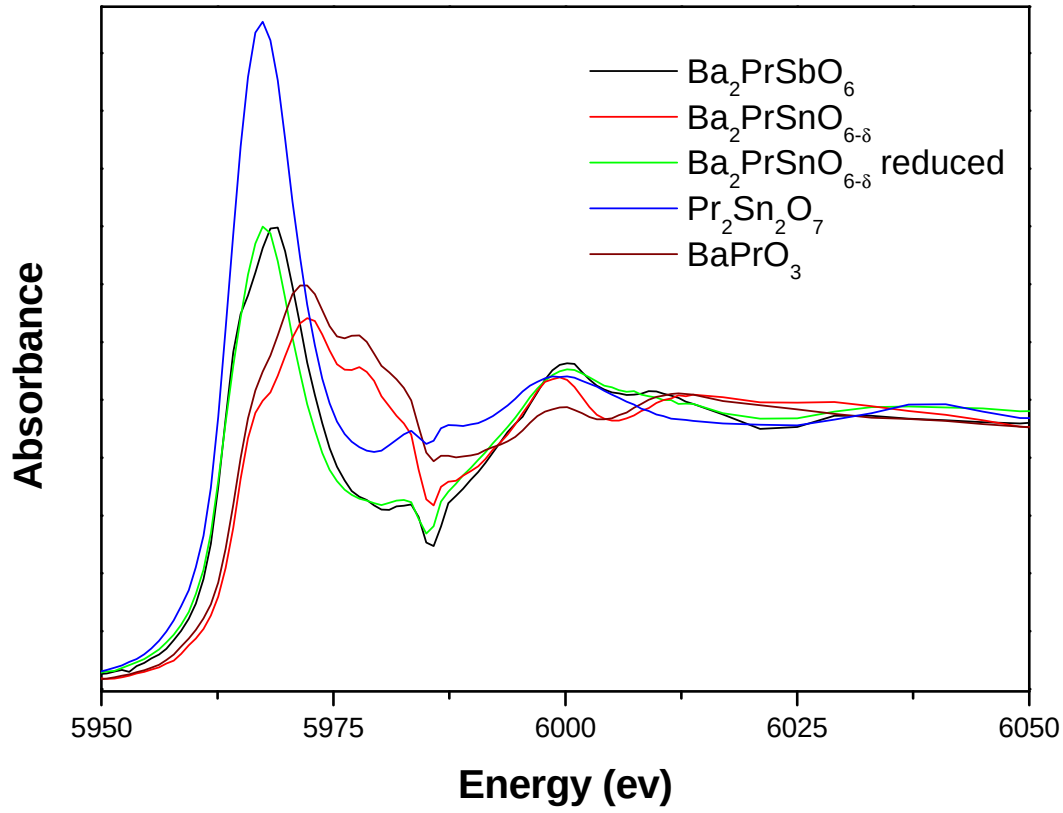

Figure 5.20: Pr L_{III}-edge spectra of Ba_2PrSbO_6 and an as synthesised and reduced sample of $Ba_2PrSnO_{6-\delta}$. The L_{III}-edges of $Pr_2Sn_2O_7$ and $BaPrO_3$ are plotted for comparison. The drop in absorbance near 5985 eV is caused by a glitch in the spectra.

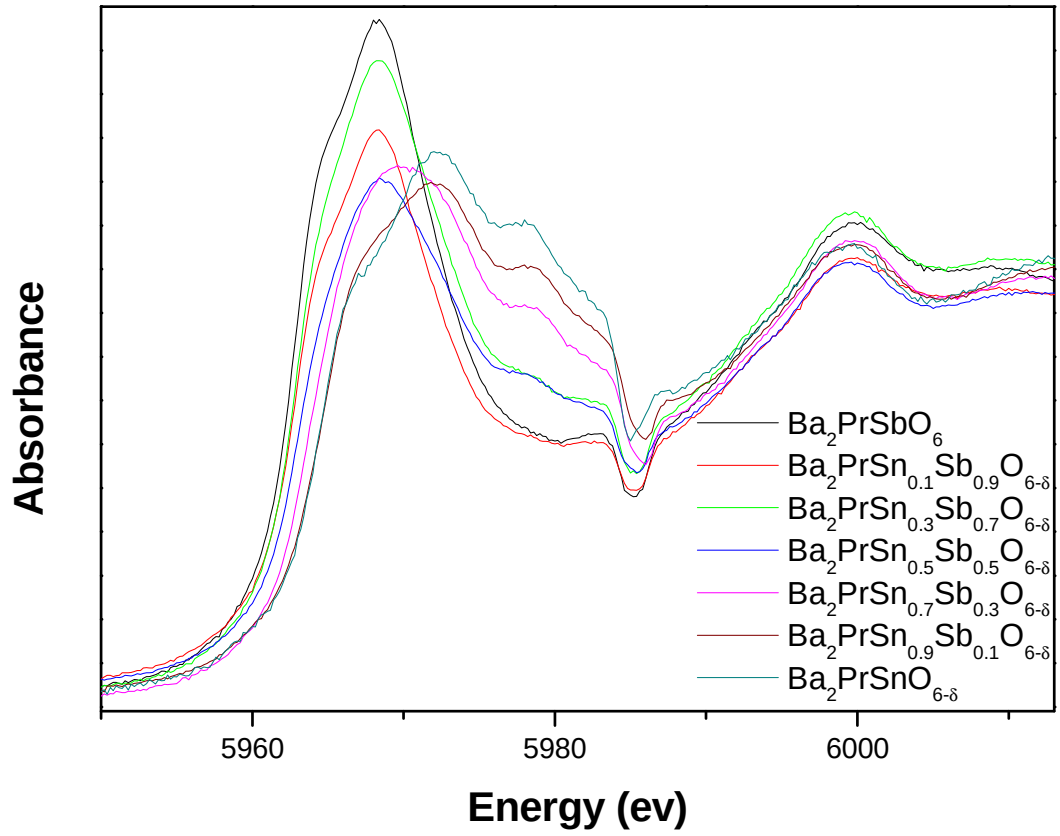

Figure 5.21: Pr L_{III}-edge spectra of selected compounds in the series $Ba_2PrSn_xSb_{1-x}O_{6-\delta}$ indicating the change in the energy and shape of the edge between 5960-5985 eV with increasing x.

Spectra of the L_{III}-edges of intermediate compounds in the series $Ba_2PrSn_xSb_{1-x}O_{6-\delta}$ show that as x increases the Pr^{3+}-like features of Ba_2PrSbO_6 gradually decrease in intensity while the Pr^{4+}-like features of $Ba_2PrSnO_{6-\delta}$ slowly increase (see Figure 5.21). Principal Component Analysis (PCA), which involves investigating a series of unknown related spectra to determine the common significant components they consist of, was carried out on the intermediate members of the $Ba_2PrSn_xSb_{1-x}O_{6-\delta}$ series. This was done over the energy range of 5.902-6.200 keV using the PCA program belonging to the EXAFSPAK suite[35]. This analysis revealed that there were only two significant components in the spectra of all the intermediate members of the series. Target transformation analysis carried out using TARGET[35], which tests whether the components found by PCA match those of sample spectra, demonstrated that these two components were well matched by the Ba_2PrSbO_6 and $Ba_2PrSnO_{6-\delta}$ end members. This indicates that the two components of the intermediate compounds in $Ba_2PrSn_xSb_{1-x}O_{6-\delta}$ are most likely the spectra of the end member

compounds of this series. The end members were better fits for the target transformation analysis than the $Pr_2Sn_2O_7$ and $BaPrO_3$ standards principally because the different co-ordination environment of Pr^{3+} in $Pr_2Sn_2O_7$ means that shape of the post-edge region of $Pr_2Sn_2O_7$ is significantly different from that of the Pr^{3+} in the perovskite series.

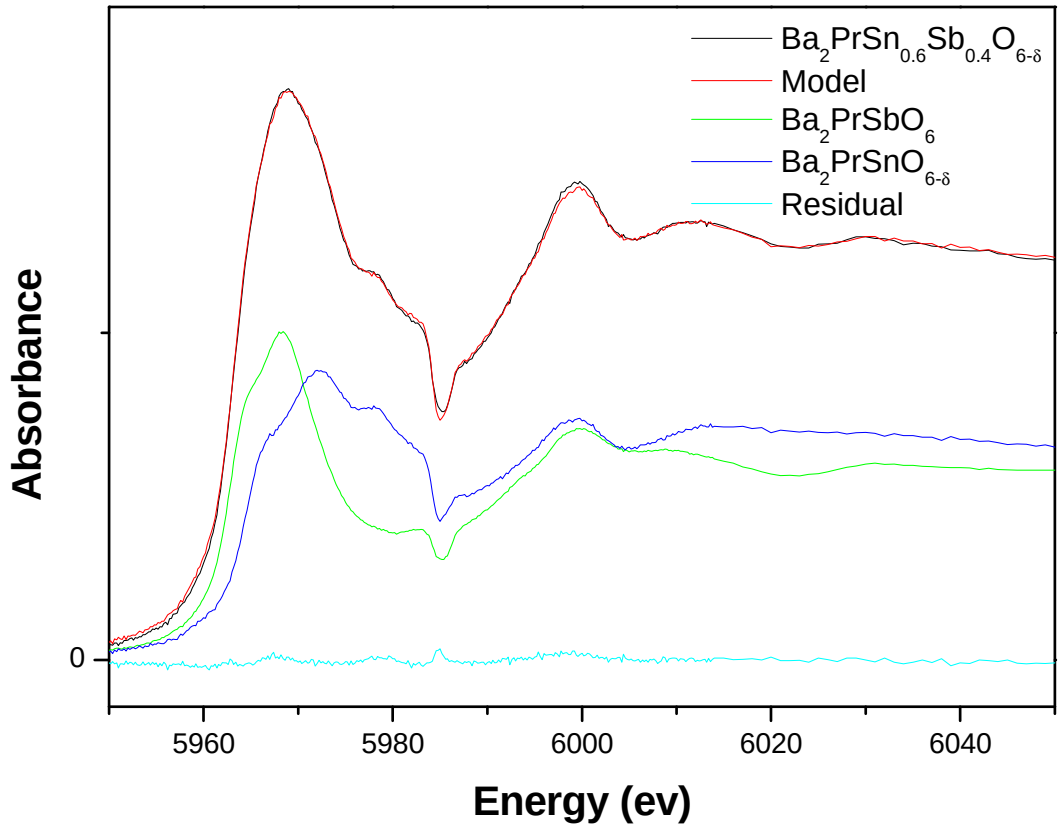

Figure 5.22: Plot of the L_{III}-edge of $Ba_2PrSn_{0.6}Sb_{0.4}O_{6-\delta}$ and the model spectrum fitted to it including the Ba_2PrSbO_6 and $Ba_2PrSnO_{6-\delta}$ components of the fit.

The structural analysis carried out using synchrotron X-ray and neutron diffraction, UV-Vis-NIR spectroscopy and the qualitative analysis of the Pr L_{III}-edge XANES all suggest that the Pr in Ba_2PrSbO_6 and $Ba_2PrSnO_{6-\delta}$ is purely trivalent and tetravalent respectively. Therefore these two compounds could be used as Pr^{3+} and Pr^{4+} standards and thereby accurately determine the oxidation state of Pr in the intermediate members of the $Ba_2PrSn_xSb_{1-x}O_{6-\delta}$ series. This was done by carrying out a multiple linear regression of the Pr L_{III}-edge spectra of the two end member compounds against the spectra for each of the individual intermediate compounds over the energy range of the 5.950-6.050 keV using the DATFIT program (see Figure 5.22 for an example

of the quality of the fits obtained)[35-37]. Such a quantitative analysis is possible using XANES spectra since, unlike the UV-Vis-NIR spectra, only the intensity of the Pr^{3+} and Pr^{4+} like-features change with increased Sn^{4+} doping with the energy of these features remaining constant. This analysis found that the ratio of Pr^{3+} to Pr^{4+} gradually changes across the series with the amount of Pr^{4+} increasing with increasing Sn^{4+} concentration (see Figure 5.23).

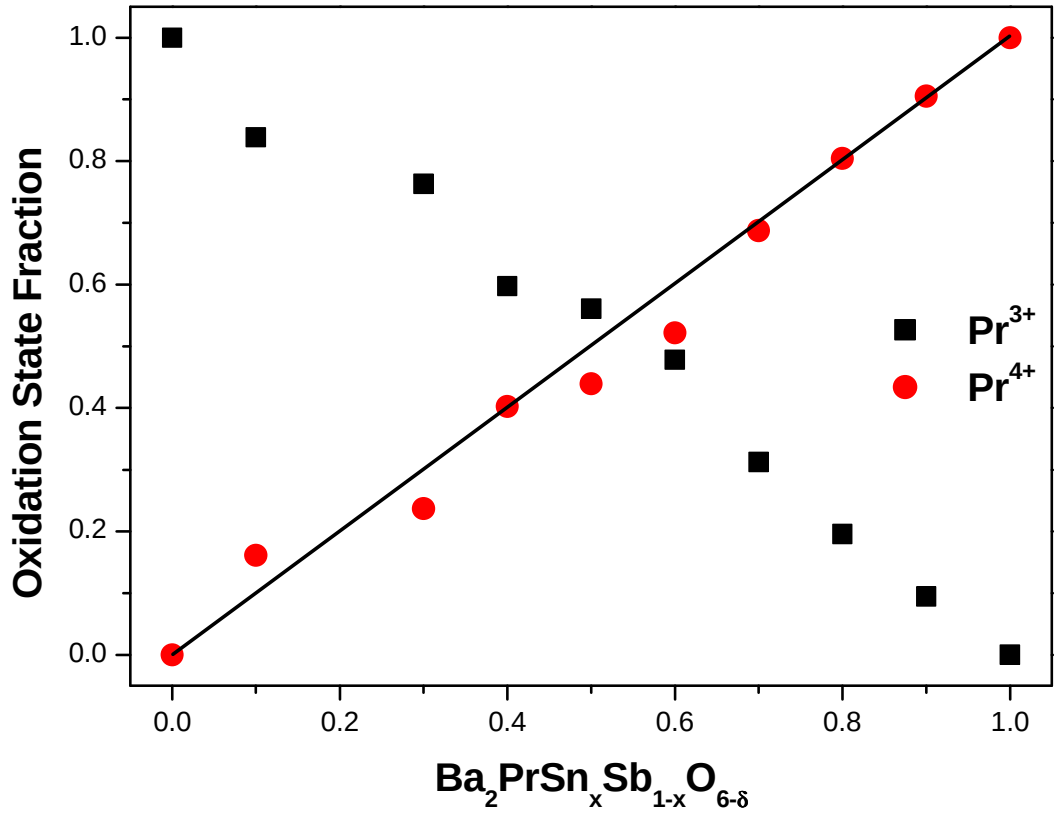

Figure 5.23: Plot of the oxidation state fraction of Pr^{3+} and Pr^{4+} in each compound examined in the $Ba_2PrSn_xSb_{1-x}O_{6-\delta}$ series. The black line indicates the amount of Pr^{4+} required at each composition for there to be no oxygen vacancies present and is drawn as a guide to the eye. The x = 0.2 sample was not investigated due to experimental constraints.

Having established that Sn and Sb cations adopt the tetravalent and pentavalent oxidation states and assuming Ba always adopts the divalent state in perovskite-type materials the amount of oxygen vacancies in each compound could then be determined from the amount of Pr^{3+} and Pr^{4+} found via the regression analysis. As can be seen in Table 5.11, there is not a significant amount of oxygen vacancies in any

member of the $Ba_2PrSn_xSb_{1-x}O_{6-\delta}$ series, with the oxidation state change of Pr^{3+} to Pr^{4+} fully compensating for the charge loss of Sn^{4+} substituting for Sb^{5+}. It should be noted that a similar least squares analysis of the reduced sample of $Ba_2PrSnO_{6-\delta}$ found that this sample contains only Pr^{3+}. Inspection of the edge of this reduced sample, however, reveals that the energy of this edge is slightly lower than that of Ba_2PrSbO_6 suggesting that the presence of oxygen vacancies or Sn^{4+} instead of Sb^{5+} in neighbouring octahedra has a small effect on the energy of the edge (see Figure 5.20).

Table 5.11: Oxygen stoichiometry as determined by the multiple linear regression of the Pr and Tb L_{III}-edges for perovskites in the series $Ba_2LnSn_xSb_{1-x}O_{6-\delta}$ (Ln = Pr or Tb).

$Ba_2LnSn_xSb_{1-x}O_{6-\delta}$	Oxygen Stoichiometry	
x	Pr	Tb
0	6.00(1)	6.00(1)
0.1	6.03(2)	5.95(1)
0.2	N/A	5.95(1)
0.3	5.97(1)	5.95(1)
0.4	6.00(2)	5.96(1)
0.5	5.97(2)	5.97(1)
0.6	5.96(1)	5.97(1)
0.7	5.99(1)	5.97(1)
0.8	6.00(1)	5.99(1)
0.9	6.00(1)	5.99(1)
1.0	6.00(1)	6.00(1)

The Tb L_{III}-edge of Ba_2TbSbO_6 shows that the white line occurs at approximately 7.512 keV very close to that of the Tb^{3+} standard, $Tb_2Sn_2O_7$. This strongly suggests that Tb in this compound is trivalent (see Figure 5.24). Similarly to $Pr_2Sn_2O_7$ and Ba_2PrSbO_6, the post-edge region of these two Tb edges is significantly different, an observation that can be attributed to the different environment of Tb in the pyrochlore and perovskite structure. Since there is no evidence for any feature in the L_{III}-edge of Ba_2TbSbO_6 at the energy of the Tb^{4+} standard, $BaTbO_3$, it can be concluded that all Tb in this compound is trivalent consistent with the other techniques used to probe the oxidation state of Tb. On the other hand the L_{III}-edge spectrum of $Ba_2TbSnO_{6-\delta}$ has both a similar shape and position to that of $BaTbO_3$ indicating that all Tb in this compound is tetravalent (see Figure 5.24). This is consistent with the majority of structural data and the UV-Vis-NIR spectra. Since Sn has also been established to be

tetravalent in this compound this implies that the analysis by neutron diffraction suggesting that about 15 % of Tb^{3+} is present in $Ba_2TbSnO_{6-\delta}$ is incorrect. As stated previously this error could arise from cross-correlation between the site occupancy and atomic displacement parameters and highlights the advantage of using multiple analytical methods.

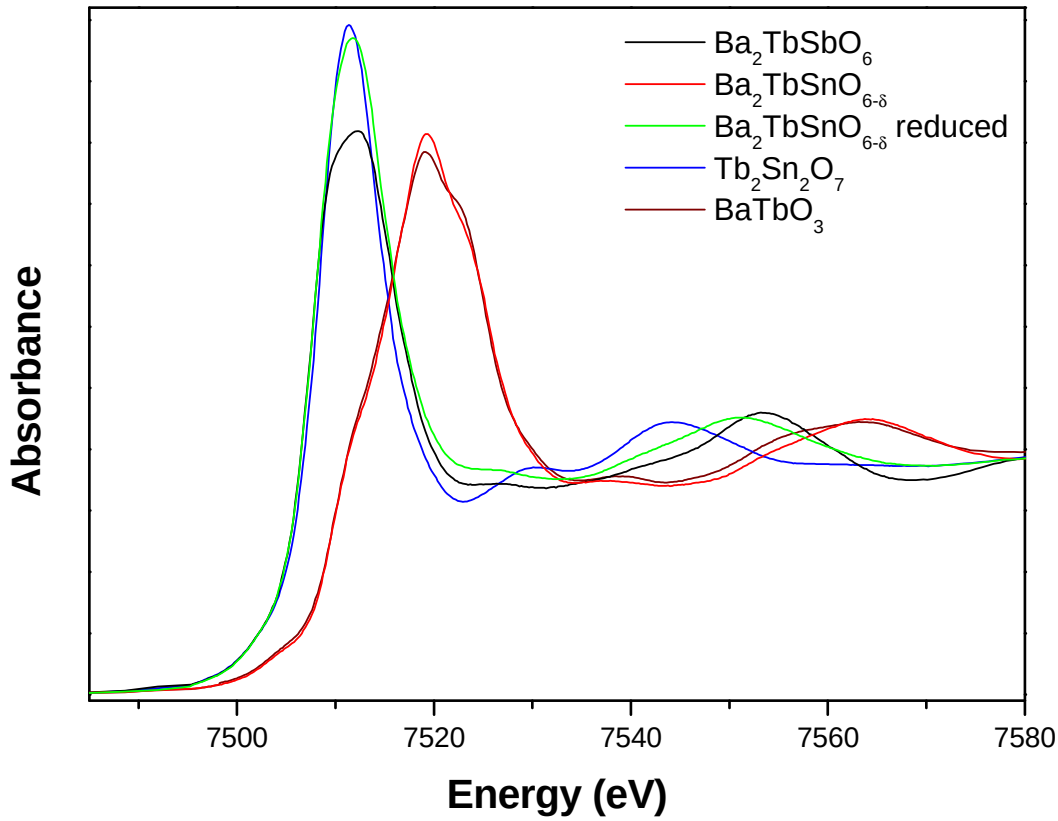

Figure 5.24: Tb L_{III}-edge spectra of Ba_2TbSbO_6 and an as synthesised and reduced sample of $Ba_2TbSnO_{6-\delta}$. The L_{III}-edges of $Tb_2Sn_2O_7$ and $BaTbO_3$ are plotted for comparison.

Qualitatively examination of the XANES region of the spectra of the intermediate compounds shows that as x increases the Tb^{3+} like features of Ba_2TbSbO_6 lose intensity while the Tb^{4+} like features in $Ba_2TbSnO_{6-\delta}$ gain intensity (see Figure 5.25). Having established that the Tb in Ba_2TbSbO_6 is all trivalent while $Ba_2TbSnO_{6-\delta}$ contains only Tb^{4+} the intermediate compounds in the series $Ba_2TbSn_xSb_{1-x}O_{6-\delta}$ can be analysed in a similar manner as was done for the analogous Pr series. PCA carried out over the energy range of 7.425-7.800 keV indicated that all the intermediate spectra consist of only two common components, which target transformation analysis

confirmed were good matches to the spectra of Ba_2TbSbO_6 and $Ba_2TbSnO_{6-\delta}$. Multiple linear regression analysis was then used to fit the region 7.475-7.675 keV to determine what fraction of Tb^{3+} and Tb^{4+} was present. Again, the end members of the series were selected to be used as Tb^{3+} and Tb^{4+} standards for this analysis because their oxidation state had been well established by a combination of several techniques. Furthermore the different co-ordination environment in the Tb^{3+} pyrochlore reduces the accuracy of the analysis if $Tb_2Sn_2O_7$ and $BaTbO_3$ were used.

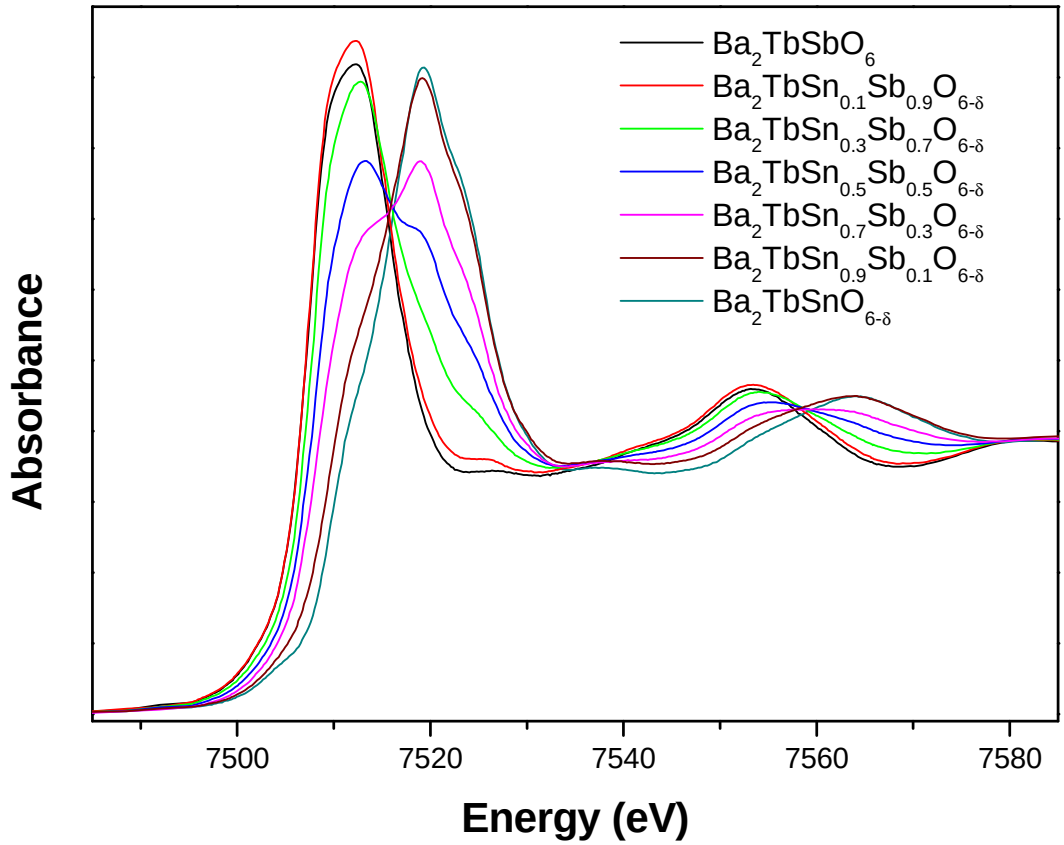

Figure 5.25: Tb L_{III}-edge spectra of selected compounds in the series $Ba_2TbSn_xSb_{1-x}O_{6-\delta}$ indicating the change in the energy and shape of the edge between 7485-7585 eV with increasing x.

The least squares analysis of the intermediate compounds reveals that the rate at which Tb^{3+} changes to Tb^{4+} as Sn^{4+} substitutes for Sb^{5+} is not sufficient in the samples with a small amount of Sn^{4+} to totally prevent the formation of oxygen vacancies. In the series $Ba_2TbSn_xSb_{1-x}O_{6-\delta}$ the x = 0.1-0.3 samples were found to have $\delta = 0.05$ (see Figure 5.26 and Table 5.11 for the oxidation state fraction of Tb and the amount of oxygen vacancy in each compound respectively). For x = 0.4 and greater, the amount

of oxygen vacancies present appears to decrease achieving a fully stoichiometric perovskite with respect to oxygen for $Ba_2TbSnO_{6-\delta}$. This contrasts with the results for $Ba_2PrSn_xSb_{1-x}O_{6-\delta}$, where there was no consistent evidence for oxygen vacancies. Although the number of oxygen vacancies found, by analysis of the XANES spectra, in intermediate compounds in the series $Ba_2TbSn_xSb_{1-x}O_{6-\delta}$ is small, and is not significantly larger than that suggested to be present in some samples in the Pr series, it is the apparent persistence of these oxygen vacancies in all intermediate samples that leads to the conclusion that they are present. The amount of variability of oxygen vacancies found in samples across the series $Ba_2PrSn_xSb_{1-x}O_{6-\delta}$ prevents a similar conclusion in that case. A similar regression analysis of the Tb L_{III}-edge spectrum of a reduced sample of $Ba_2TbSn_xSb_{1-x}O_{6-\delta}$ suggested that all the Tb^{4+} had been reduced to Tb^{3+} upon heating to 800 °C in 5 % H_2 in Ar (see Figure 5.24 for XANES spectra). This confirms that the anomalously large weight loss revealed by TGA, under reducing conditions, is caused by the partial reduction of Sn^{4+}.

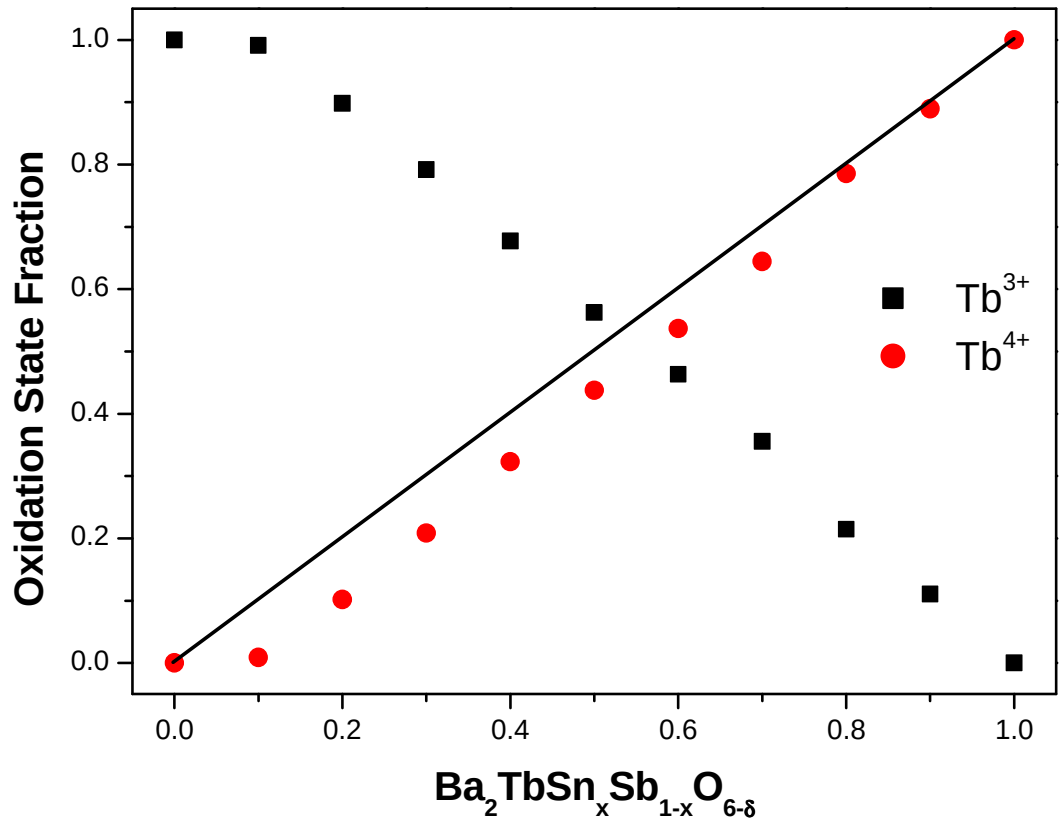

Figure 5.26: Plot of the oxidation state fraction of Tb^{3+} and Tb^{4+} in each compound examined in the $Ba_2TbSn_xSb_{1-x}O_{6-\delta}$ series. The black line is drawn as a guide to the amount of Tb^{4+} required for there to be no oxygen vacancies present.

5.4.2 Characterisation of $Ba_2LnSn_xNb_{1-x}O_{6-\delta}$

Characterisation of the compounds in the series $Ba_2LnSn_xNb_{1-x}O_{6-\delta}$ (Ln = Pr or Tb) will be presented in three sections. The first two will detail the structures of the Pr and Tb series respectively while the final section examines the oxidation states of the lanthanides in these two series using a combination of UV-Vis-NIR and XANES spectroscopies.

5.4.2.1 Structures of $Ba_2PrSn_xNb_{1-x}O_{6-\delta}$

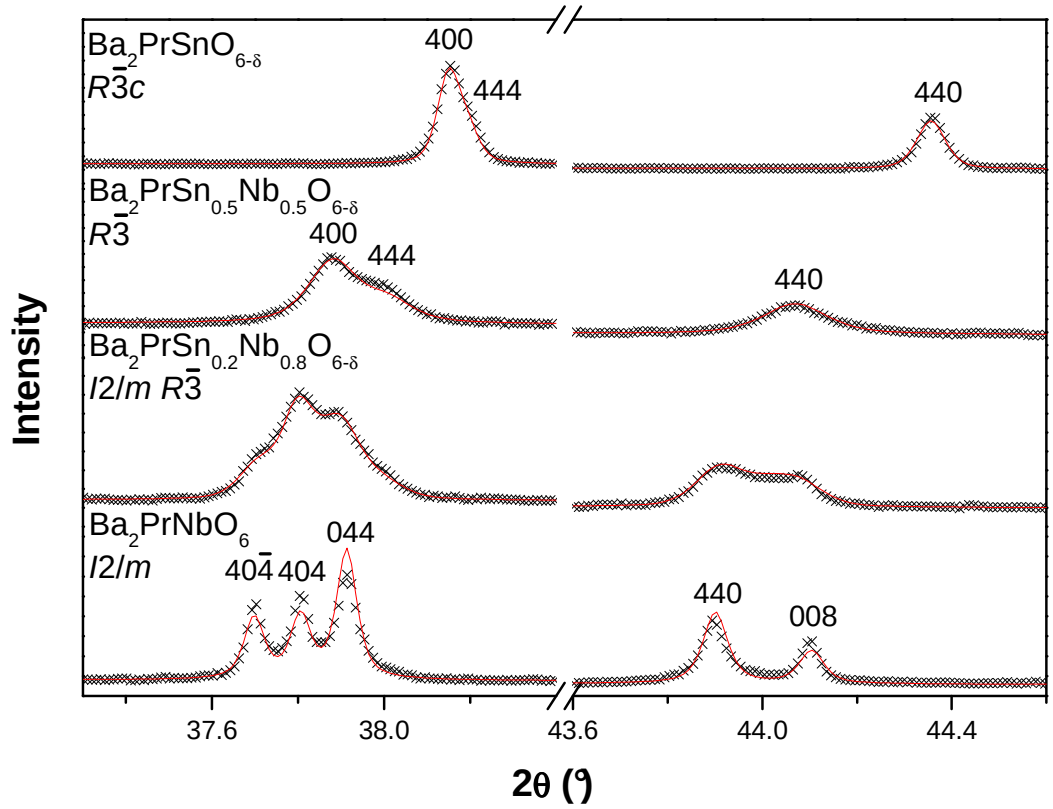

Figure 5.27: Selected regions of the diffraction patterns of compounds in the series $Ba_2PrSn_xNb_{1-x}O_{6-\delta}$ highlighting the different symmetry structures adopted. The format is the same as for Figure 5.2.

As established in Chapter 3 and Section 5.4.1.1 Ba_2PrNbO_6 and $Ba_2PrSnO_{6-\delta}$ adopt the fully B-site ordered $I2/m$ monoclinic and the disordered $R\bar{3}c$ rhombohedral structures respectively (see Figure 5.27). That $Ba_2PrSnO_{6-\delta}$ has a smaller unit cell than Ba_2PrNbO_6 (see Table 5.12), despite the larger ionic radii of Sn^{4+} compared to Nb^{5+} (cf. 0.69 to 0.64 Å[6]) suggests that the dominant oxidation state of Pr in Ba_2PrNbO_6 is

trivalent. This is consistent with the B-site cations being ordered in Ba_2PrNbO_6 but not in $Ba_2PrSnO_{6-\delta}$. Refinement against a neutron diffraction pattern of Ba_2PrNbO_6 yields an occupancy of the axial and equatorial oxygen sites of 99(2) and 102(1) % respectively consistent with a fully stoichiometric compound with respect to oxygen (see Figure 5.28 for the quality of the fit). Assuming that Nb in this compound is pentavalent, which is consistent with the use of Nb_2O_5 as a starting material and synthesis being under oxidising conditions, it is reasonable to conclude that Pr in Ba_2PrNbO_6 adopts the trivalent oxidation state.

Table 5.12: Unit cell parameters and volume for compounds in the series $Ba_2PrSn_xNb_{1-x}O_{6-\delta}$. In the x = 0.4 sample β was unstable and was therefore set to 90°.

x	Space Group	*a* (Å)	*b* (Å)	*c* (Å)	α (°)	β (°)	Volume (Å^3)
0	*I*2/*m*	6.09269(6)	6.05523(6)	8.55218(9)	90	90.1668(5)	315.511(6)
0.1	*I*2/*m*	6.09096(3)	6.05502(3)	8.55208(4)	90	90.1604(5)	315.407(3)
0.2	*I*2/*m*	6.08488(12)	6.05097(11)	8.54955(18)	90	90.1287(11)	314.788(10)
	$R\bar{3}$	6.04432(15)	= *a*	= *a*	60.2347(28)	= α	156.920(189)
0.3	*I*2/*m*	6.08032(19)	6.04861(15)	8.54293(29)	90	90.0914(43)	314.187(16)
	$R\bar{3}$	6.04579(10)	= *a*	= *a*	60.2178(15)	= α	157.038(99)
0.4	*I*2/*m*	6.08027(40)	6.04659(33)	8.54436(7)	90	90	314.130(40)
	$R\bar{3}$	6.04019(26)	= *a*	= *a*	60.2005(35)	= α	156.532(233)
0.5	$R\bar{3}$	6.03908(10)	= *a*	= *a*	60.1600(17)	= α	156.303(117)
0.6	$R\bar{3}$	6.03629(25)	= *a*	= *a*	60.0982(39)	= α	155.867(262)
0.7	$R\bar{3}$	6.03105(33)	= *a*	= *a*	60.0700(51)	= α	155.367(341)
0.8	$R\bar{3}c$	6.02087(19)	= *a*	= *a*	60.0523(31)	= α	154.516(210)
0.9	$R\bar{3}c$	6.01629(11)	= *a*	= *a*	60.0824(17)	= α	154.270(116)
1.0	$R\bar{3}c$	6.00990(6)	= *a*	= *a*	60.0551(9)	= α	153.683(58)

The synchrotron X-ray diffraction patterns of intermediate compounds in the series $Ba_2PrSn_xNb_{1-x}O_{6-\delta}$ revealed a series of phases. While the diffraction pattern of $Ba_2PrSn_{0.1}Nb_{0.9}O_{6-\delta}$ was well fitted by a model with *I*2/*m* symmetry (R_p and R_{wp} of 6.3 and 6.0 % respectively) attempts to fit more Sn^{4+} rich samples with such a model were unsuccessful. Diffraction patterns of samples with x = 0.2 to 0.4 revealed the presence of a two phase mixture (see Figure 5.27). The diffraction patterns of samples with x = 0.5-0.7 featured splitting consistent with rhombohedral symmetry (see Figure 5.27) and these also had the lowest angle *R*-point super-lattice peaks, the overlapping (111) and (100) Bragg reflections, at ~9.3° indicating B-site cation ordering. This shows

that compounds with x = 0.5-0.7 adopt $R\bar{3}$ rhombohedral symmetry and these three diffraction patterns were satisfactorily fitted using models with this structure. Diffraction patterns of compounds x = 0.8 and 0.9 still featured splitting consistent with rhombohedral symmetry but no longer had any indication of the lowest angle *R*-point reflections indicative of cation ordering. These compounds adopt the same symmetry as $Ba_2PrSnO_{6-\delta}$, $R\bar{3}c$ rhombohedral.

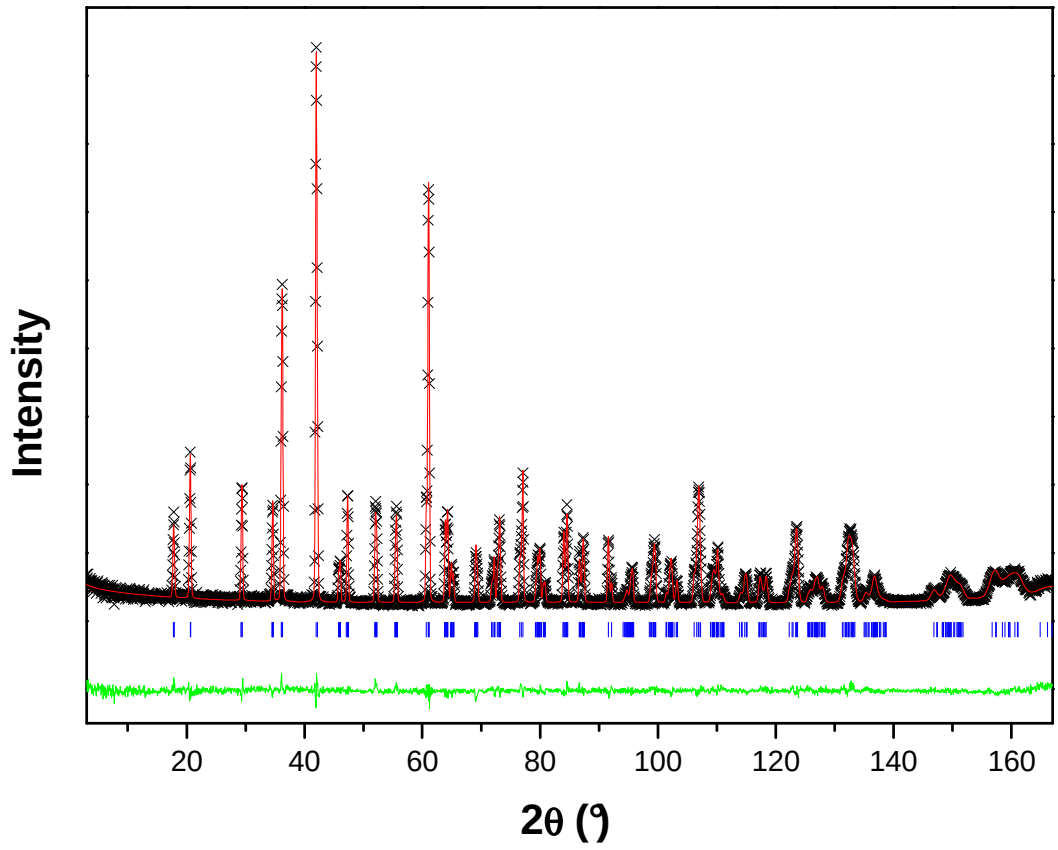

Figure 5.28: Neutron diffraction pattern of Ba_2PrNbO_6 collected using BT-1. The format is the same as for Figure 5.1.

Having established that the structures on either side of the two phase region were *I*2/*m* monoclinic and $R\bar{3}$ rhombohedral a combination of these two models was used to fit the x = 0.2-0.4 samples. Good fits were obtained to the diffraction patterns of these samples using this approach. The existence of the two phase region can be interpreted in two ways. The first possibility is that it is a result of the discontinuous phase transition that is required to occur between structures adopting these two space groups. On the other hand it could be interpreted as indicating that, similarly to the two phase region in the series $Ba_2PrSn_xSb_{1-x}O_{6-\delta}$, there is some type of cation

segregation occurring between these two phases. To confirm which of these possibilities was correct a sample of $Ba_2PrSn_{0.2}Nb_{0.8}O_{6-\delta}$ was examined between 150-300 °C using synchrotron X-ray diffraction. These diffraction patterns showed that at 150 °C the sample is single phase and adopts rhombohedral symmetry. This confirms that the two phase co-existence of monoclinic and rhombohedral symmetries in the x = 0.2-0.4 samples of $Ba_2PrSn_xNb_{1-x}O_{6-\delta}$ is caused by the discontinuous phase transition between these two symmetries, and not by cation segregation.

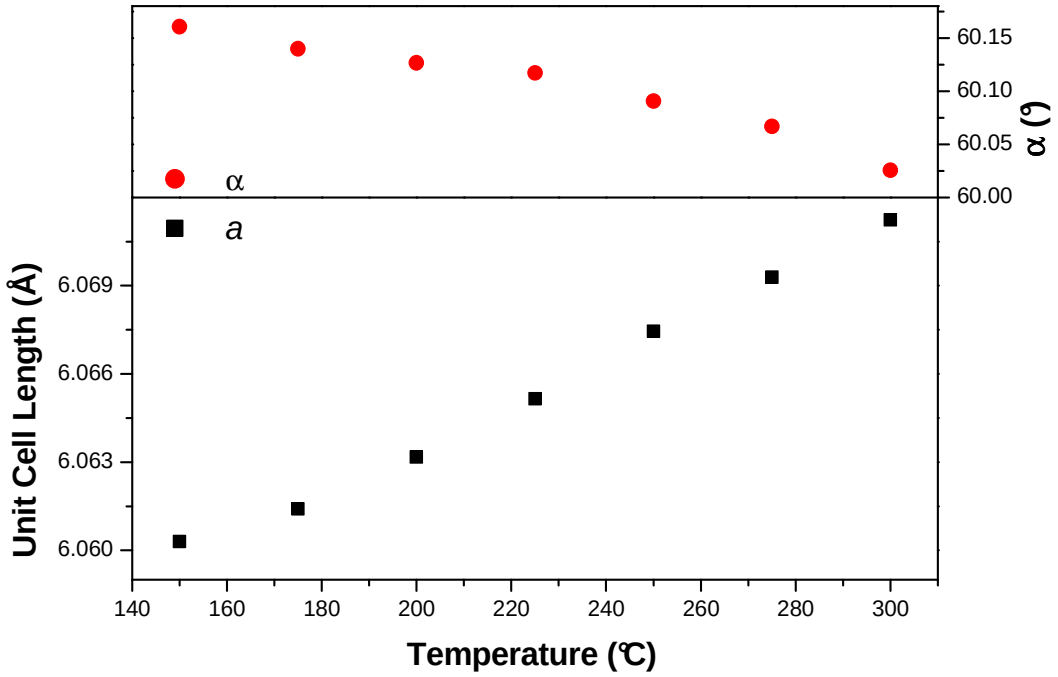

Figure 5.29: Unit cell parameters of $Ba_2PrSn_{0.2}Nb_{0.8}O_{6-\delta}$ versus temperature.

The decrease in the rhombohedral angle of $Ba_2PrSn_{0.2}Nb_{0.8}O_{6-\delta}$ with increasing temperature implies that the phase transition to $Fm\bar{3}m$ cubic symmetry would be expected to occur slightly above 300 °C (see Figure 5.29). The square of the rhombohedral distortion (α-60) versus temperature is linear (see Figure 5.30). Since the rhombohedral distortion is proportional to the square of the order parameter (Q^2) of the Landau free energy expansion the transition between the rhombohedral and cubic phases in this compound must be tricritical in nature[38]. An extrapolation of the square of the rhombohedral distortion to zero suggests that the phase transition should occur at approximately 302(4) °C, just slightly above the maximum temperature investigated. That the phase transition is tricritical is not surprising since such

transitions often occur between two structures when there is an additional nearby phase that is stable[39, 40]. As discussed in Chapter 3, in the Ba_2LnNbO_6 series of compounds there is competition between the *I*4/*m* tetragonal and $R\bar{3}$ rhombohedral structures to be the intermediate phase adopted between monoclinic and cubic symmetries. It is reasonable to conclude that similar competition occurs in $Ba_2PrSn_{0.2}Nb_{0.8}O_{6-\delta}$, causing the observed transition to be tricritical.

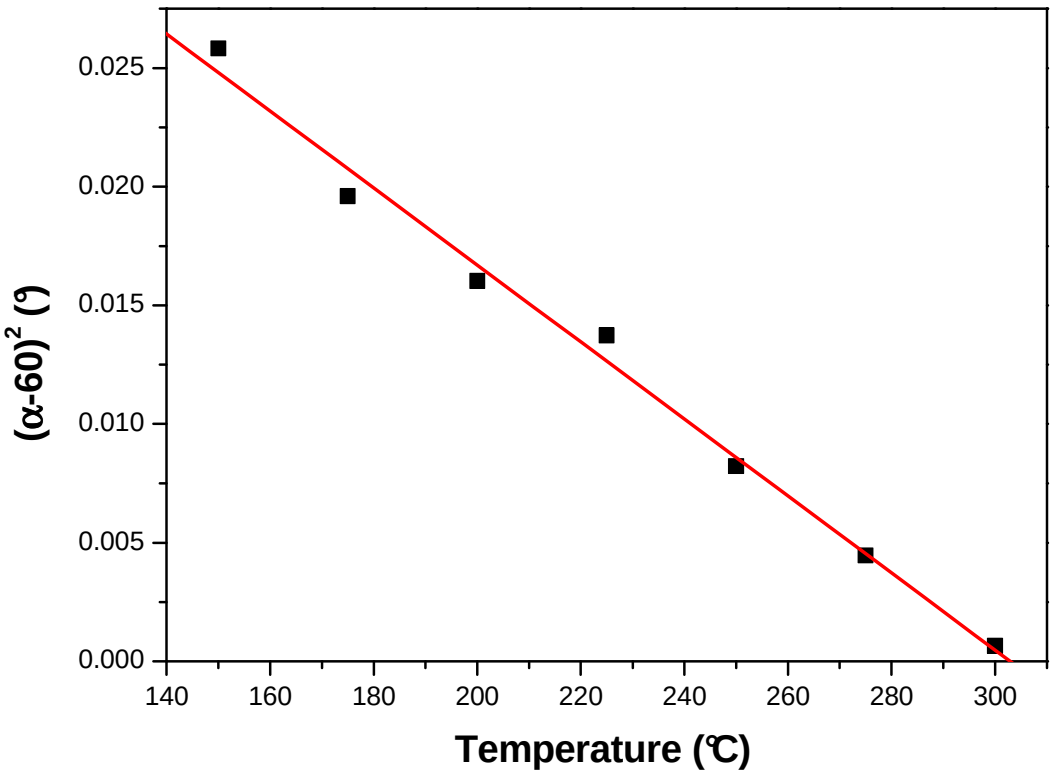

Figure 5.30: Plot of the square of rhombohedral strain versus temperature for $Ba_2PrSn_{0.2}Nb_{0.8}O_{6-\delta}$. The linear fit to the plot confirms that the transition is tricritical.

Refinements against synchrotron X-ray diffraction patterns indicate that the $Ba_2PrSn_xNb_{1-x}O_{6-\delta}$ compounds with x = 0-0.5 have a high degree of B-site cation ordering with a minimum of approximately 90 % Pr on the 2*a* or 1*a* site, in the monoclinic or rhombohedral structure respectively, with the other 10 % being made up of Sn^{4+} and Nb^{5+} in a ratio fixed to the stoichiometry of the compound (the B' site is fixed to have the opposite Pr and B' ratio such as to maintain the nominal stoichiometry). Unfortunately, due to unusually high noise in the diffraction patterns of x = 0.6-0.7 samples it was not possible to reliably refine the degree of cation ordering for these using X-ray diffraction. This high background was caused by air

scattering due to instrumental failure and occurred despite two attempts to collect each pattern. Neutron diffraction is, however, in the case of this combination of B-site cations relatively sensitive to the degree of B-site cation (the coherent neutron scattering lengths of Nb, Sn and Pr are 7.14(3), 6.225(2) and 4.58(5) fm respectively[15]). Refinement of neutron diffraction patterns of the x = 0.6 and 0.7 samples suggest that these samples also have a high degree of B-site cation ordering.

In contrast with the high degree of B-site cation ordering exhibited by the x = 0-0.7 samples, $Ba_2PrSn_{0.8}Nb_{0.2}O_{6-\delta}$ adopts $R\bar{3}c$ symmetry and therefore has no B-site cation ordering. This sudden loss of order between the x = 0.7 and 0.8 samples is very different from that found for the $Ba_2TbSn_xSb_{1-x}O_{6-\delta}$ series where the loss of cation ordering occurs gradually with increased Sn^{4+} doping. The Pr-O and Sn/Nb-O bond lengths in the compounds in the series $Ba_2PrSn_xNb_{1-x}O_{6-\delta}$ increase and decrease, respectively, in a gradual fashion with increasing x (see Table 5.13 and 5.14 for crystallographic positions and cation bond distances respectively). This occurs such that the Pr-O and Sn/Nb-O bond lengths have a small difference in length, ~ 0.06 Å, in the x = 0.7 sample before order is lost and a disordered structure adopted for x = 0.8.

The evolution of Pr-O bond length is consistent with the gradual change in oxidation state from Pr^{3+} to Pr^{4+} across the series with the difference in Pr-O bond lengths between the Ba_2PrNbO_6 and $Ba_2PrSnO_{6-\delta}$ end members being 0.20 Å. This change in Pr-O bond length is larger than the difference in the ionic radii of Pr^{3+} and Pr^{4+} (0.14 Å[6]) and this additional shortening of the Pr-O bond may be related to the Pr and Sn^{4+} cations sharing the same site in $Ba_2PrSnO_{6-\delta}$. Similarly to the $Ba_2PrSn_xSb_{1-x}O_{6-\delta}$ compounds the Pr cation are overbonded throughout the series. This is in contrast to the significant underbonding of Sn^{4+} and Nb^{5+} particularly in the x = 0.8-1.0 samples where Pr, Sn^{4+} and Nb^{5+} all occupy the same crystallographic site. This suggests that there may some local distortions around each of these different cations in the disordered structures to satisfy their different bonding requirements. Lattice parameters and unit cell volumes for compounds in the series $Ba_2PrSn_xNb_{1-x}O_{6-\delta}$ are illustrated in Figure 5.31 and tabulated in Table 5.12.

Table 5.13: Crystallographic information for the series $Ba_2PrSn_xNb_{1-x}O_{6-\delta}$. Structures have been determined using either neutron or, in the case of the x = 0.8 sample, synchrotron X-ray diffraction. In the case of the x = 0.6 and 0.7 samples refinement of the 1*a* site gives a Pr occupancy of 0.99(4) and 1.02(5) respectively with the remainder of the site consisting of B' cations.

Compound	Ba_2PrNbO_6	$Ba_2PrSn_{0.6}Nb_{0.4}O_{6-\delta}$	$Ba_2PrSn_{0.7}Nb_{0.3}O_{6-\delta}$	$Ba_2PrSn_{0.8}Nb_{0.2}O_{6-\delta}$
Space Group	*I*2/*m*	$R\bar{3}$	$R\bar{3}$	$R\bar{3}c$
a (Å)	6.0940(1)	6.0336(3)	6.0278(3)	6.0209(2)
b (Å)	6.0546(2)	= *a*	= *a*	= *a*
c (Å)	8.5521(2)	= *a*	= *a*	= *a*
α (°)	90	60.127(4)	60.110(5)	60.052(3)
β (°)	90.178(2)	= α	= α	= α
γ(°)	90	= α	= α	= α
Ba	4*i* (x,0,z)	2*c* (x,x,x)	2*c* (x,x,x)	2*a* (¼,¼,¼)
x	0.5023(5)	0.2503(11)	¼	¼
z	0.2476(5)	= x	= x	¼
B (Å^2)	0.81(2)	0.86(2)	0.86(2)	1.06(4)
Pr	2*a* (0,0,0)	1*a* (0,0,0)	1*a* (0,0,0)	2*b* (0,0,0)
B (Å^2)	0.72(5)	0.43(2)	0.50(2)	0.51(4)
B'	2*d* (0,0,½)	1*b* (½,½,½)	1*b* (½,½,½)	2*b* (0,0,0)
B (Å^2)	0.21(4)	0.45(2)	0.48(2)	= Pr *B*
O1	4*i* (x,0,z)	6*f* (x,y,z)	6*f* (x,y,z)	6*e* (x,½-x,¼)
x	0.0537(4)	0.7385(11)	0.7433(16)	0.7858(10)
y	0	0.2247(5)	0.2240(5)	0.7142(10)
z	0.2698(3)	0.2876(5)	0.2827(7)	¼
B (Å^2)	1.01(7)	1.82(2)	1.81(2)	0.88(9)
Occupancy	0.988(16)	0.998(4)	0.995(5)	1
O2	8*j* (x,y,z)			
x	0.2702(3)			
y	0.2669(4)			
z	0.9718(2)			
B (Å^2)	1.51(5)			
Occupancy	1.015(10)			
R_p %	5.3	5.4	5.7	4.6
R_{wp} %	6.4	6.7	7.0	4.1
χ^2	1.0	1.6	1.9	46

Table 5.14: Bond lengths and bond valence sums (BVS) for selected compounds in the $Ba_2PrSn_xNb_{1-x}O_{6-\delta}$ series. Structures have been determined using either neutron or, in the case of the x = 0.8 sample, synchrotron X-ray diffraction. The BVS for Pr is based on the Pr^{3+}-O parameter since the appropriate value for Pr^{4+} is not known. In the case of the mixed Sn^{4+} and Nb^{5+} structures the BVS for Sn^{4+} is listed above Nb^{5+}.

x	Ba-O			Pr-O		B'-O	
	Bond Length (Å)		BVS	Bond Length (Å)	BVS	Bond Length (Å)	BVS
0	1 × 2.741(4) 2 × 2.840(3) 2 × 2.884(4) 2 × 3.0500(5)	2 × 3.187(4) 2 × 3.246(4) 1 × 3.365(4)	1.79	2 × 2.329(2) 4 × 2.320(2)	3.61	2 × 1.997(2) 4 × 2.003(2)	4.70
0.6	3 × 2.833(1) 3 × 2.987(10)	3 × 3.059(10) 3 × 3.213(1)	1.77	6 × 2.196(4)	5.09	6 × 2.092(4)	3.62 3.67
0.7	3 × 2.842(1) 3 × 2.999(11)	3 × 3.039(11) 3 × 3.196(1)	1.77	6 × 2.169(5)	5.47	6 × 2.112(5)	3.43 3.49
0.8	3 × 2.7974(1) 6 × 3.018(6) 3 × 3.2283(1)		1.84	6 × 2.140(8)	5.91	= Pr-O	3.18 3.23

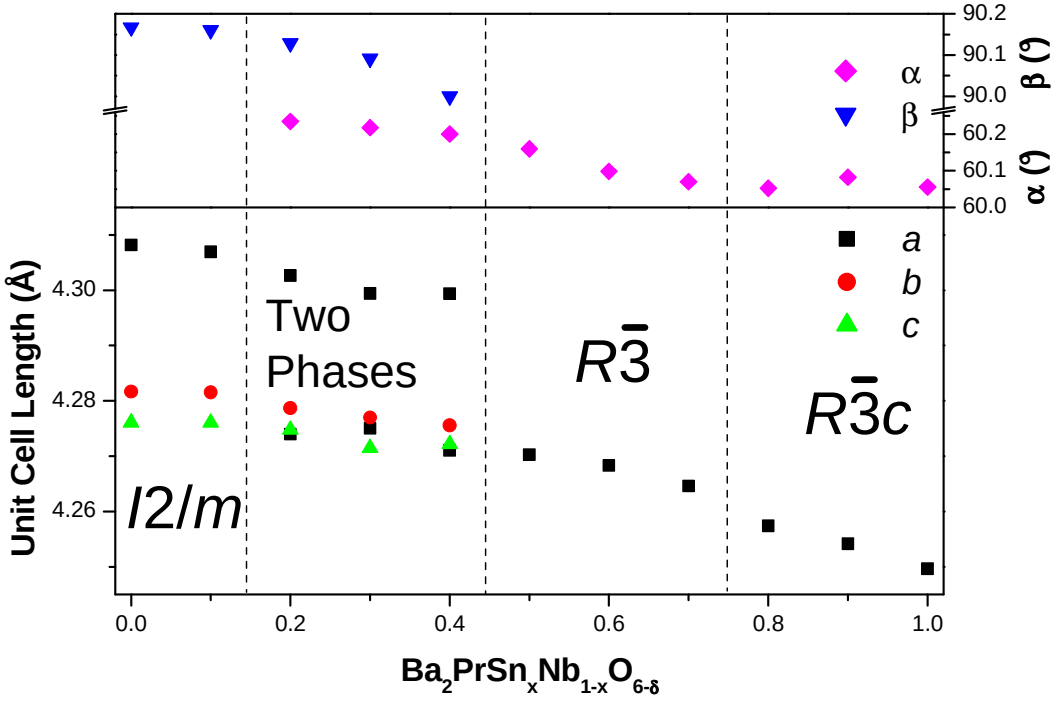

Figure 5.31: Reduced unit cell parameters for compounds in the series $Ba_2PrSn_xNb_{1-x}O_{6-\delta}$.

5.4.2.2 Structures of $Ba_2TbSn_xNb_{1-x}O_{6-\delta}$

Table 5.15: Unit cell parameters, atomic positions, displacement and oxygen occupancy parameters as determined using neutron diffraction for compounds in the series $Ba_2TbSn_xNb_{1-x}O_{6-\delta}$. In the partially ordered x = 0.3 and 0.6 structures the occupancy of the 2*a* site refines to 74(15) % in the case of x = 0.3 and the 4*a* site is set as 67 % for x = 0.6 based on the refinement of the synchrotron X-ray diffraction pattern of this sample.

Compound	Ba_2TbNbO_6	$Ba_2TbSn_{0.3}Nb_{0.7}O_{6-\delta}$	$Ba_2TbSn_{0.6}Nb_{0.4}O_{6-\delta}$	$Ba_2TbSn_{0.7}Sb_{0.3}O_{6-\delta}$
Space Group	*I*4/*m*	*I*4/*m*	$Fm\bar{3}m$	$Pm\bar{3}m$
a (Å)	5.9816(1)	5.9796(3)	8.4364(2)	4.21390(8)
c (Å)	8.4757(2)	8.4588(10)	= *a*	= *a*
Ba	4*d* (0,½,¼)	4*d* (0,½,¼)	8*c* (¼,¼,¼)	1*b* (½,½,½)
B (Å^2)	0.94(3)	0.69(2)	0.67(2)	0.71(2)
Tb	2*a* (0,0,0)	2*a* (0,0,0)	4*a* (0,0,0)	1*a* (0,0,0)
B (Å^2)	0.61(5)	0.23(6)	0.37(2)	0.40(2)
B'	2*b* (0,0,½)	2*b* (0,0,½)	4*b* (½,½,½)	1*a* (0,0,0)
B (Å^2)	0.49(5)	0.44(6)	0.37(2)	= Tb *B*
O1	4*e* (0,0,z)	4*e* (0,0,z)	24*e* (x,0,0)	3*d* (½,0,0)
x	0	0	0.2539(2)	½
z	0.2665(5)	0.2674(26)	0	0
B (Å^2)	1.33(14)	1.02*	1.34(1)	1.25(1)
Occupancy	1.024(36)	1	0.984(4)	0.978(4)
O2	8*h* (x,y,0)	8*h* (x,y,0)		
x	0.2441(4)	0.2626(37)		
y	0.2821(4)	0.2470(9)		
z	0	0		
B (Å^2)	1.44(8)	1.12*		
Occupancy	1.002(18)	0.986(6)		
R_p %	5.5	5.2	5.6	5.5
R_{wp} %	6.5	6.6	6.9	7.2
χ^2	2.5	1.8	2.1	2.2

* Oxygen displacement parameters refined anisotropically : O1 B_{11} = B_{22} = 0.0142(27) and B_{33} = -0.0001(7); O2 B_{11} = 0.0077(35), B_{22} = 0.0099(33), B_{33} = 0.0067(15) and B_{12} = -0.0001(21).

As established, in Chapter 3, using synchrotron X-ray diffraction Ba_2TbNbO_6, adopts an *I*4/*m* tetragonal structure with full B-site cation ordering and this has a larger unit cell than $Ba_2TbSnO_{6-\delta}$. Refinement of a model against a neutron diffraction pattern gives an occupancy of the oxygen anion equatorial and axial sites of 102(4) and 100(2) % of full occupancy respectively, indicating that Tb adopts the trivalent

oxidation state in this compound (see Table 5.15 for crystallographic details). Apparently the loss of B-site cation ordering between Ba_2TbNbO_6 and $Ba_2TbSnO_{6-\delta}$ is a consequence of the oxidation of Tb^{3+} to Tb^{4+}. The degree of tetragonal splitting in Ba_2TbNbO_6 is quite small and a synchrotron X-ray diffraction pattern collected at 100 °C no longer contains any peak splitting suggesting that $Fm\bar{3}m$ cubic symmetry is adopted.

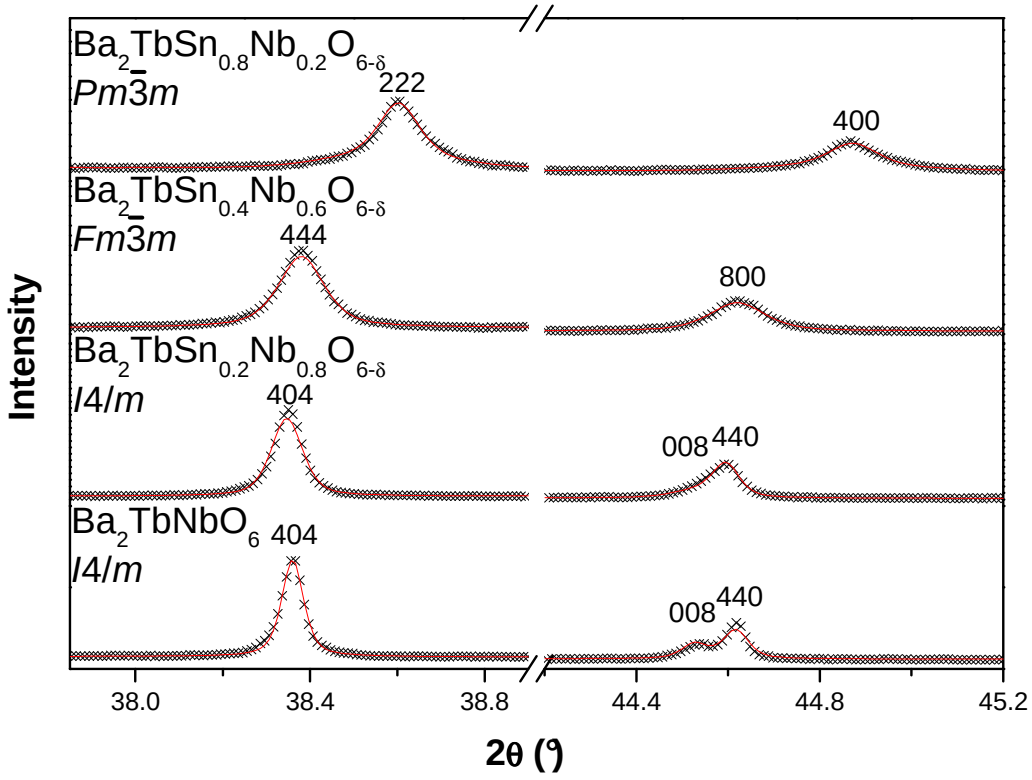

Figure 5.32: Selected regions of diffraction patterns of compounds in the series $Ba_2TbSn_xNb_{1-x}O_{6-\delta}$. The format is the same as for Figure 5.2.

The synchrotron X-ray diffraction patterns of compounds in the series $Ba_2TbSn_xNb_{1-x}O_{6-\delta}$ with x = 0.1-0.3 feature splitting consistent with *I*4/*m* symmetry. Subsequent refinements of models with this symmetry provide good fits to the data (see Figure 5.32). The x = 0.4-0.9 members of the series do not exhibit any peak splitting indicating that they adopt cubic symmetry (see Figure 5.32). The x = 0.4-0.6 compounds, however, feature weak *R*-point super-lattice reflections. Since these have cubic symmetry and lack any octahedral tilting, the *R*-point reflections arise from ordering of the B-site cations. Therefore these compounds adopt $Fm\bar{3}m$ cubic symmetry. The more Sn^{4+} rich compounds (x = 0.7-0.9) do not show any *R*-point

reflections confirming that they adopt the $Pm\bar{3}m$ structure also displayed by $Ba_2TbSnO_{6-\delta}$.

The synchrotron X-ray diffraction patterns of the x = 0.7-0.9 compounds feature peak asymmetry similar to that observed in $Ba_2TbSn_xSb_{1-x}O_{6-\delta}$; consequently a second *P*4/*mmm* "phase" was also used to improve the quality of the fit to diffraction patterns of these members of the niobate series. The peak shape parameters of this secondary phase are very broad confirming that the peak asymmetry is caused by strain in this compound, and not by the presence of a genuine second phase. Lattice parameters and unit cell volumes for compounds in the series $Ba_2TbSn_xNb_{1-x}O_{6-\delta}$ are plotted in Figure 5.33 and tabulated in Table 5.16.

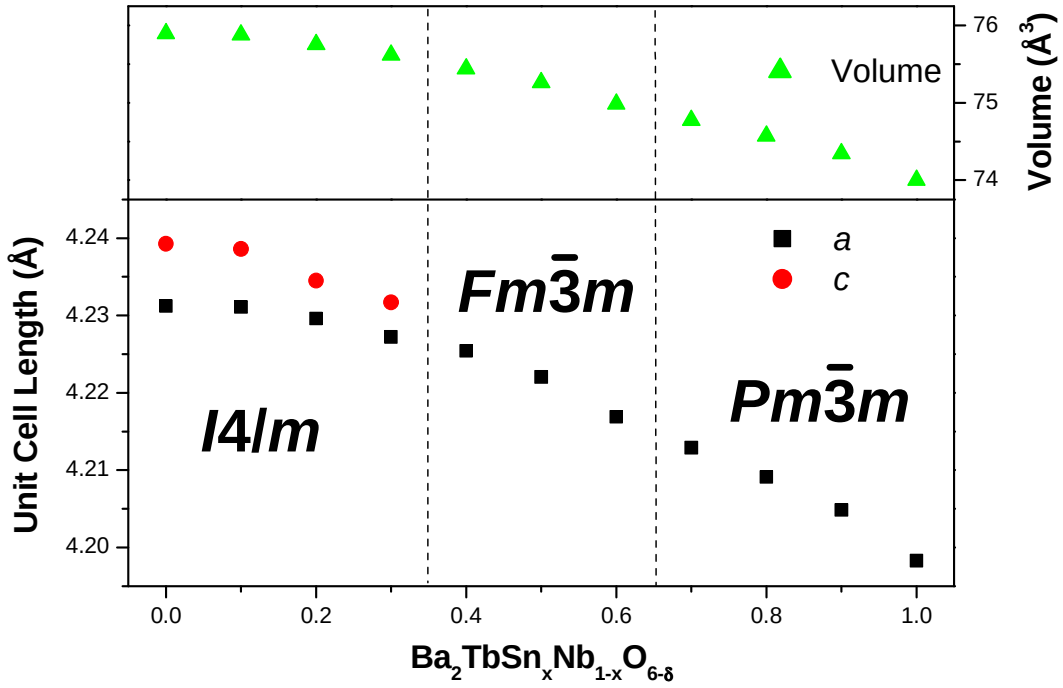

Figure 5.33: Reduced unit cell lengths and volumes for compounds in the series $Ba_2TbSn_xNb_{1-x}O_{6-\delta}$.

Table 5.16: Unit cell lengths and volumes for compounds in the series $Ba_2TbSn_xNb_{1-x}O_{6-\delta}$.

x	Space Group	*a* (Å)	*c* (Å)	Volume (Å^3)
0	*I*4/*m*	5.98382(5)	8.47854(6)	303.584(3)
0.1	*I*4/*m*	5.98364(4)	8.47719(6)	303.516(3)
0.2	*I*4/*m*	5.98154(4)	8.46900(9)	303.011(5)
0.3	*I*4/*m*	5.97820(6)	8.46339(12)	302.472(6)
0.4	$Fm\bar{3}m$	8.45083(8)	= *a*	603.530(10)
0.5	$Fm\bar{3}m$	8.44407(8)	= *a*	602.082(10)
0.6	$Fm\bar{3}m$	8.43374(11)	= *a*	599.875(14)
0.7	$Pm\bar{3}m$	4.21290(2)	= *a*	74.7726(7)
0.8	$Pm\bar{3}m$	4.20912(3)	= *a*	74.5716(8)
0.9	$Pm\bar{3}m$	4.20484(3)	= *a*	74.3447(10)
1.0	$Pm\bar{3}m$	4.19830(1)	= *a*	73.9980(8)

Table 5.17: Bond lengths and bond valence sums (BVS) for selected compounds in the $Ba_2TbSn_xNb_{1-x}O_{6-\delta}$ series determined using neutron diffraction. The BVS for Tb is based on the Tb^{3+}-O parameter since the appropriate value for Tb^{4+} is unknown. In the case of the mixed B' compounds the BVS for Sn^{4+} is listed above Nb^{5+}.

x	Ba-O		Tb-O		B'-O	
	Bond Length (Å)	BVS	Bond Length (Å)	BVS	Bond Length (Å)	BVS
0	4 × 2.884(1) 4 × 2.9941(2) 4 × 3.111(2)	1.84	2 × 2.259(4) 4 × 2.231(3)	3.57	2 × 1.979(4) 4 × 2.011(3)	4.73
0.3	4 × 2.944(9) 4 × 2.993(1) 4 × 3.038(9)	1.81	2 × 2.262(22) 4 × 2.156(20)	4.12	2 × 1.967(22) 4 × 2.075(19)	4.22 4.29
0.6	12 × 2.9829(1)	1.84	6 × 2.142(2)	4.67	6 × 2.076(2)	3.78 3.84
0.7	12 × 2.9797(1)	1.86	6 × 2.1070(1)	5.13	= Tb-O	3.48 3.53

Refinement of the structures in the $Ba_2TbSn_xNb_{1-x}O_{6-\delta}$ series against synchrotron X-ray diffraction patterns shows that the B-site cation ordering is lost gradually from full ordering in Ba_2TbNbO_6 to only 67.1(1) % of the 4*a* site being occupied by Tb in x = 0.6. It should be noted that refinements of the partially ordered structures were done in a similar manner as for the analogous Pr series in order to maintain nominal stoichiometry. This result is similar to the analogous antimonate series but contrasts with the $Ba_2PrSn_xNb_{1-x}O_{6-\delta}$ series, which loses cation ordering suddenly between the

x = 0.7 and 0.8 compounds. Consistent with the gradual loss of B-site cation ordering the Tb-O and Sn/Nb-O bonds gradually contract and expand respectively with increasing x. There is only a small difference, ~ 0.03 Å, between the B-site cation bonds in the disordered structure of the x = 0.7 member of the series and the Tb-O and Sn/Nb-O bonds of the last B-site ordered compound x = 0.6 (see Table 5.15 and 5.17 for refined structures and selected cation distances respectively). Similar to the other series examined in this chapter the Tb cations are significantly overbonded and the Sn^{4+} and Nb^{5+} cations are significantly underbonded in the structures where these cations occupy the same site.

Interestingly refinements using a neutron diffraction pattern of the tetragonal $Ba_2TbSn_{0.3}Nb_{0.7}O_{6-\delta}$ sample consistently suggest an unusually large difference between the axial and equatorial Tb-O bond lengths with an axial and equatorial bond length of 2.26(2) and 2.16(2) Å respectively. This stretching of the axial Tb-O bond is reversed in the Sn/Nb octahedra where the axial bond is significantly shorter than the equatorial bond (cf. 1.97(2) Å to 2.07(2) Å). The cause of these unusually distorted octahedra is not clear although it may be related to anisotropic peak broadening observed for (00*l*) Bragg reflections in the synchrotron X-ray diffraction pattern in both the x = 0.2 and 0.3 samples. The larger than expected standard deviations of the oxygen atomic positions, and therefore of the bond lengths in this structure, are caused by cross-correlation between the oxygen atomic positions and the anisotropic displacement parameters used in this model. While the precision in the atomic positions can be greatly increased by using isotropic displacement parameters this also results in noticeably less stable refinements with significantly higher R-values (cf. an R_p and R_{wp} of 5.2 and 6.6 % for a fit to the pattern using anisotropic displacement parameters to an R_p and R_{wp} of 5.7 and 7.3 % for a fit using isotropic displacement parameters).

5.4.2.3 Analysis of Oxygen Vacancies and Oxidation States of Cations in $Ba_2LnSn_xNb_{1-x}O_{6-\delta}$

The structures of compounds in the series $Ba_2LnSn_xNb_{1-x}O_{6-\delta}$ (Ln = Pr or Tb) determined in the previous two sections implies that, similarly to the analogous antimonate series, as x increases the trivalent lanthanide cations undergo a transition

to the tetravalent state. In order to determine the precise way in which this oxidation state change occurs and, therefore, if there is any significant level of oxygen vacancies in these compounds UV-Vis-NIR and XANES spectroscopies were used to probe the oxidation state of the lanthanide cations in each compound.

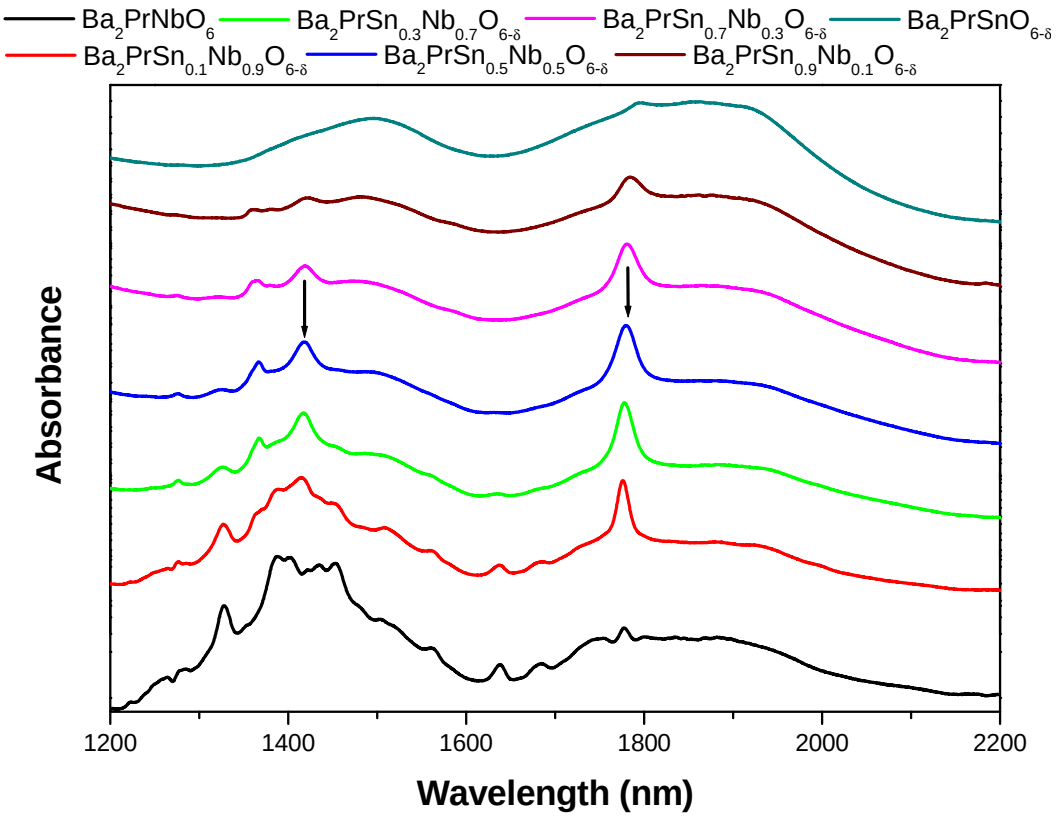

Figure 5.34: Selected spectra of compounds in the series $Ba_2PrSn_xNb_{1-x}O_{6-\delta}$ in the region 1200-2200 nm. The peaks marked by arrows in the spectrum of $Ba_2PrSn_{0.5}Nb_{0.5}O_{6-\delta}$ at approximately 1415 and 1775 nm are at their most intense in the intermediate compounds.

The 1200-2200 nm region of the Near-Infrared spectra of $Ba_2PrSn_xNb_{1-x}O_{6-\delta}$ exhibits sharp features associated with Pr^{3+} in Ba_2PrNbO_6, that lose intensity with increasing x while the broader features associated with Pr^{4+} in $Ba_2PrSnO_{6-\delta}$ become more intense (see Figure 5.34). This is similar to the trend observed in $Ba_2PrSn_xSb_{1-x}O_{6-\delta}$. There are, however, numerous weak features, most notably at 1415 and 1775 nm, in Ba_2PrNbO_6 that increase significantly in intensity towards the midpoint of the series before losing most, or all, of their intensity in $Ba_2PrSnO_{6-\delta}$. The cause of the behaviour of these features is uncertain. These additional bands are not observed in

the analogous antimonate series, which may suggest that they occur in the niobate compounds because they contain both Pr^{3+} and Pr^{4+} in the same structure. This in turn suggests that these bands may be related to charge transfer between Pr^{3+} and Pr^{4+} cations. The behaviour of the 250-700 nm UV-Vis region of the $Ba_2PrSn_xNb_{1-x}O_{6-\delta}$ spectra is similar to that in $Ba_2PrSn_xSb_{1-x}O_{6-\delta}$ with the main peak observed in this region increasing in intensity and broadening to lower energy with increasing x.

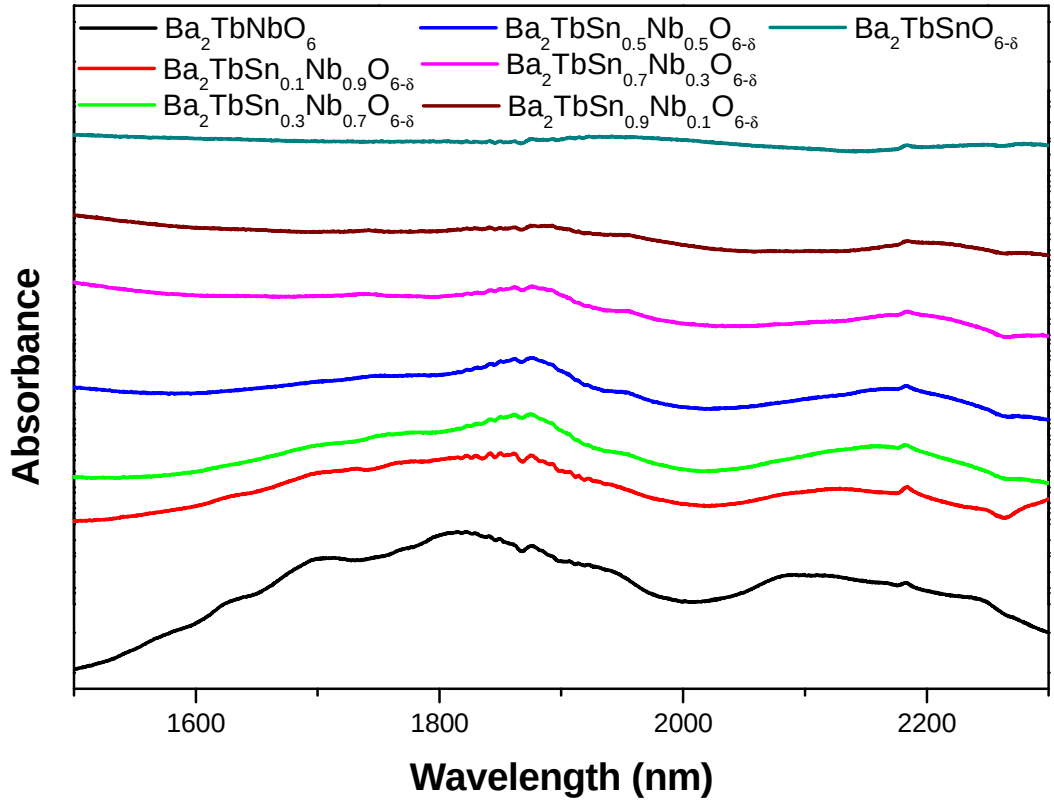

Figure 5.35: Selected spectra of compounds in the series $Ba_2TbSn_xNb_{1-x}O_{6-\delta}$ in the region 1500-2300 nm.

The 1500-2300 nm region of the spectra of $Ba_2TbSn_xNb_{1-x}O_{6-\delta}$ exhibit a slightly different change than that found for the analogous antimonate series (see Figure 5.35). The features found in Ba_2TbNbO_6, while not as strong or sharp as those found in Ba_2TbSbO_6, suggest the presence of Tb^{3+}. These features gradually decrease in intensity with increasing x leading to a featureless spectrum for $Ba_2TbSnO_{6-\delta}$. This indicates that there is a continuous oxidation state change from Tb^{3+} to Tb^{4+} with increased Sn^{4+} doping although why the change in spectra is more gradual than that found for $Ba_2TbSn_xSb_{1-x}O_{6-\delta}$ is unclear. The behaviour of the main feature in this

series in the region of 250-600 nm is similar to that found for the other three series examined, the broadening of this peak to 500 nm being consistent with a transition from Tb^{3+} to Tb^{4+}.

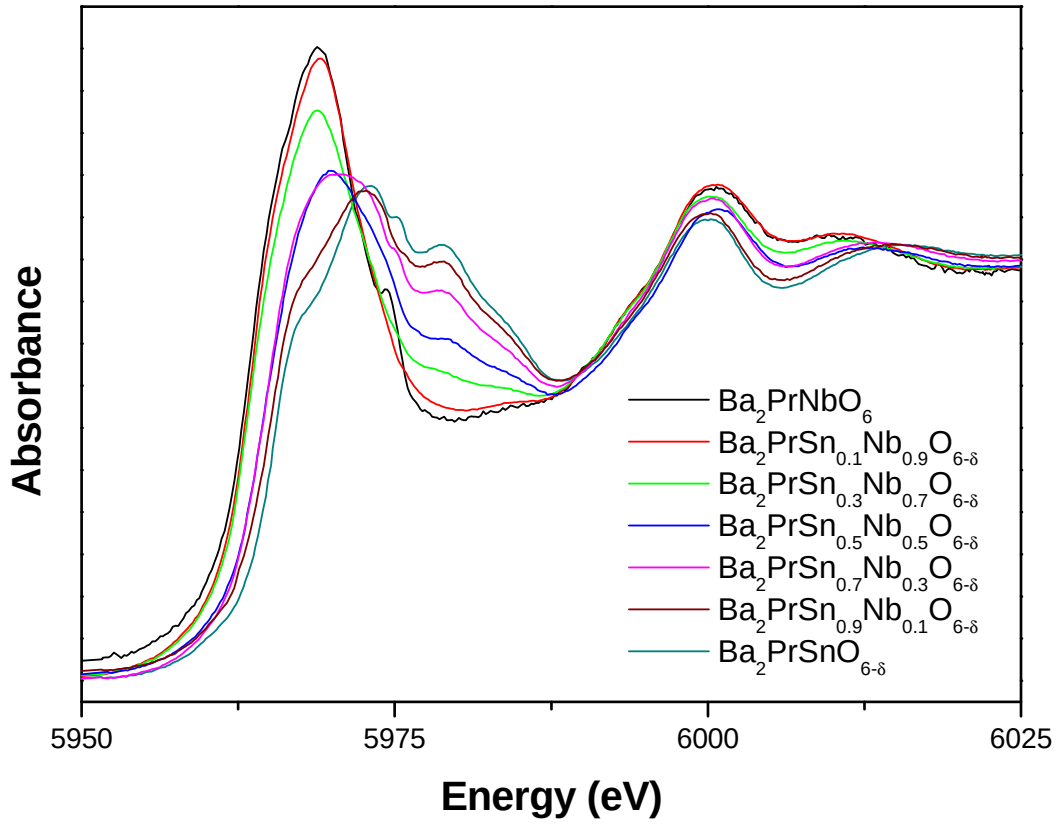

Figure 5.36: Pr L_{III}-edge spectra of selected compounds in the series $Ba_2PrSn_xNb_{1-x}O_{6-\delta}$ indicating the change in the energy and shape of the edge between 5960-5985 eV with increased Sn^{4+} doping.

Having used UV-Vis-NIR spectroscopy to confirm that Pr^{3+} and Tb^{3+} cations undergo a valency change to Pr^{4+} and Tb^{4+} in the series $Ba_2LnSn_xNb_{1-x}O_{6-\delta}$ XANES of the Pr and Tb L_{III}-edges were collected in-order to quantify the oxidation states of the cations in each compound. The white line of the Pr L_{III}-edge in Ba_2PrNbO_6 occurs at 5.969 keV, which is only 1 eV higher in energy than that of $Pr_2Sn_2O_7$, confirming that Pr is trivalent in this compound. These Pr^{3+} like features decrease in intensity with increased Sn^{4+} doping while features similar to those found in $Ba_2PrSnO_{6-\delta}$ increase in intensity (see Figure 5.36). Since it has already been established that the spectrum of $Ba_2PrSnO_{6-\delta}$ is consistent with this containing only Pr^{4+} this change

demonstrates the oxidation state change from Pr^{3+} to Pr^{4+} occurs gradually with increasing x.

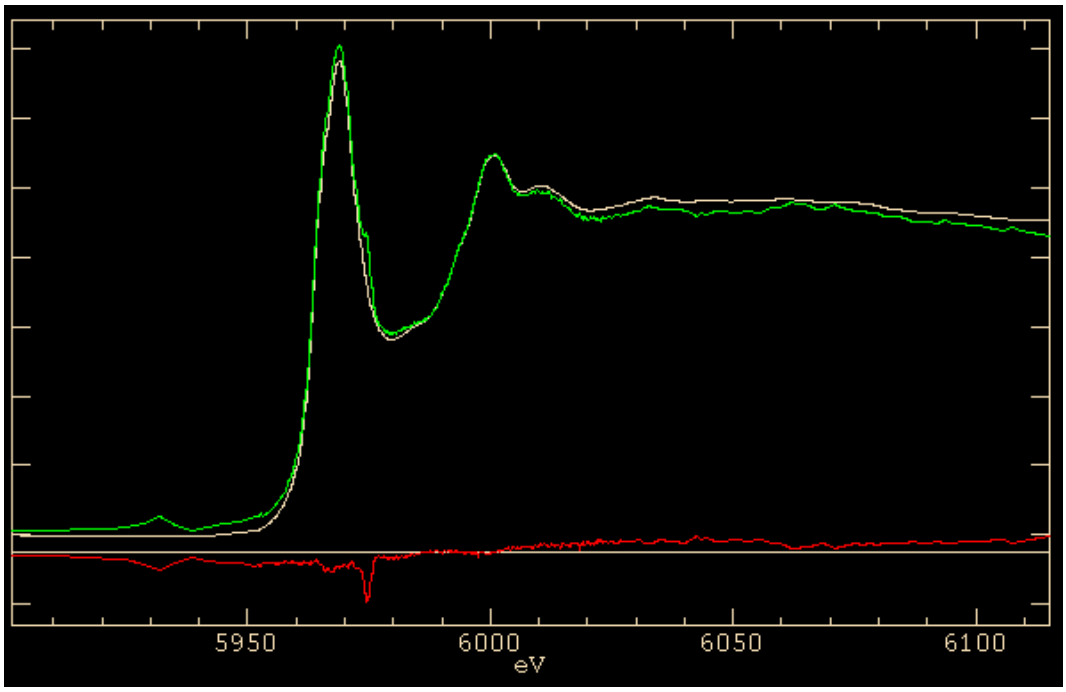

Figure 5.37: Target transformation fit of the Ba_2PrNbO_6 spectrum to the appropriate component of the PCA analysis. The green, white and red lines are the Ba_2PrNbO_6 and the PCA component spectra and the difference between the two respectively. Note the extra feature at approximately 5975 eV in the Ba_2PrNbO_6 spectra that is not in the component spectra.

Principal component analysis (PCA), carried out over the region 5.902-6.200 keV, indicates that the intermediate compounds in the series $Ba_2PrSn_xNb_{1-x}O_{6-\delta}$ consist of two common components. Target transformation analysis suggests that while one of these is an excellent match to the spectrum of $Ba_2PrSnO_{6-\delta}$ the other is not quite as well fitted by Ba_2PrNbO_6 (see Figure 5.37). This is principally because of a peak in the spectra of Ba_2PrNbO_6 that is at approximately 5.975 keV. This feature is not in the spectra of any of the intermediate compounds in the series nor does it match the energy of any Pr^{4+} features in either $Ba_2PrSnO_{6-\delta}$ or $BaPrO_3$. It is believed that is caused by either an instrumental "glitch"[41, 42] or from the presence of a very small amount of an impurity phase, possibly Pr_3NbO_7, identified in the sample by X-ray diffraction. As detailed in Chapter 3, Rietveld refinement suggests that this phase makes up approximately 1 mole % of the compound and it seems unlikely that such a

small impurity could contribute such a significant feature to the spectra. Regardless of the cause of this extra feature, the L_{III}-edge spectrum of Ba_2PrNbO_6 was a significantly better fit to the second component than the $Pr_2Sn_2O_7$ spectrum. Therefore this was selected to be used as component of the least squares fit of the spectra of the intermediate samples.

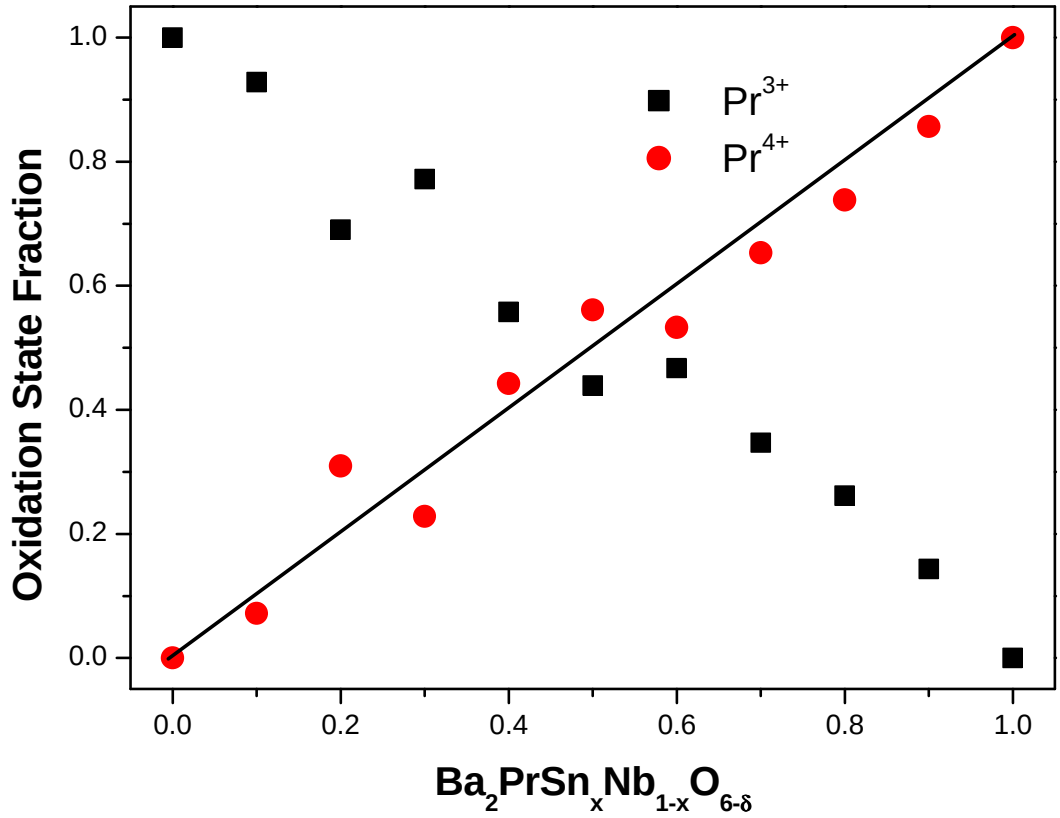

Figure 5.38: Plot of the oxidation state fraction of Pr^{3+} and Pr^{4+} in each compound examined in the $Ba_2PrSn_xNb_{1-x}O_{6-\delta}$ series. The black line depicts the amount of Pr^{4+} required at each composition for there to be no oxygen vacancies present and is drawn as a guide to the eye.

The least squares fit of the spectra of intermediate compounds in the series, carried out over the range 5.950-6.050 keV, showed that Pr^{3+} oxidises gradually to Pr^{4+} with increased Sn^{4+} doping. There is no evidence for a significant level of oxygen vacancies in these compounds (see Figure 5.38 and Table 5.18 for oxidation state fractions and oxygen stoichiometry respectively). It should be noted, however, that the fraction of Pr in each oxidation state changes significantly between samples with similar x. This is similar to, but more significant than, the variation found in the

analogous antimonate series. This extra variability is most likely related to the additional feature in the Ba_2PrNbO_6 spectrum causing complications in the fitting process and decreases the accuracy of the results obtained. This is consistent with a significant increase in the standard deviation of the relative abundances determined by the least squares refinement.

Table 5.18: Oxygen stoichiometry as determined by the least squared fit of the Pr and Tb L_{III}-edges for perovskites in the series $Ba_2LnSn_xNb_{1-x}O_{6-\delta}$ (Ln = Pr or Tb).

$Ba_2LnSn_xSb_{1-x}O_{6-\delta}$	Oxygen Stoichiometry	
x	Pr	Tb
0	6.00(1)	6.00(1)
0.1	5.99(1)	5.98(1)
0.2	6.05(3)	5.98(1)
0.3	5.96(1)	5.99(1)
0.4	6.02(2)	5.98(1)
0.5	6.03(1)	5.98(1)
0.6	5.97(1)	5.97(1)
0.7	5.98(1)	5.98(1)
0.8	5.97(1)	5.97(1)
0.9	5.98(1)	5.97(1)
1.0	6.00(1)	6.00(1)

The edge in the Tb L_{III}-edge spectrum of Ba_2TbNbO_6 occurs at a very similar energy to that of the Tb^{3+} standard, $Tb_2Sn_2O_7$. The edge does not have any features in the range of the Tb^{4+} standard showing that only Tb^{3+} is present in this sample. This is consistent with observations from UV-Vis-NIR spectroscopy and the structural models derived from Rietveld refinement. Since it was established in Section 5.4.1.4 that only Tb^{4+} is present in $Ba_2TbSnO_{6-\delta}$ this illustrates the full oxidation state change from Tb^{3+} to Tb^{4+} occurs with increasing Sn^{4+} doping in the series $Ba_2TbSn_xNb_{1-x}O_{6-\delta}$. The spectra of the intermediate compounds signify that this change occurs gradually (see Figure 5.39).

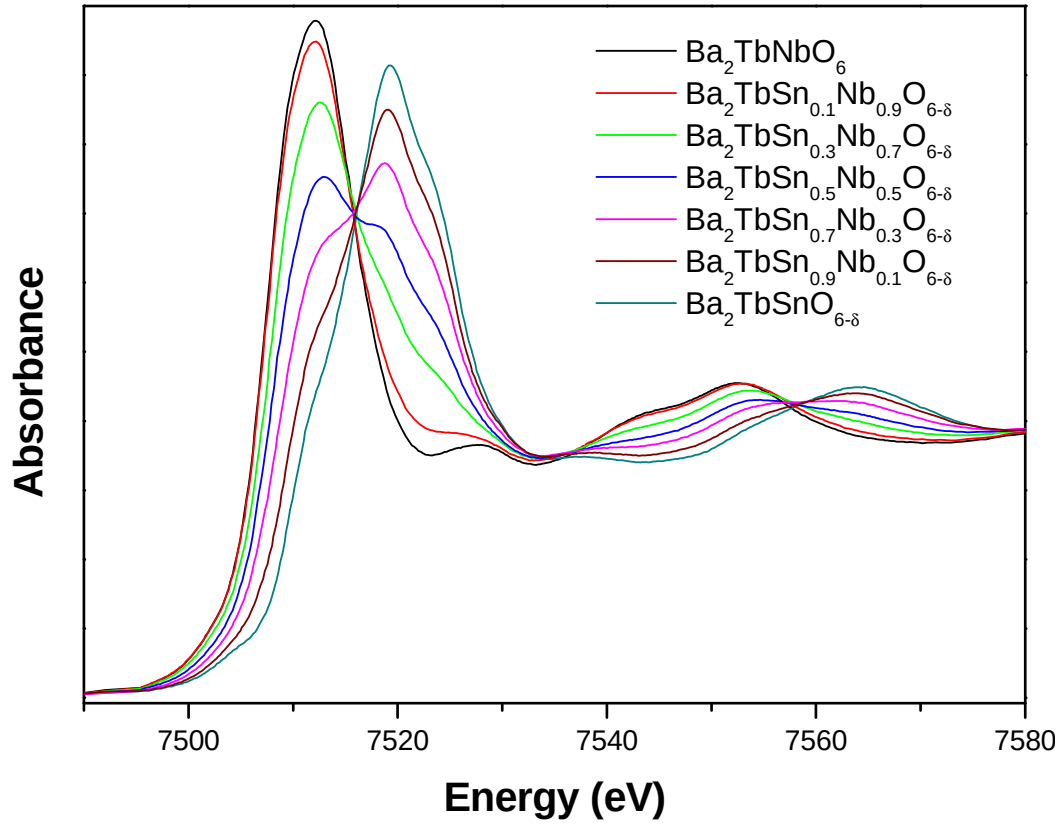

Figure 5.39: Tb L_{III}-edge spectra for selected compounds in the series $Ba_2TbSn_xNb_{1-x}O_{6-\delta}$ indicating the change in shape and energy of the edge with increasing x.

A combination of PCA and target transformation analysis, carried out over the range 7.425-7.800 keV, showed that the intermediate compounds in the series $Ba_2TbSn_xNb_{1-x}O_{6-\delta}$ consist of only two common components, which are excellent fits for the spectra of the two end member compounds, Ba_2TbNbO_6 and $Ba_2TbSnO_{6-\delta}$. A least squared fit of each of these intermediates, using these two component spectra, was carried out over the region 7.475-7.675 keV. This analysis indicates that the rate at which the Tb oxidation state changes as Sn^{4+} doping increases suggests the presence of a very small amount of oxygen vacancies, $\delta \approx 0.02$, in each of the intermediate compounds (see Figure 5.40 and Table 5.18 for oxidation state fraction and oxygen stoichiometry respectively). This is similar to the observation of oxygen vacancies in compounds in the series $Ba_2TbSn_xSb_{1-x}O_{6-\delta}$ although the lightly doped Sn^{4+} compounds in the antimonate series were found to have more oxygen vacancies. The analysis of the two Pr series on the other hand did not reveal any significant level of oxygen vacancies through a significant part of the series. In the $Ba_2PrSn_xNb_{1-x}O_{6-\delta}$

series, however, this may be a result of the larger error in the least squares analysis obscuring the presence of such vacancies.

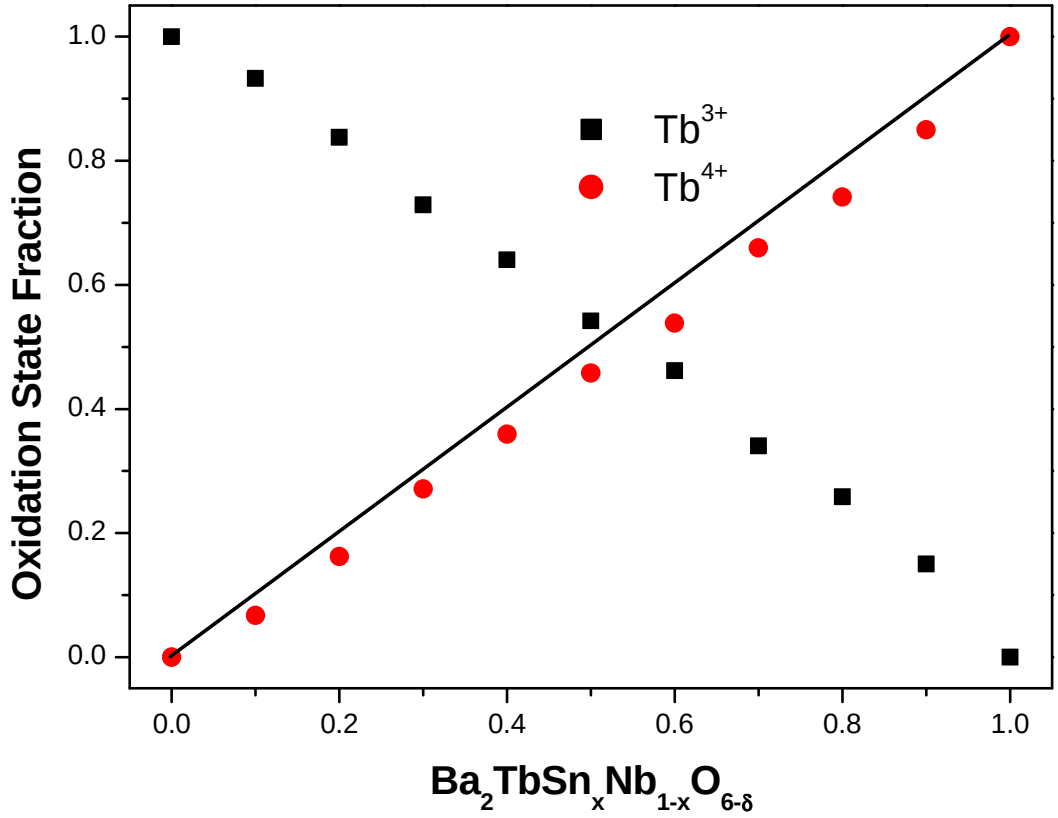

Figure 5.40: Plot of the oxidation state fraction of Tb^{3+} and Tb^{4+} in each compound examined in the $Ba_2TbSn_xNb_{1-x}O_{6-\delta}$ series. The black line depicts the amount of Tb^{4+} required at each composition for there to be no oxygen vacancies present and is drawn as a guide to the eye.

5.5 Conclusions

The structures adopted by compounds in the series $Ba_2LnSn_xB'_{1-x}O_{6-\delta}$ (Ln = Pr or Tb and B' = Nb^{5+} or Sb^{5+}) have been determined using synchrotron X-ray and neutron diffraction. UV-Vis-NIR and XANES spectroscopies were then used to determine the oxidation states of the cations present. In all four series it was shown than the trivalent lanthanide cation undergoes an oxidation state change to the tetravalent oxidation state with increased Sn^{4+} doping. In the series $Ba_2PrSn_xSb_{1-x}O_{6-\delta}$ it was found that there was a large two phase region from x = 0.3-0.9 which is likely to be associated with the segregation of Pr^{3+} and Pr^{4+} into two different phases. By contrast in the

other three series there is no indication of cation segregation with the two Tb series remaining single phase for all compositions while the two phase region in $Ba_2PrSn_xNb_{1-x}O_{6-\delta}$ was found to be caused by a discontinuous phase transition between *I*2/*m* monoclinic and $R\bar{3}$ rhombohedral structures. Oxidation of the lanthanide cation with increased Sn^{4+} doping leads to a loss of B-site cation ordering in all four series. The fashion in which the Tb and Pr series manifest this loss of order is, however, different. The Tb series lose order in a gradual fashion while in the Pr series it occurs suddenly or is associated with phase segregation.

The XANES analysis suggests that the oxidation state change of the lanthanide cation occurs with increasing Sn^{4+} doping so that there are apparently no oxygen vacancies in the Pr compounds and only a small quantity in the Tb containing compounds. Clearly oxidation of the Pr and Tb cations is strongly favoured over the formation of oxygen vacancies in these four series. This suggests that while these compounds might be good electrical conductors they are unlikely to be good oxygen anion or proton conductors as required for fuel cell applications. Therefore in Chapter 6 another series $Ba_2NdSn_xSb_{1-x}O_{6-\delta}$ is examined in which the Nd^{3+} cations cannot oxidise to the tetravalent state forcing oxygen vacancies to form with increased Sn^{4+} doping. Attention will be focused on the structures of these compounds particularly in regards to the presence of oxygen vacancy ordering in their structures.

5.6 References

[1] J.B. Goodenough, Rep. Prog. Phys. 67 (2004) 1915-1993.

[2] V.V. Kharton, F.M.B. Marques, A. Atkinson, Solid State Ionics 174 (2004) 135-149.

[3] K.D. Kreuer, Solid State Ionics 97 (1997) 1-15.

[4] S.J. Skinner, Int. J. Inorg. Mater. 3 (2001) 113-121.

[5] P. Murugaraj, K.D. Kreuer, T. He, T. Schober, J. Maier, Solid State Ionics 98 (1997) 1-6.

[6] R.D. Shannon, Acta Cryst. A 32 (1976) 751-767.

[7] J. Kurian, A.M. John, P.K. Sajith, J. Koshy, S.P. Pai, R. Pinto, Mater. Lett. 34 (1998) 208-212.

[8] J. Kurian, J. Koshy, P.R.S. Wariar, Y.P. Yadava, A.D. Damodaran, J. Solid State Chem. 116 (1995) 193-198.

[9] B.J. Kennedy, B.A. Hunter, C.J. Howard, J. Solid State Chem. 130 (1997) 58-65.

[10] M. Yoshimura, T. Nakamura, T. Sata, Bull. Tokyo Inst. Technol. 120 (1974) 13-27.

[11] Y. Hinatsu, J. Alloys Compd. 193 (1993) 113-115.

[12] A.M. Glazer, Acta Cryst. B 28 (1972) 3384-3392.

[13] C.J. Howard, B.J. Kennedy, P.M. Woodward, Acta Cryst. B 59 (2003) 463-471.

[14] V. Ting, Y. Liu, R.L. Withers, L. Norén, M. James, J.D. Fitz Gerald, J. Solid State Chem. 179 (2006) 551-562.

[15] V.F. Sears, Neutron News 3 (1992) 26-37.

[16] W.T. Fu, D. Visser, K.S. Knight, D.J.W. IJdo, J. Solid State Chem. 177 (2004) 1667-1671.

[17] A.J. Jacobson, B.C. Tofield, B.E.F. Fender, Acta Cryst. B 28 (1972) 956-961.

[18] N. Rosov, J.W. Lynn, Q. Lin, G. Cao, J.W. O'Reilly, P. Pernambuco-Wise, J.E. Crow, Phys. Rev. B 45 (1992) 982-986.

[19] R.H. Mitchell, *Perovskites Modern and Ancient*, Almaz Press, Ontario, 2002.

[20] K.S. Knight, Solid State Ionics 145 (2001) 275-294.

[21] K. Li, D. Xue, J. Phys. Chem. A 110 (2006) 11332-11337.

[22] I.D. Brown, A. Dabkowski, A. McCleary, Acta Cryst. B 53 (1997) 750-761.

[23] D.A. Pawlak, T. Lukasiewicz, M.A. Carpenter, M. Malinowski, R. Diduszko, J. Kisielewski, J. Cryst. Growth 282 (2005) 260-269.
[24] D. Pawlak, Z. Frukacz, Z. Mierczyk, A. Suchocki, J. Zachara, J. Alloys Compd. 275-277 (1998) 361-364.
[25] W.A. Pisarski, J. Pisarska, G. Dominiak-Dzik, W. Ryba-Romanowski, J. Phys.: Condens. Matter 16 (2004) 6171-6184.
[26] L. Ning, C.S.K. Mak, P.A. Tanner, Phys. Rev. B 72 (2005) 085127.
[27] V.F. Zolin, J. Alloys Compd. 380 (2004) 101-106.
[28] H.J. Emeléus, A.G. Sharpe, *Modern Aspects of Inorganic Chemistry*, Routledge & Kegan Paul, London, 1973.
[29] J. Rockenberger, U. zum Felde, M. Tischer, L. Tröger, M. Haase, H. Weller, J. Chem. Phys. 112 (2000) 4296-4304.
[30] J.M.M. Millet, M. Baca, A. Pigamo, D. Vitry, W. Ueda, J.L. Dubois, Appl. Catal. A-Gen. 244 (2003) 359-370.
[31] Z. Liu, K. Handa, K. Kaibuchi, Y. Tanaka, J. Kawai, J. Electron Spectrosc. Relat. Phenom. 135 (2004) 155-158.
[32] A.A. Bolzan, C. Fong, B.J. Kennedy, C.J. Howard, Acta Cryst. B 53 (1997)
[33] H. Arashi, S. Shin, H. Miura, A. Nakashima, M. Ishigame, O. Shimomura, Solid State Ionics 35 (1989) 323-327.
[34] T.W. Capehart, R.K. Mishra, J.F. Herbst, J. Appl. Phys. 72 (1992) 676-679.
[35] G.N. George, I.J. Pickering, *Principle Component Analysis and Target Transformation Using EXAFSPAK: Notes for Version 0.1*; Stanford Synchrotron Radiation Laboratory: 2002.
[36] G.N. George, I.J. Pickering, *EXAFSPAK: A Suite of Computer Programs for Analysis of X-Ray Absorption Spectra*; Stanford Synchrotron Radiation Laboratory: 2000.
[37] I.J. Pickering, *Edge Fitting Analysis Using EXAFSPAK: A Tutorial*; Standford Synchrotron Radiation Laboratory: 2001.
[38] B.J. Kennedy, C.J. Howard, K.S. Knight, Z. Zhang, Q. Zhou, Acta Cryst. B 62 (2006) 537-546.
[39] M.C. Gallardo, F.J. Romero, S.A. Hayward, E.K.H. Salje, J.d. Cerro, Mineral. Mag. 64 (2000) 971-982.
[40] E.K.H. Salje, Phase Transitions 34 (1991) 25-52.

[41] G.G. Cohen, D.A. Fischer, J. Colbert, N.J. Shevchik, Rev. Sci. Instrum. 51 (1980) 273-277.
[42] F. Bridges, X. Wang, J.B. Boyce, Nucl. Instrum. Methods Phys. Res., Sect. A 307 (1991) 316-324.